| Owner |

on behalf of Gazi University
Rector
Prof. Dr.
Musa YILDIZ

| Publishing Manager |

Prof. Dr.
Cevriye GENCER
Gazi University

| Chief Editor |

Prof. Dr.
Sema Bilge OCAK
Gazi University

| Managing Editor |

Prof. Dr.
Mustafa Gürhan YALÇIN
Akdeniz University

| Editorial Board |

| Editorial Board |

| Editorial Board |

| **Correspondence Address** |

Gazi University Graduate School of Natural and Applied Sciences
Emniyet Neighborhood, Bandırma Avenue, No:6/20B, 06560, Yenimahalle - ANKARA
B Block, Auxiliary Building

| **e-mail** |

gujsa06@gmail.com

| **web page** |

https://dergipark.org.tr/tr/pub/gujsa

Gazi University Journal of Science Part A: Engineering and Innovation
is a peer-reviewed journal.

| INDEXING |

| ACCESSIBILITY |

| CONTENTS |

| CONTENTS |

Hilbert I-Statistical Convergence on Neutrosophic Normed Spaces

Nazmiye GONUL BILGIN[1*] (iD)

[1]*Zonguldak Bulent Ecevit University, Department of Mathematics, Zonguldak, Türkiye*

Keywords	Abstract
Neutrosophic Normed Spaces Hilbert Matrix Statistical Convergence Hilbert Sequence Space Open Sets	In this paper, $\lambda\mathfrak{I}$-statistical convergence is defined to generalize statistical convergence on Neutrosophic normed spaces. As it is known, Neutrosophic theory, which brings a new breath to daily life and complex scientific studies which we encounter with many uncertainties, is a rapidly developing field with many new study subjects. Thus, researchers show great interest in this philosophical approach and try to transfer related topics to this field quickly. For this purpose, in this study, besides the definition of $\lambda\mathfrak{I}$-statistical convergence, the important features of Hilbert sequence space and $\lambda\mathfrak{I}$-statistical convergence in Neutrosophic spaces are examined with the help of these defined sequences. By giving the relationship between Hilbert $\lambda\mathfrak{I}$-statistical convergence and Hilbert $\mathfrak{I}$-statistical convergence, it has been evaluated whether the definitions contain a coverage relationship as in fuzzy and intuitionistic fuzzy. As a result, it is thought that the selected convergence type is suitable for the Neutrosophic normed space structure and is a guide for new convergence types.

1. INTRODUCTION

Statistical convergence and this concept-based studies play a very important role in areas such as solving some daily life problems, computer science and information theory. Statistical convergence was defined in Fast, 1951. Subsequently, many important modifications of this concept were studied. For example, λ-statistical convergence was introduced in (Mursaleen, 2000) and ideal convergence was given in Kostyrko et al., 2000. Later on, Savas and Das (2011) defined I-λ-statistical convergence. Recently, the types of ideal convergence have been moved to different spaces and important contributions have been made to the theory. Examples of these spaces can be given as fuzzy and intuitionistic fuzzy normed spaces.

Fuzzy theory, allows us to transform imprecise information. This concept was given in (Zadeh, 1965). Fuzzy set theory has been applied to different engineering fields where uncertainty is modeled. e.g. quantum physics (Madore, 1992) computer programming (Giles,1980), control of chaos (Fradkov & Evans, 2005). Moreover, the concept of fuzzy and its modification have been given in different spaces For example, Bilgin & Bozma, 2020; Ali & Ansari, 2022; Guner & Aygun, 2022.

Later, the opinion of the intuitionistic fuzzy set was defined in (Atanassov,1986). This concept and its various generalizations were given in different spaces for example Melliani et al., 2015; Gonul Bilgin & Bozma, 2021. In order to transfer uncertain situations to fuzzy normed spaces, Felbin (1992) defined fuzzy normed space then Saadati and Park (2006) gave basic structures of intuitionistic fuzzy norm. Kumar and Kumar (2008) have been studied ideal convergent in fuzzy number theory. Then, Savas and Gurdal (2015) defined λ-ideal convergence in a intuitionistic fuzzy normed space.

*Corresponding Author, e-mail: nazmiyegonul@beun.edu.tr

Neutrosophic set theory; was established by Smarandache (1999) who added the degree of uncertainty of the subject by recognizing the inadequacy and deficiency of the fuzzy logic dealing with the degree of membership and the intuitionistic fuzzy logic dealing with membership-nonmembership. In the scientific world, it is not always possible to definitively interpret a problem in daily life as right or wrong. Therefore, this concept has gained so much popularity. For example uncertainty theory plays an important role in constructing a model in different technological problem. On the other hand, many researchers have been working on this new theory in mathematics (e.g. Kisi, 2021a,b,c; Bilgin, 2022; Gonul Bilgin, 2022).

The transfer of special sequences to normed spaces is one of the popular topics of recent times. Kirisci (2019), examined a generalization of the statistical convergence he has been created with the help of the Fibonacci sequence on the intuitionistic fuzzy normed space. Polat (2016) has defined new type Hilbert sequence spaces and Khan et al. (2020) have been gave some properties of Hilbert I-convergent sequences. After that, Khan et al. (2020) transferred this concept to intuitionistic fuzzy normed spaces.

In the literature review, it was seen that Hilbert sequence space, which is one of the important sequence spaces, was not examined together with this new space and statistical convergence. This study was carried out in order to eliminate this deficiency and to bring a different perspective to the theory. In the study, after the basic definitions and theorems are given, these three concepts and important theoretical information about them have been presented.

(Smarandache, 2016) Let's $y_1, y_2, \ldots, y_n \in [0,1]$ be n crisp-components. Their sum is next form

1. $0 \leq y_1 + y_2 + \cdots + y_n \leq n,$
    if all of them are 100% independent two by two,

2. $0 \leq y_1 + y_2 + \cdots + y_n \leq 1,$
    if all of them are 100% dependent.

(Neutrosophic Set) (Smarandache, 1999) Let $\mathcal{S} \neq \emptyset$, $\Theta_{\mathfrak{N},M}(z), \Upsilon_{\mathfrak{N},I}(z)$ and $\Psi_{\mathfrak{N},n.M}(z)$ are the degrees of membership, indeterminacy, non-membership of z. A neutrosophic set $\mathfrak{N}$ has the following notation:

$$\mathfrak{N} = \left\{ \left(z, \Theta_{\mathfrak{N},T}(z), \Psi_{\mathfrak{N},n.M}(z), \Upsilon_{\mathfrak{N},I}(z) \right) : z \in \mathcal{S} \right\}$$

where for each z in $\mathcal{S}$, $\Theta_{\mathfrak{N},M}(z), \Upsilon_{\mathfrak{N},I}(z), \Psi_{\mathfrak{N},n.M}(z) \in [0,1]$, $0 \leq \Theta_{\mathfrak{N},M}(z) + \Psi_{\mathfrak{N},n.M}(z) + \Upsilon_{\mathfrak{N},I}(z) \leq 2$.

Here, $\Theta_{\mathfrak{N},M}(z), \Upsilon_{\mathfrak{N},I}(z)$ are dependent components, $\Psi_{\mathfrak{N},n.M}(z)$ is an independent component.

(Neutrosophic Normed Spaces) (Kirisci & Simsek, 2020) Let $\boxtimes$ and $\boxplus$ show the continuous $\mathfrak{t} - norm$ and continuous $\mathfrak{t} - conorm$, $\mathcal{S}$ be a linear spaces on $\mathbb{R}$. A Neutrosophic Normed is a notation of the form $\left\{ \left((z, \mathfrak{s}), \Theta_{\mathfrak{N},M}(z, \mathfrak{s}), \Psi_{\mathfrak{N},n.M}(z, \mathfrak{s}), \Upsilon_{\mathfrak{N},I}(z, \mathfrak{s}) \right) : (z, \mathfrak{s}) \in \mathcal{S} \times \mathbb{R}^+ \right\}$ where $\Theta_{\mathfrak{N},M}, \Upsilon_{\mathfrak{N},I}$ and $\Psi_{\mathfrak{N},n.M}$ are shown the degree of membership, indeterminacy, non-membership of $(z, \mathfrak{s})$ on $\mathcal{S} \times \mathbb{R}^+$ satisfies next:

For every $z, w \in \mathcal{S}$,

1. For all $\mathfrak{s} \in \mathbb{R}^+$ $\Theta_{\mathfrak{N},M}(z, \mathfrak{s}), \Upsilon_{\mathfrak{N},I}(z, \mathfrak{s}), \Psi_{\mathfrak{N},n.M}(z, \mathfrak{s}) \in [0,1]$ then

    $\Theta_{\mathfrak{N},M}(z, \mathfrak{s}) + \Upsilon_{\mathfrak{N},I}(z, \mathfrak{s}) + \Psi_{\mathfrak{N},n.M}(z, \mathfrak{s}) \leq 2,$

2. For all $\mathfrak{s} \in \mathbb{R}^+$,

$\Theta_{\mathfrak{N},M}(z, \mathfrak{s}) = 1 \Longleftrightarrow z = 0, \Upsilon_{\mathfrak{N},I}(z, \mathfrak{s}) = 0 \Longleftrightarrow z = 0, \Psi_{\mathfrak{N},n.M}(z, \mathfrak{s}) = 0 \Longleftrightarrow z = 0,$

3. For each $\mathfrak{d} \neq 0$,

$\Theta_{\mathfrak{N},M}(\mathfrak{d}z, \mathfrak{s}) = \Theta_{\mathfrak{N},M}\left(z, \frac{\mathfrak{s}}{|\mathfrak{d}|} \right), \Upsilon_{\mathfrak{N},I}(\mathfrak{d}z, \mathfrak{s}) = \Upsilon_{\mathfrak{N},I}\left(z, \frac{\mathfrak{s}}{|\mathfrak{d}|} \right), \Psi_{\mathfrak{N},n.M}(\mathfrak{d}z, \mathfrak{s}) = \Psi_{\mathfrak{N},n.M}\left(z, \frac{\mathfrak{s}}{|\mathfrak{d}|} \right)$

4. For all $\mathfrak{s}_1, \mathfrak{s}_2 \in \mathbb{R}^+$,

$$\Theta_{\mathfrak{R},M}(z,\mathfrak{s}_2) \odot \Theta_{\mathfrak{R},M}(\mathfrak{p},\mathfrak{s}_1) \leq \Theta_{\mathfrak{R},M}(z+\mathfrak{p}, \mathfrak{s}_1 + \mathfrak{s}_2),$$

$$\Upsilon_{\mathfrak{R},I}(z,\mathfrak{s}_2) \otimes \Upsilon_{\mathfrak{R},I}(z,\mathfrak{s}_1) \geq \Upsilon_{\mathfrak{R},I}(z+\mathfrak{p}, \mathfrak{s}_1 + \mathfrak{s}_2),$$

$$\Psi_{\mathfrak{R},n.M}(z,\mathfrak{s}_2) \otimes \Psi_{\mathfrak{R},n.M}(z,\mathfrak{s}_1) \geq \Psi_{\mathfrak{R},n.M}(z+\mathfrak{p}, \mathfrak{s}_1 + \mathfrak{s}_2).$$

5. $\Theta_{\mathfrak{R},M}(z,\cdot)$ is non-decreasing- continuous function; $\Upsilon_{\mathfrak{R},I}(z,\cdot)$, $\Psi_{\mathfrak{R},n.M}(z,\cdot)$ are non-increasing, continuous function,
6. $\lim\limits_{\mathfrak{s}\to\infty} \Theta_{\mathfrak{R},M}(z,\mathfrak{s}) = 1$, $\lim\limits_{\mathfrak{s}\to\infty} \Upsilon_{\mathfrak{R},I}(z,\mathfrak{s}) = 0$, $\lim\limits_{\mathfrak{s}\to\infty} \Psi_{\mathfrak{R},n.M}(z,\mathfrak{s}) = 0$.
7. Let $\mathfrak{s} \leq 0$. thus situated $\Theta_{\mathfrak{R},M}(z,\mathfrak{s}) = 0$, $\Upsilon_{\mathfrak{R},I}(z,\mathfrak{s}) = 1$, $\Psi_{\mathfrak{R},n.M}(z,\mathfrak{s}) = 1$.

So, $(\mathcal{S}, \Theta_{\mathfrak{R},M}, \Upsilon_{\mathfrak{R},I}, \Psi_{\mathfrak{R},n.M}, \odot, \otimes)$ is named Neutrosophic Normed Spaces. In this case, $\Theta_{\mathfrak{R},M}$, $\Psi_{\mathfrak{R},n.M}$ are dependent, $\Upsilon_{\mathfrak{R},I}$ is an independent.

(Ideal) (Kostyrko et al., 2000) Let $\mathcal{S} \neq \emptyset$ and a family of $\mathfrak{I} \subset \mathcal{P}(\mathcal{S})$ is an ideal where,

1. $\emptyset \in \mathfrak{I}$,
2. for every $S_1, S_2 \in \mathfrak{I}$, then $S_1 \cup S_2 \in \mathfrak{I}$,
3. for all $S_1 \in \mathfrak{I}$ and $S_2 \subset S_1$, then $S_2 \in \mathfrak{I}$.

($\mathcal{H}$ − transforms) (Polat, 2016) Let $\mathcal{K}, \mathcal{K}^*$ be a sequence spaces and $x = (x_k) \in \mathcal{K}$, $\mathcal{H} = (\hbar_{rk}) \in \mathcal{K}^*$ be a triangle Hilbert matrix where for $1 \leq k \leq r$, $\hbar_{rk} = \frac{1}{r+k-1}$ and for $k > r$, $\hbar_{rk} = 0$. $\mathcal{H}$ − transform of (x_k) is defined as

$$\mathcal{H}_r(x) = \sum_{k=1}^{r} \frac{1}{r+k-1} x_k.$$

In the following section, some basic properties of $\lambda\mathfrak{I}$-convergent and Cauchy sequences are given. Throughout this study, the sequence (x_k) is taken as the bounded sequence.

2. MATERIALS AND METHODS

2.1 $\lambda\mathfrak{I}$-Convergence on Neutrosophic Normed Spaces

Definition 2.1 Let $(\mathcal{S}, \Theta_{\mathfrak{R},M}, \Psi_{\mathfrak{R},n.M}, \Upsilon_{\mathfrak{R},I}, \odot, \otimes)$ be a Neutrosophic normed spaces and $\lambda = (\lambda_r)$ be a non-decreasing sequence of positive numbers, $\lim\limits_{r\to\infty} \lambda_r = \infty$ also $\lambda_1 = 1$, $\lambda_{r+1} \leq \lambda_r + 1$. (x_k) is called $\lambda\mathfrak{I}$-convergence to $\mathfrak{L}_{\mathfrak{R}}$ with respect to $(\Theta_{\mathfrak{R},M}, \Psi_{\mathfrak{R},n.M}, \Upsilon_{\mathfrak{R},I})$ in $\mathcal{S}$, if for all $0 < \varepsilon < 1$ and $\mathfrak{s} > 0$, the set

$$\{r \in \mathbb{N}: \Theta_{\mathfrak{R},M}(\mathcal{M}_r(x_k) - \mathfrak{L}_{\mathfrak{R}}, \mathfrak{s}) \leq 1 - \varepsilon \text{ or } \Upsilon_{\mathfrak{R},I}(\mathcal{M}_r(x_k) - \mathfrak{L}_{\mathfrak{R}}, \mathfrak{s}) \geq \varepsilon \text{ and } \Psi_{\mathfrak{R},n.M}(\mathcal{M}_r(x_k) - \mathfrak{L}_{\mathfrak{R}}, \mathfrak{s}) \geq \varepsilon\} \in \mathfrak{I}$$

where $\mathcal{I}_r = [r - \lambda_r + 1, r]$ and $\mathcal{M}_r(x_k) = \frac{1}{\lambda_r} \sum_{k\in\mathcal{I}_r} x_k$.

This sequences is shown with $(x_k) \to \mathfrak{L}_{\mathfrak{R}_{\lambda\mathfrak{I}}}$ or $(\lambda\mathfrak{I})_{\mathfrak{R}} - \lim x_k = \mathfrak{L}_{\mathfrak{R}}$.

Lemma 2.1 Let $(\mathcal{S}, \Theta_{\mathfrak{R},M}, \Upsilon_{\mathfrak{R},I}, \Psi_{\mathfrak{R},n.M}, \odot, \otimes)$ be a Neutrosophic normed spaces and (x_k) be a $\lambda\mathfrak{I}$-convergent sequences. Then, for all $0 < \varepsilon < 1$, $\mathfrak{s} > 0$, the next situations are equivalent,

1. $(\lambda\mathfrak{I})_{\mathfrak{R}} - \lim x_k = \mathfrak{L}_{\mathfrak{R}}$,

2. $\{r \in \mathbb{N}: \Theta_{\mathfrak{R},M}(\mathcal{M}_r(x_k) - \mathfrak{L}_{\mathfrak{R}}, \mathfrak{s}) \leq 1 - \varepsilon\} \in \mathfrak{I}$, $\{r \in \mathbb{N}: \Psi_{\mathfrak{R},n.M}(\mathcal{M}_r(x_k) - \mathfrak{L}_{\mathfrak{R}}, \mathfrak{s}) \geq \varepsilon\} \in \mathfrak{I}$,

$$\{r \in \mathbb{N} : \Upsilon_{\mathfrak{N},I}(\mathcal{M}_r(x_k) - \mathfrak{L}_{\mathfrak{N}}, \mathfrak{s}) \geq \varepsilon\} \in \mathfrak{I}.$$

3. $(\lambda\mathfrak{I})_{\mathfrak{N}} - \lim \Theta_{\mathfrak{N},M}(x_k - \mathfrak{L}_{\mathfrak{N}}, \mathfrak{s}) = 1,$

   $(\lambda\mathfrak{I})_{\mathfrak{N}} - \lim \Psi_{\mathfrak{N},n.M}(x_k - \mathfrak{L}_{\mathfrak{N}}, \mathfrak{s}) = 0,$

   $(\lambda\mathfrak{I})_{\mathfrak{N}} - \lim \Upsilon_{\mathfrak{N},I}(x_k - \mathfrak{L}_{\mathfrak{N}}, \mathfrak{s}) = 0.$

Proof Using Definition 2.1, the equivalence of properties are easily obtained.

Lemma 2.2 Let $(\mathcal{S}, \Theta_{\mathfrak{N},M}, \Upsilon_{\mathfrak{N},I}, \Psi_{\mathfrak{N},n.M}, \odot, \otimes)$ be a Neutrosophic normed spaces, (x_k) be a $\lambda\mathfrak{I}$-convergent to $\mathfrak{L}_{\mathfrak{N}}$. Then, $\mathfrak{L}_{\mathfrak{N}}$ is unique.

Proof It can be easily proved by assuming that there are two $\mathfrak{L}_{\mathfrak{N}}$ and making a contradiction.

Now, let's recall the definition of the filter (Mursaleen, 2000). Let $\mathcal{S} \neq \emptyset$ and a family of $\mathcal{F} \subset \mathcal{P}(\mathcal{S})$ is a filter where, $\emptyset \notin \mathcal{F}$; for all $S_1, S_2 \in \mathcal{F}$ then $S_1 \cap S_2 \in \mathcal{F}$; for all $S_1 \in \mathcal{F}$ and $S_1 \subset S_2$ then $S_2 \in \mathcal{F}$.

Let $\mathfrak{I} \neq \emptyset$, $\mathcal{S} \notin \mathfrak{I}$. Then, $\mathcal{F} = \mathcal{F}(\mathfrak{I}) = \{(\mathcal{S} \setminus I) : I \in \mathfrak{I}\}$ is a Filter.

Definition 2. 2 Let $(\mathcal{S}, \Theta_{\mathfrak{N},M}, \Psi_{\mathfrak{N},n.M}, \Upsilon_{\mathfrak{N},I}, \odot, \otimes)$ be a Neutrosophic normed spaces and $\mathcal{I}_r = [r - \lambda_r + 1, r]$. (x_k) is named $\lambda\mathfrak{I}$-Cauchy sequences in $\mathcal{S}$, where for each $\varepsilon \in (0,1)$, $\mathfrak{s} > 0$, there exist $\tilde{n} \in \mathbb{N}$:

$$\{r \in \mathbb{N} : \Theta_{\mathfrak{N},M}(\mathcal{M}_r(x_k) - \mathcal{M}_r(x_{\tilde{n}}), \mathfrak{s}) > 1 - \varepsilon \text{ or } \Upsilon_{\mathfrak{N},I}(\mathcal{M}_r(x_k) - \mathcal{M}_r(x_{\tilde{n}}), \mathfrak{s}) < \varepsilon \text{ and } \Psi_{\mathfrak{N},n.M}(\mathcal{M}_r(x_k) - $$

$$- \mathcal{M}_r(x_{\tilde{n}}), \mathfrak{s}) < \varepsilon\} \in \mathcal{F}(\mathfrak{I}),$$

where $\mathcal{M}_r(x_k) = \dfrac{1}{\lambda_r} \displaystyle\sum_{k \in \mathcal{I}_r} x_k.$

2.2 $\mathcal{H}$- Sequences Spaces Using Neutrosophic Norm

Definition 2.3 Let $(\mathcal{S}, \Theta_{\mathfrak{N},M}, \Psi_{\mathfrak{N},n.M}, \Upsilon_{\mathfrak{N},I}, \odot, \otimes)$ be a Neutrosophic normed spaces and $\lambda = (\lambda_r)$ be a sequence whose properties are given above. The sequences space of the $\mathcal{H} -$ transforms of (x_k) $\lambda\mathfrak{I}$-converging to $\mathfrak{L}_{\mathfrak{N}}$ with respect to Neutrosophic norm $(\Theta_{\mathfrak{N},M}, \Psi_{\mathfrak{N},n.M}, \Upsilon_{\mathfrak{N},I})$ in $\mathcal{S}$ is defined as follows.

$$\mathfrak{C}_{\mathfrak{N}} = \{x = (x_k) : \{r \in \mathbb{N} : \Theta_{\mathfrak{N},M}(\mathcal{M}_r(\mathcal{H}_k x) - \mathfrak{L}_{\mathfrak{N}}, \mathfrak{s}) \leq 1 - \varepsilon \text{ or } \Upsilon_{\mathfrak{N},I}(\mathcal{M}_r(\mathcal{H}_k x) - \mathfrak{L}_{\mathfrak{N}}, \mathfrak{s}) \geq \varepsilon \text{ and }$$

$$\Psi_{\mathfrak{N},n.M}(\mathcal{M}_r(\mathcal{H}_k x) - \mathfrak{L}_{\mathfrak{N}}, \mathfrak{s}) \geq \varepsilon\} \in \mathfrak{I}\}$$

where $\mathcal{I}_r = [r - \lambda_r + 1, r]$, $0 < \varepsilon < 1$,

$$\mathcal{M}_r(x_k) = \frac{1}{\lambda_r} \sum_{k \in \mathcal{I}_r} x_k.$$

Lemma 2.3 Let $(\mathbb{R}, \Theta_{\mathfrak{N},M}, \Psi_{\mathfrak{N},n.M}, \Upsilon_{\mathfrak{N},I}, \odot, \otimes)$ be a Neutrosophic normed spaces. The sequences spaces $\mathfrak{C}_{\mathfrak{N}}$ is a linear spaces on $\mathbb{R}$.

Now, using techniques similar to those in intuitinistic fuzzy normed spaces an open ball with center x, radius a will be given as:

Definition 2.4 Let $(\mathcal{S}, \Theta_{\mathfrak{N},M}, \Upsilon_{\mathfrak{N},I}, \Psi_{\mathfrak{N},n.M}, \odot, \otimes)$ be a Neutrosophic normed spaces. An open ball is given next form using $\mathcal{H} -$ transforms:

$\mathcal{B}_{\mathcal{H}}\big((x,a),\mathfrak{s}\big) = \big\{(\mathfrak{z}_k): \{r \in \mathbb{N}: \Theta_{\mathfrak{R},M}(\mathcal{M}_r(\mathcal{H}_k x) - \mathcal{M}_r(\mathcal{H}_k \mathfrak{z}),\mathfrak{s}) > 1-a \ and \ \Upsilon_{\mathfrak{R},I}(\mathcal{M}_r(\mathcal{H}_k x) - \mathcal{M}_r(\mathcal{H}_k \mathfrak{z}),\mathfrak{s}) < a$

$and \ \Psi_{\mathfrak{R},n.M}(\mathcal{M}_r(\mathcal{H}_k x) - \mathcal{M}_r(\mathcal{H}_k \mathfrak{z}),\mathfrak{s}) < a\}\big\}$

Lemma 2.4 Let $\mathfrak{C}_{\mathfrak{R}}$ is a sequences spaces given in Definition 2.3. In this case, every open ball is an open set in $\mathfrak{C}_{\mathfrak{R}}$.

Proof   Let $(\mathcal{H}_k \mathfrak{z}) \in \mathcal{B}_{\mathcal{H}}\big((x,a),\mathfrak{s}\big)$ and   then $\Theta_{\mathfrak{R},M}(\mathcal{M}_r(\mathcal{H}_k x) - \mathcal{M}_r(\mathcal{H}_k \mathfrak{z}),\mathfrak{s}) > 1-a$, $\Upsilon_{\mathfrak{R},I}(\mathcal{M}_r(\mathcal{H}_k x) - \mathcal{M}_r(\mathcal{H}_k \mathfrak{z}),\mathfrak{s}) < a$ and $\Psi_{\mathfrak{R},n.M}(\mathcal{M}_r(\mathcal{H}_k x) - \mathcal{M}_r(\mathcal{H}_k \mathfrak{z}),\mathfrak{s}) < a$. So there exists a $\mathfrak{s}^* \in (0,\mathfrak{s})$: $\Theta_{\mathfrak{R},M}(\mathcal{M}_r(\mathcal{H}_k x) - \mathcal{M}_r(\mathcal{H}_k \mathfrak{z}),\mathfrak{s}^*) > 1-a$, $\Upsilon_{\mathfrak{R},I}(\mathcal{M}_r(\mathcal{H}_k x) - \mathcal{M}_r(\mathcal{H}_k \mathfrak{z}),\mathfrak{s}^*) < a$ and $\Psi_{\mathfrak{R},n.M}(\mathcal{M}_r(\mathcal{H}_k x) - \mathcal{M}_r(\mathcal{H}_k \mathfrak{z}),\mathfrak{s}^*) < a$.

On the other hand, let $u := \Theta_{\mathfrak{R},M}(\mathcal{M}_r(\mathcal{H}_k x) - \mathcal{M}_r(\mathcal{H}_k \mathfrak{z}),\mathfrak{s}^*)$. So, $u > 1-a$ then, there exists $0 < h < 1$: $u > 1-h > 1-a$. Using the properties of $\mathfrak{t}-norm$ and $\mathfrak{t}-conorm$, given $u > 1-h$, $u^*, u^{**} \in (0,1)$ is getting. Here, $u \odot u^* > 1-h$ and $(1-u) \otimes (1-u^{**}) < h$. Then $u^{***} := max\{u^*, u^{**}\}$. To show that $\mathcal{B}_{\mathcal{H}}\big((\mathcal{H}_k \mathfrak{z}, 1-u^{***}),\mathfrak{s}-h\big) \subset \mathcal{B}_{\mathcal{H}}\big((x,a),\mathfrak{s}\big)$, let $v \in \mathcal{B}_{\mathcal{H}}\big((\mathcal{H}_k \mathfrak{z}, 1-u^{***}),\mathfrak{s}-h\big)$.

So, $\Theta_{\mathfrak{R},M}(\mathcal{M}_r(\mathcal{H}_k x) - \mathcal{M}_r(\mathcal{H}_k v),\mathfrak{s}^*) \geq \Theta_{\mathfrak{R},M}(\mathcal{M}_r(\mathcal{H}_k x) - \mathcal{M}_r(\mathcal{H}_k \mathfrak{z}),h) \odot \Theta_{\mathfrak{R},M}(\mathcal{M}_r(\mathcal{H}_k \mathfrak{z}) - \mathcal{M}_r(\mathcal{H}_k v)$

$,u-h) > u \odot u^{***} \geq u \odot u^* > 1-h > 1-a$.

Moreover,

$\Upsilon_{\mathfrak{R},I}(\mathcal{M}_r(\mathcal{H}_k x) - \mathcal{M}_r(\mathcal{H}_k v),\mathfrak{s}) \leq \Upsilon_{\mathfrak{R},I}(\mathcal{M}_r(\mathcal{H}_k x) - \mathcal{M}_r(\mathcal{H}_k \mathfrak{z}),h) \otimes \Upsilon_{\mathfrak{R},I}(\mathcal{M}_r(\mathcal{H}_k \mathfrak{z}) - \mathcal{M}_r(\mathcal{H}_k v),\mathfrak{s}-h)$

$\leq (1-u) \otimes (1-u^{***}) \leq (1-u) \otimes (1-u^{**}) < a$.

$\Psi_{\mathfrak{R},n.M}(\mathcal{M}_r(\mathcal{H}_k x) - \mathcal{M}_r(\mathcal{H}_k v),\mathfrak{s}^*)$ can be obtained in a similar way.

Thus, $(\mathcal{H}_k v) \in \mathcal{B}_{\mathcal{H}}\big((x,a),\mathfrak{s}\big)$, $\mathcal{B}_{\mathcal{H}}\big((\mathcal{H}_k \mathfrak{z}, 1-u^{***}),\mathfrak{s}-h\big) \subset \mathcal{B}_{\mathcal{H}}\big((x,a),\mathfrak{s}\big)$. So, every open ball is an open set in $\mathfrak{C}_{\mathfrak{R}}$.

Definition 2.5 Let $\big(\mathcal{S}, \Theta_{\mathfrak{R},M}, \Upsilon_{\mathfrak{R},I}, \Psi_{\mathfrak{R},n.M}, \odot, \otimes\big)$ be a Neutrosophic normed spaces, (x_k) is called Hilbert $\lambda\mathfrak{J}$-statistical convergence to $\mathfrak{L}_{\mathfrak{R}}$ if, for all $\varepsilon > 0$, $s > 0$, there exist a $\mathfrak{L}_{\mathfrak{R}}$:

$\Big\{r \in \mathbb{N}: \dfrac{1}{\lambda_r} \mid k \in \mathcal{J}_r: \Theta_{\mathfrak{R},M}(\mathcal{M}_r(\mathcal{H}_k x) - \mathfrak{L}_{\mathfrak{R}},\mathfrak{s}) \leq 1-\varepsilon \ or \ \Upsilon_{\mathfrak{R},I}(\mathcal{M}_r(\mathcal{H}_k x) - \mathfrak{L}_{\mathfrak{R}},\mathfrak{s}) \geq \varepsilon \ and$

$\Psi_{\mathfrak{R},n.M}(\mathcal{M}_r(\mathcal{H}_k x) - \mathfrak{L}_{\mathfrak{R}},\mathfrak{s}) \geq \varepsilon \big| \Big\} \in \mathfrak{J}$.

This situation is denoted with $(x_k) \to \mathfrak{L}_{\mathfrak{R}}\big(st_{\lambda\mathfrak{J}}^{\mathcal{H}}\big)$.

The set of Hilbert $\lambda\mathfrak{J}$-statistical convergence according to neutrosophic normed, is denoted by $St_{\lambda\mathfrak{J}}^{\mathcal{H}}$. For $\lambda_r = r$, it is called Hilbert $\mathfrak{J}$-statistical convergent to $\mathfrak{L}_{\mathfrak{R}}$.

Theorem 2.1 Let (x_k) be Hilbert $\mathfrak{J}$-statistical convergent to $\mathfrak{L}_{\mathfrak{R}}$ on $\big(\mathcal{S}, \Theta_{\mathfrak{R},M}, \Upsilon_{\mathfrak{R},I}, \Psi_{\mathfrak{R},n.M}, \odot, \otimes\big)$. If $\liminf\limits_{r\to\infty} \dfrac{\lambda_r}{r} > 0$, then (x_k) is Hilbert $\lambda\mathfrak{J}$-statistical convergent to $\mathfrak{L}_{\mathfrak{R}}$.

Proof For given $0 < \varepsilon < 1$,

$\frac{1}{r} | k \le n : \Theta_{\mathfrak{N},M}(\mathcal{M}_r(\mathcal{H}_k x) - \mathfrak{L}_{\mathfrak{N}}, \mathfrak{s}) \le 1 - \varepsilon \ or \ \Upsilon_{\mathfrak{N},I}(\mathcal{M}_r(\mathcal{H}_k x) - \mathfrak{L}_{\mathfrak{N}}, \mathfrak{s}) \ge \varepsilon \ and \ \Psi_{\mathfrak{N},n.M}(\mathcal{M}_r(\mathcal{H}_k x) - \mathfrak{L}_{\mathfrak{N}}$

$, \mathfrak{s}) \ge \varepsilon | \ge \frac{1}{r} | k \in \mathcal{I}_r : \Theta_{\mathfrak{N},M}(\mathcal{M}_r(\mathcal{H}_k x) - \mathfrak{L}_{\mathfrak{N}}, \mathfrak{s}) \le 1 - \varepsilon \ or \ \Upsilon_{\mathfrak{N},I}((\mathcal{M}_r \mathcal{H}_k x) - \mathfrak{L}_{\mathfrak{N}}, \mathfrak{s}) \ge \varepsilon, \Psi_{\mathfrak{N},n.M}(\mathcal{M}_r(\mathcal{H}_k x$

$) - \mathfrak{L}_{\mathfrak{N}}, \mathfrak{s}) \ge \varepsilon | \ge \frac{\lambda_r}{r} \frac{1}{\lambda_r} | k \in \mathcal{I}_r : \Theta_{\mathfrak{N},M}(\mathcal{M}_r(\mathcal{H}_k x) - \mathfrak{L}_{\mathfrak{N}}, \mathfrak{s}) \le 1 - \varepsilon \ or \ \Upsilon_{\mathfrak{N},I}(\mathcal{M}_r(\mathcal{H}_k x) - \mathfrak{L}_{\mathfrak{N}}, \mathfrak{s}) \ge \varepsilon ,$

$\Psi_{\mathfrak{N},n.M}(\mathcal{M}_r(\mathcal{H}_k x) - \mathfrak{L}_{\mathfrak{N}}, \mathfrak{s}) \ge \varepsilon |.$

If $\liminf\limits_{r \to \infty} \frac{\lambda_r}{r} = c$, then from definition $\left\{ r \in \mathbb{N} : \frac{\lambda_r}{r} < \frac{c}{2} \right\}$ is finite. For $\delta > 0$,

$\left\{ n \in \mathbb{N} : \frac{1}{\lambda_r} | k \in \mathcal{I}_r : \Theta_{\mathfrak{N},M}(\mathcal{M}_r(\mathcal{H}_k x) - \mathfrak{L}_{\mathfrak{N}}, \mathfrak{s}) \le 1 - \varepsilon \ or \ \Upsilon_{\mathfrak{N},I}(\mathcal{M}_r(\mathcal{H}_k x) - \mathfrak{L}_{\mathfrak{N}}, \mathfrak{s}) \ge \varepsilon, \Psi_{\mathfrak{N},n.M}(\mathcal{M}_r(\mathcal{H}_k x) \right.$

$\left. - \mathfrak{L}_{\mathfrak{N}}, \mathfrak{s}) \ge \varepsilon | \ge \delta \right\} \subset \left\{ n \in \mathbb{N} : \frac{1}{r} | k \in \mathcal{I}_r : \Theta_{\mathfrak{N},M}(\mathcal{M}_r(\mathcal{H}_k x) - \mathfrak{L}_{\mathfrak{N}}, \mathfrak{s}) \le 1 - \varepsilon \ or \ \Upsilon_{\mathfrak{N},I}(\mathcal{M}_r(\mathcal{H}_k x) - \mathfrak{L}_{\mathfrak{N}}, \mathfrak{s}) \ge \varepsilon, \right.$

$\left. \Psi_{\mathfrak{N},n.M}(\mathcal{M}_r(\mathcal{H}_k x) - \mathfrak{L}_{\mathfrak{N}}, \mathfrak{s}) \ge \varepsilon | \ge \frac{c}{2} \delta \right\} \cup \left\{ n \in \mathbb{N} : \frac{\lambda_r}{r} < \frac{c}{2} \right\}.$

Here, since the set on the right belongs to $\mathfrak{I}$ then the desired result is getting.

3. RESULTS AND DISCUSSION

In this study, the definition of $\lambda\mathfrak{I}$ −convergence for Neutrosophic normed spaces and important properties for, $\lambda\mathfrak{I}$ −convergent sequences are given. In addition, the definition of $\lambda\mathfrak{I}$ −Cauchy sequence is established. The $\mathcal{H}$ −transforms of, $\lambda\mathfrak{I}$ −sequences and the open ball definition have been studied. The definition of Hilbert statistical convergence is given and an important property of these sequences is proved.

Khan et al. (2020) defined Hilbert I-convergent sequence spaces in the classical sense and Khan et al. (2022) introduced the concept of Hilbert ideal convergent series for intuitionistic fuzzy normed spaces. On the other hand, Savas and Gurdal (2015) defined the concept of λ −convergent sequence for intuitionistic fuzzy normed spaces using ideals. Then, for Neutrosophic normed spaces, Khan et al. (2019) gave the definition of statistical convergence using Fibonacci matrices. In addition, the definition of Fibonacci I-convergent in intuitionistic fuzzy normed spaces has been given by Kisi & Guler (2019).

In this study, an important convergence definition has been made on Neutrosophic normed spaces, where convergence types in fuzzy and intuitionistic fuzzy normed spaces have been transferred quickly in the last few years. Moreover, due to its connection with statistical convergence and its use in the $\mathcal{H}$ −transform, many important concepts in the mentioned space were brought together for the first time in this study.

4. CONCLUSION

In this paper, firstly, the definition of $\lambda\mathfrak{I}$ −convergence is created for Neutrosophic Normed Spaces, which forms the basis of the research. Important properties are given for $\lambda\mathfrak{I}$ −convergent sequences also the unique of such convergent sequences is proven. Then, the definition of the Cauchy sequence for the $\lambda\mathfrak{I}$ −sequence structure has been given. An $\mathcal{H}$ −transform of the sequences set up in this space is created and an open ball definition has been given with the help of this transformation. By showing that the open ball-open set relationship is preserved in this defined space, the Hilbert statistical convergence definition is given, and in this sense, an important property for convergent sequences has been proven.

In this study, a concept is defined that will allow the evaluation of important studies in Neutrosophic normed spaces from different perspectives. In future studies, it is aimed to obtain different properties of the defined concept and to create the equivalent of the concept in different sequence spaces.

ACKNOWLEDGEMENT

CONFLICT OF INTEREST

The author declares no conflict of interest.

REFERENCES

Ali, G., & Ansari, M. N. (2022). Multiattribute decision-making under Fermatean fuzzy bipolar soft framework. *Granular Computing*, *7*(2), 337-352. doi:10.1007/s41066-021-00270-6

Atanassov, K. T. (1986). Intuitionistic fuzzy sets. *Fuzzy Sets and* Systems, *20*(1), 87-96. doi:10.1016/S0165-0114(86)80034-3

Bilgin, N. G. (2022). Rough Statistical Convergence In Neutrosophic Normed Spaces. *Euroasia Journal of Mathematics, Engineering, Natural & Medical Sciences*, *9*(21), 47-55. doi:10.38065/euroasiaorg.958

Bilgin, N. G., & Bozma, G. (2020). On Fuzzy n-Normed Spaces Lacunary Statistical Convergence of Order±. *i-Manager's Journal on Mathematics,* 9(2), 1-7. doi:10.26634/jmat.9.2.17841

Fast, H. (1951). Sur la convergence statistique. *Colloquium Mathematicae*, *2*(3-4)*,* 241-244.

Felbin, C. (1992). Finite-dimensional fuzzy normed linear space. *Fuzzy Sets and Systems*, *48*(2), 239-248. doi:10.1016/0165-0114(92)90338-5

Fradkov, A. L., & Evans, R. J. (2005). Control of chaos: methods and applications in engineering. *Annual Reviews in Control*, *29*(1), 33-56. doi:10.1016/j.arcontrol.2005.01.001

Giles, R. (1980). A computer program for fuzzy reasoning. *Fuzzy Sets and Systems*, *4*(3), 221-234. doi:10.1016/0165-0114(80)90012-3

Gonul Bilgin, N. (2022). Hibrid Δ-Statistical Convergence for Neutrosophic Normed Space. *Journal of Mathematics*, *2022*, 3890308. doi:10.1155/2022/3890308

Gonul Bilgin, N., & Bozma, G. (2021). Fibonacci Lacunary Statistical Convergence of Order γ in IFNLS. *International Journal of Advances in Applied Mathematics and Mechanics*, *8*(4), 28-36.

Guner, E., & Aygun, H. (2022). A New Approach to Fuzzy Partial Metric Spaces. *Hacettepe Journal of Mathematics and Statistics*, *51*(6), 1-14. doi:10.15672/hujms.1115381

Khan, V. A., Khan, M. D., & Mobeen, A. (2019). Some results of neutrosophic normed spaces via fibonacci matrix, *U.P.B Sci. Bull., Series A*, 20(2), 1-14.

Khan, V. A., Alshlool, K. M. A. S., & Alam, M. (2020). On Hilbert I-convergent sequence spaces. *Journal of Mathematics and Computer Science*, *20*(3), 225-233. doi:10.22436/jmcs.020.03.05

Khan, V. A., Ali., Abdullah, S. A. A., & Alshlool, K. M. A. S. (2022). On intuitionistic fuzzy hilbert ideal convergent sequence spaces. *Acta Scientiarum. Technology*, *44*(1), e59724. doi:10.4025/actascitechnol.v44i1.59724

Kirisci, M. (2019). Fibonacci statistical convergence on intuitionistic fuzzy normed spaces. *Journal of Intelligent & Fuzzy Systems*, *36*(6), 5597-5604. doi:10.3233/jifs-181455

Kirisci M., & Simsek, N. (2020). Neutrosophic normed spaces and statistical convergence, *Journal of Analysis*, *28*(4), 1059-1073. doi:10.1007/s41478-020-00234-0

Kisi, O. (2021a). Convergence Methods for Double Sequences and Applications in Neutrosophic Normed Spaces. In: *Soft Computing Techniques in Engineering, Health, Mathematical and Social Sciences* (pp. 137-154). CRC Press.

Kisi, O. (2021b). On Iθ-convergence in Neutrosophic Normed Spaces. *Fundamental Journal of Mathematics and Applications*, *4*(2), 67-76. doi:10.33401/fujma.873029

Kisi, O. (2021c). Ideal convergence of sequences in neutrosophic normed spaces. *Journal of Intelligent & Fuzzy Systems*, *41*(2), 2581-2590. doi:10.3233/JIFS-201568

Kisi O., & Guler E. (2019). On Fibonacci ideal convergence of double sequences in intuitionistic fuzzy normed linear spaces. *Turkish Journal of Mathematics and Computer Science*, *11*(Special Issue: Proceedings of ICMME 2019), 46-55.

Kostyrko, P., Salat, T., & Wilczynski, W. (2000). I-Convergence. *Real Anal. Exchange*, *26*(2), 669-686.

Kumar, V., & Kumar, K. (2008). On the ideal convergence of sequences of fuzzy numbers. *Information Sciences*, *178*(24), 4670-4678. doi:10.1016/j.ins.2008.08.013

Madore, J. (1992). Fuzzy physics *Annals of Physics*, *219*(1), 187-198. doi:10.1016/0003-4916(92)90316-E

Melliani, S., Elomari, M., Chadli, L. S., & Ettoussi, R. (2015). Intuitionistic fuzzy metric space. *Notes on Intuitionistic Fuzzy Sets*, *21*(1), 43-53.

Mursaleen, M. (2000). Lambda-statistical convergence. *Mathematica* Slovaca, *50*(1), 111–115.

Polat, H. (2016). Some new Hilbert sequence spaces. *Muş Alparslan University Journal of Science*, *4*(1), 367-372.

Saadati, R., & Park, J. H. (2006). Intuitionistic fuzzy euclidean normed spaces. *Communications in* MathematicalAnalysis, *1*(2), 85-90.

Savas, E., & Das, P. (2011). A generalized statistical convergence via ideals. *Applied Mathematics Letters*, *24*(6), 826-830. doi:10.1016/j.aml.2010.12.022

Savas, E., & Gurdal, M. (2015). A generalized statistical convergence in intuitionistic fuzzy normed spaces. *Science Asia*, *41*(4), 289-294. doi:10.2306/scienceasia1513-1874.2015.41.289

Smarandache, F., (1999). *A Unifying Field in Logics: Neutrosophic Logic. Neutrosophy, Neutrosophic Set, Neutrosophic Probability*. American Research Press, Rehoboth, NM.

Smarandache, F. (2016). Degree of dependence and independence of the (sub)components of fuzzy set and neutrosophic set. *Neutrosophic Sets and Systems*, *11*, 95-97. doi:10.5281/zenodo.50941

Zadeh, L. A. (1965). Fuzzy sets. *Information and Control*, *8*(3), 338-353. doi:10.1016/S0019-9958(65)90241-X

The Comparison of the Temperature Susceptibility of the Serial Resistance Effect of Au/n-GaAs Type M/S Structures

Esra EVCİN BAYDİLLİ[1*] iD

[1]Hakkari University, Faculty of Engineering, Department of Electrical and Electronics Engineering, Hakkari, Türkiye

Keywords	Abstract
M/S Structures Serial Resistance Ohm's Law Cheung-Cheung Functions Norde Function	To enable comparison with the literature, this study seeks to assess the temperature susceptibility of serial resistance (R_s) features of the Au/n-GaAs type M/S structure, which is acceptable the benchmark sample. The serial resistance features of the sample were computed separately withal principal of Ohm, Norde, and Cheungs' functions. The current-voltage (I-V) data used in order to compute were evaluated at the voltage values between +2V and -2 V and temperature values between 120K and 360K in 60K steps. Each computation method was also compared one another other. As a result, the fact that the R_s values computed using principal of Ohm, Norde functions and Cheungs' functions tended to reduce with rising temperature, as anticipated by the literature results. In addition, it was determined that, with only tiny variations, the temperature susceptibility of R_s is consistent across all computation methods. In addition, as a result of the comparison with the literature, it was concluded serial resistance is less of an issue when a polymer interfacial layer is present at the metal-semiconductor contact region. The R_s parameter of the M/S structure is, in essence, a sensitive function of temperature and input voltage.

1. INTRODUCTION

Metal/semiconductor (M/S) structures are extensive on the developing the microelectronics industry (Özdemir et al., 2021). Previously, silicon was widely used as a semiconductor in M/S structures, obtained by tight metal contact with a semiconductor. After that, GaAs became competitive with silicon due to its high electron mobility and increasing demand for devices operating at microwave frequency (Novoselov et al., 2004; Sadao, 2005). Its wide band gap of 1.42 eV makes GaAs a more resistant material against radiation. These features make it suitable for communication, aviation and space systems. In addition, GaAs, a direct band gap semiconductor, is ideal for optoelectronic devices (Çiçek et al., 2016). Au/n-GaAs is a fundamental and well-known type of M/S structures (Helal et al., 2020). Then, since the junction region properties of M/S structures significantly affect the contact performance, an interface layer has started to be placed between the M/S to control the charge transitions, prevent diffusion and leakage currents, and passivate the interface states (Sato and Yasumura, 1985; Altındal Yerişkin, 2019). In this study, the Au/n-GaAs type sample was accepted as a reference sample to compare the serial resistance properties of the M/S structures with an interfacial layer such as MIS and MPS types structures.

In M/S structures, the image-force, the tunneling, the edge, and the serial resistance effects are the factors that cause deviation from the ideal condition (Evcin Baydilli et al., 2020). The serial resistance (R_s) effect, among the most crucial of them, is the semiconductor's neutral region's resistance to the flow of current across the M/S contact, which is located outside the deplation region. (Deniz et al., 2022). As the positive voltage values increase, the R_s effect starts effective and the contact current declines as a result. (Ashajyothi & Reddy, 2021).

The cause of this reduction in current is that when the voltage applied to the contact increases, the saturation effect occurs with the serial resistance effect and reduces the contact current (Rhoderick, 1978). So, this causes serious computation errors originating from R_s (Evcin Baydilli et al., 2020). Features such as conductor wire taken from M/S structures for measurements, the affinity of ohmic contact with semiconductor crystal, a dirty film layer formed on the interface, the semiconductor in the M/S structures has a disordered contribution distribution, the resistance of the M/S contact's depletion region on the semiconductor side, and the ohmic contact resistance causes a serial resistance effect (Sevgili et al., 2022).

This study focuses on the serial resistance effect of the Au/n-GaAs sample depending on temperature and voltage using principal of Ohm, Norde, and Cheungs' functions. Additionally, the outcomes of every method were contrasted with one another. The first method is principle of Ohm, the most well-known resistance computation method. The Norde method, developed by Norde, allows the calculation of R_s and potential barrier height (Φ_{Bo}) values using the F(V) function defined by a single I-V curve in which the temperature does not change when n=1 in its initial state (Norde, 1979). The Norde function was developed by Bohlin and allowed the computation of the R_s and Φ_{Bo} parameters of M/S structures if there is n>>1 (Bohlin, 1986). Another function that enables the analysis of R_s and other parameters (such as n, Φ_{Bo}) is the Cheungs' function. Cheungs' first function calculates the ideality factor (n) and R_s, and the second function, again, R_s and barrier height Φ_{Bo} were calculated. This method is considered a more straightforward method derived from I-V datas. In this approach, when the forward bias I-V curve precisely turns, R_s becomes active. (Cheung & Cheung, 1986).

In this research, the Au/n-GaAs type M/S structure's I-V data were evaluated at the voltage values between +2V and -2 V and temperature values between 120K and 360K in 60K steps. Because temperature is one of the most critical factors affecting the M/S structures parameters (Çaldıran, 2020), it is necessary to analyze the temperature susceptibility. Moreover, the n, R_s, and Φ_{Bo} parameters were also computed one by one by principal of Ohm, Norde, and Cheungs'functions. Computing these parameters with different methods will allow us to obtain valid and reliable results for the sample, making it possible to compare the results with the literature.

2. MATERIALS AND METHODS/EXPERIMENTAL METHODS

The n-GaAs semiconductor in the Au/n-GaAs type M/S structure was acquired by the Molecular Beam Epitaxy (MBE) method. The thickness of the n-GaAs semiconductor substrate is about 1 μm, its radius is 3", and it has [1 0 0] surface orientation. First, chemical cleaning of n-GaAs was performed to clean the substrate's impurity. Therefore, the substrate was ultrasonically washed with acetone ((CH_3COH_3) and isopropyl alcohol (C_3H_8O), respectively. After the substrate was ultrasonically washed with 18 MΩ-cm de-ionized water, it was dried with nitrogen (N_2) gas for 3 minutes. After the chemical cleaning process, ohmic contacts were prepared using 99.999% pure gold (Au) metal on the matte face of the n-GaAs wafer utilizing the thermal evaporation system. The constructed ohmic contact measures around 150 nm thick. For the ohmic contact to have low resistance, the annealing process was executed in the nitrogen medium at 500 °C for 3 minutes. Then, Au rectifying contacts were prepared on the substrate's bright (front) surface withal the thermal evaporation method, by utilizing a mask that have 1mm diameter holes. The obtained rectifier contacts are approximately 150 nm thick and 1 mm in diameter. The prepared Au/n-GaAs type M/S structure is shown in Figure 1. Current-voltage (I-V) data of the sample were perused between 120K and 360K temperature values in 60K steps by Kheitley 2400 current voltage source and the measurements was performed in the vpf-475 cryostat. Temperature monitoring was done with the temperature control device, Lake Shore model 321. Figure 2 presents the measurement system.

3. RESULTS AND DISCUSSION

The Au/n-GaAs type M/S structure's I-V datas outcomes are displayed in Figure 3 for a temperature range of 120K to 360K with 60K steps. Around 1 V, the I-V curves' linearity starts to degrade, at which point the Rs effect can be seen for each temperature setting. The inset graph shows the linear region between 0.6 V and 0.95 V in the current-voltage curve. By the extrapolating of the area where the I-V graph is linear, it is passed from experimental to theoretical calculation. Using the results of these calculations and the equations given below, the results in Table 1 were obtained (Rhoderick, 1978);

$$I = I_o \exp\left(\frac{qV}{nkT}\right) \tag{1}$$

$$\ln(I) = \ln(I_o) + \frac{q}{nkT} V_D \tag{2}$$

$$\Phi_{Bo} = \frac{kT}{q} \ln\left(\frac{AA^*T^2}{I_o}\right) \tag{3}$$
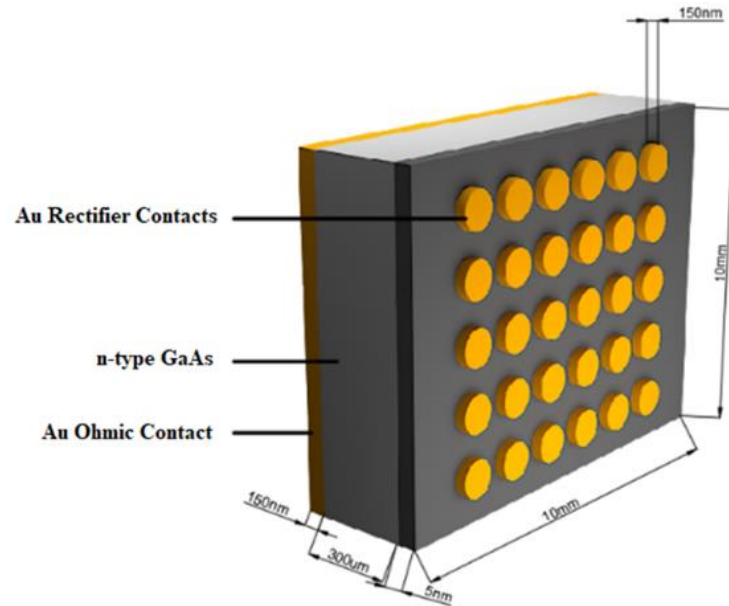
Figure 1. *The schematic presentation of the Au/n-GaAs type MS structure*
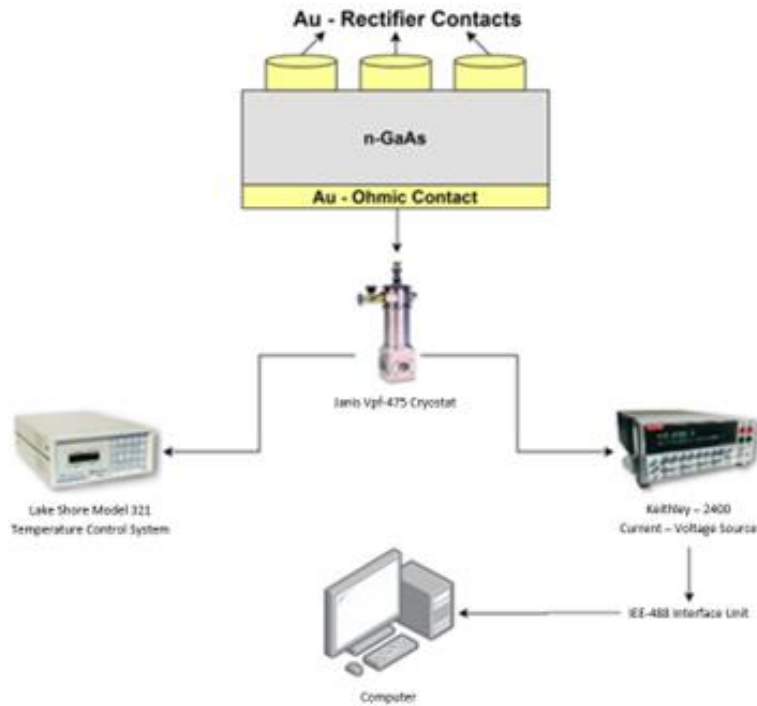
Figure 2. *The schematic presentation of the system for measuring.*
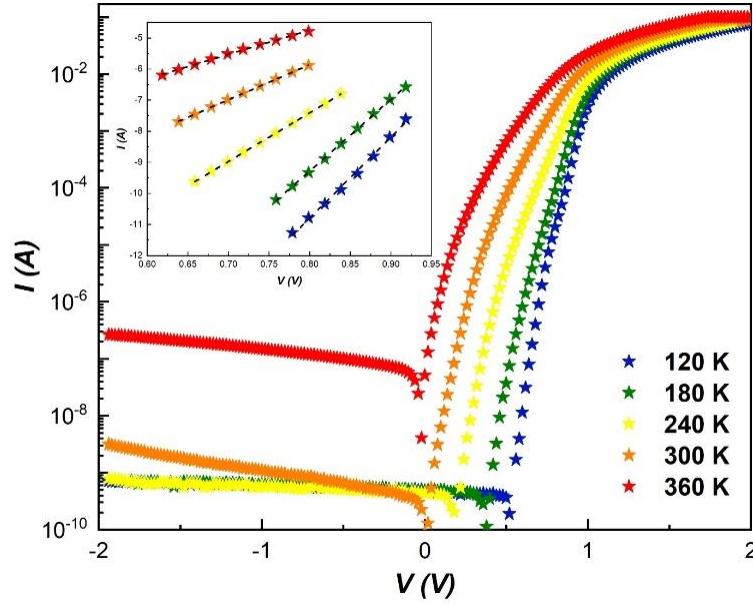
Figure 3. *The semilogarithmic I-V graph of Au/n-GaAs type M/S structure for each temperature value.*

Table 1. *n, Φ_{Bo}, and R_S parameters of Au/n-GaAs type M/S structure for each temperature value.*

T (K)	n	Φ_{Bo} (eV)	I_o (A)
120	2.25	0.398	8.13E-20
180	2.11	0.549	9.13E-15
240	1.44	0.582	5.95E-13
300	1.26	0.609	3.1E-10
360	1.04	0.622	6.94E-08

These findings suggest that the literature's description of barrier inhomogeneity as the cause of the decrease in n values and rise in Φ_{Bo} values with rising temperature (Werner & Güttler, 1991; Baydilli et al., 2020).

For each temperature setting, the graph of V vs. R_s is shown in Figure 4. Principle of Ohm was used to derive R_s values from forward bias values (Eq. 4) (Evcin Baydilli et al., 2020). As can be observed, temperature and applied voltage have a significant impact on the R_s values. Additionally, as Table 2's R_s values demonstrate, they drop as temperature rises. Because with increasing temperature, the carriers have more energy to overcome the barrier and higher voltage levels cause the I-V curve to bend, which indicates an increase in charge carrier density. (Taşyürek et al., 2022). So, the effect of R_s decreases. In the inset graph, it is seen that when the applied voltage increases, the values of R_s decrease. Recombination/generation CTMs (current-conduction mechanisms) can explain this phenomenon. (Werner and Güttler, 1991). In addition, after the temperature rises above room temperature, it is seen that the voltage-dependent R_s values converge as the temperature increases. This behavior can be explained by the Thermionic Emission theory becoming more effective after room temperature.

$$R_s = \frac{dV_i}{dI_i}$$ (4)
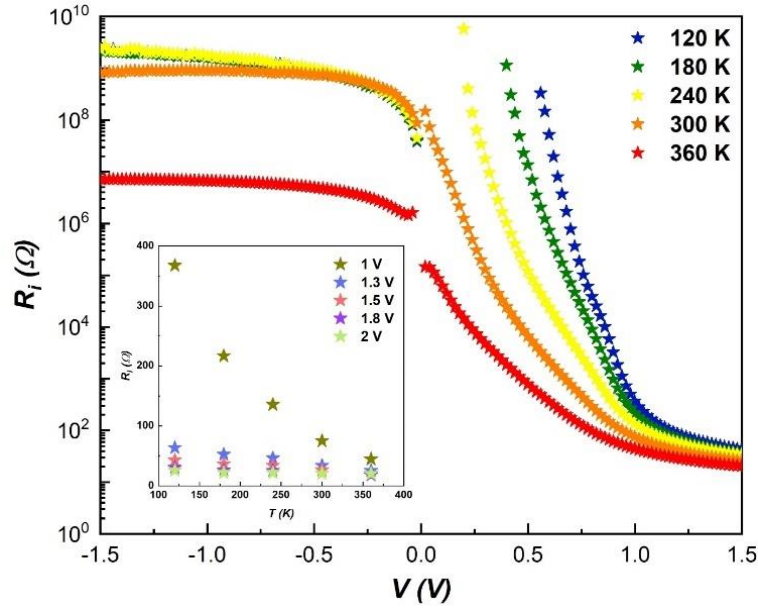
Figure 4. *R_i vs V_i and R_s vs T graph of Au/n-GaAs type M/S structure for each temperature value.*

Table 2. *R_S parameters of Au/n-GaAs type M/S structure for each temperature value.*

T (K)	R_s (Ω)
120	25.73
180	22.08
240	21.76
300	20.42
360	19.99

It has been stated that temperature and voltage have a considerable impact on the effect of R_s. The forward bias linear area changes as a result of this variability. That's why, it is helpful to refer to the Norde and Cheungs' functions to define the linear area of the positive voltage region. The graph of V vs. F(V), the outcome of the Norde function for each temperature value, is shown in Figure 5. The I-V features were utilized to derive the values of the ideality factors and current that are used in the F(V) function. The gamma (γ) value is a unitless integer created by adding to the n values by 2 (γ=n+2). Φ_{Bo} and R_s parameters were obtained by substituting V_{min} and I_{min} values to Eq. 5 and 6 (Uslu et al., 2010). The mentioned parameters and calculation results are shown in Table 3. It is seen that by increasing temperature values, R_s values decrease while Φ_{Bo} values increase.

$$F(V) = \frac{V}{\gamma} - \frac{kT}{q} \ln\left(\frac{I(V)}{AA^*T^2} \right) \tag{5}$$

$$R_s = \frac{(\gamma - n)kT}{qI_{min}} \tag{6}$$
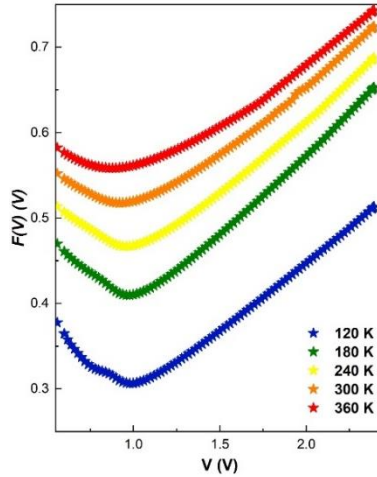
Figure 5. F(V)-V graph of Au/n-GaAs type M/S structure for all temperatures.

Table 3. *Some parameters obtained from the Norde function of Au/n-GaAs type M/S structure for each temperature value.*

T (K)	V_{min} (V)	$F(V)_{min}$ (V)	I_{min} (A)	Φ_{Bo} (eV)	R_s (Ω)	n	γ
120	0.98	0.306	0.0020	0.488	10.58	2.25	4.25
180	0.98	0.406	0.0036	0.622	8.54	2.11	4.11
240	0.94	0.488	0.0043	0.715	7.88	1.44	3.44
300	0.86	0.564	0.0050	0.794	6.36	1.26	3.26
360	0.72	0.621	0.0047	0.827	4.72	1.04	3.04

The graph in Figure 6a displays the linear results from Cheungs' first function, which are depicted in Eq.7 (Uslu et al., 2010). The n values were derived from the ordinate intersection point and the R_s values from the slope by fitting this linear region. Figure 6b shows the linear regions obtained from Cheung's second function, which is given in Eq. 8 (Uslu et al., 2010). The n value used in Cheung's second function is obtained from Cheungs' first function. From these linear regions' slopes, R_s values were computed, and from the ordinate intercept points, Φ_{Bo} values were computed. Table 4 shows the obtained results. The n values drop as the temperature values rise, while the Φ_{Bo} values rise. It is seen that the R_s values derived from the first and second Cheungs' functions are consistent with one another and reduce as the temperature value rises.
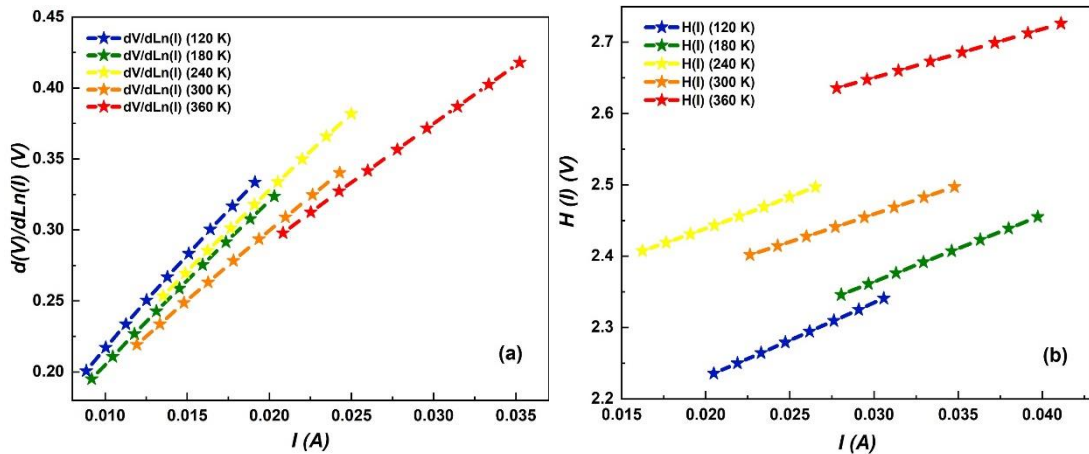
Figure 6. The graph of a) Cheungs' first function b) Cheung's second function for Au/n-GaAs type M/S structure for each temperature value

Table 4. *n, R_s, and Φ_{Bo} values obtained from Cheungs' functions of Au/n-GaAs type M/S structure for each temperature value*

	1st Function of Cheungs'		2nd Function of Cheungs'	
T (K)	**n**	**R_s (Ω)**	**R_s (Ω)**	**Φ_{Bo} (eV)**
120	8.45	12.932	10.428	0.239
180	5.79	11.581	9.342	0.360
240	4.97	11.213	8.714	0.456
300	3.98	9.801	7.838	0.558
360	4.03	8.321	6.809	0.607

Figure 7 shows temperature-dependent serial resistance computed by the principle of Ohm, Norde and Cheungs' first and second functions. With a few small variations brought on by the various I-V regions that each method considers, it can be argued that the behavior of the results acquired with each method are consistent with one another (Evcin Baydilli et al., 2020; Pehlivanoglu, 2021). The interface carriers are trapped, the concentration of free carriers diminishes, and the serial resistance effect grows as the n values rise with decreasing temperature (Evcin Baydilli et al., 2020).
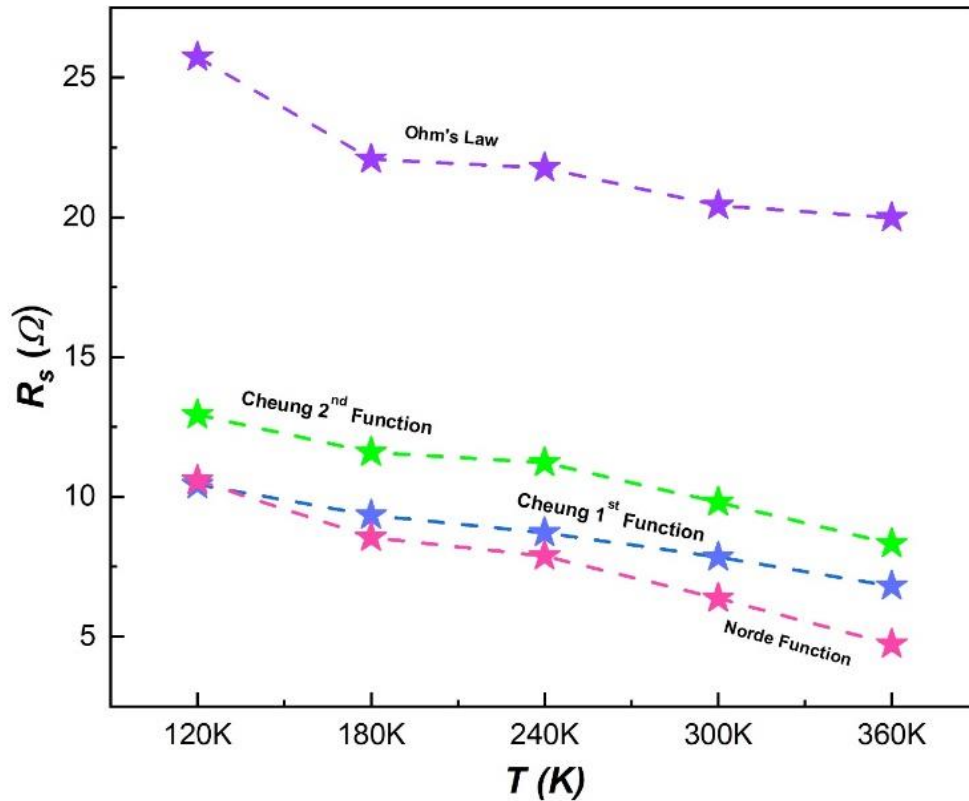
Figure 7. *Temperature-dependent R_s values of Au/n-GaAs type M/S structure according to Ohm's Law, Norde and Cheungs' Functions.*

Figure 8 belongs to our previous study (Evcin Baydilli et al., 2020). Unlike in Au/n-GaAs type M/S structure, there is a 7% Gr doped-PVA interfacial layer. In Figure 8, partial leaps are seen. This behavior can be explained by the fact that the different current-conduction mechanisms are active together or alone (Evcin Baydilli et al., 2020). On the other hand, it can be said that the effect of R_s decreases with increasing temperature for all

methods. In addition, it is seen that the serial resistance values of Au/(%7 Gr-doped)PVA/n-GaAs type M/P/S structure are lower than the serial resistance values of Au/n-GaAs type M/S structure. It could be asserted that the reason for these differences seen in Figure 7 and Figure 8 is the existence of the %7 Gr doped-PVA interfacial coating.
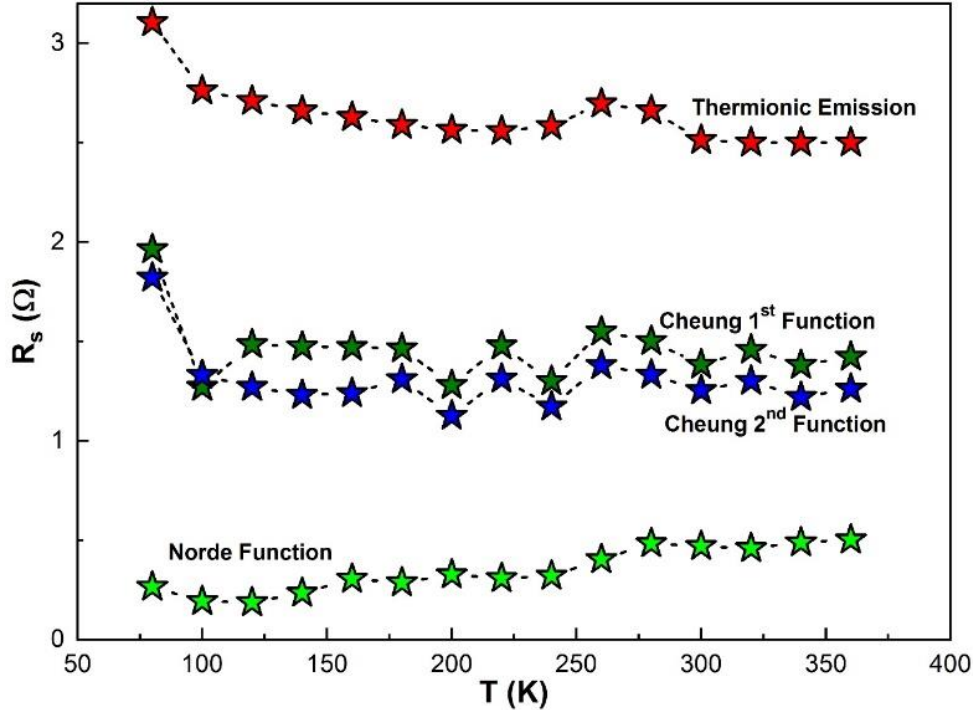
Figure 8. Temperature-dependent R_s values of Au/(%7 Gr-doped)PVA/n-GaAs type M/P/S structure according to Principle of Ohm, Norde and Cheungs' Functions (Evcin Baydilli et al., 2020).

Table 5 shows the comparison of the temperature-dependent changes of the n, R_s and Φ_{Bo} values obtained by principle of Ohm, Norde and Cheungs' functions of Au/n-GaAs type M/S and Au/(7% Gr-doped)PVA/n-GaAs type M/P/S structures. By the increase in temperature, the ideality factors of both structures decreased. When we compare the ideality factor values of the two structures, it is seen that the n values of the M/S structure are lower than those of the M/P/S structure. When the Φ_{Bo} values are examined, it is seen that the Φ_{Bo} values of both structures decrease with the increase in temperature. When the Φ_{Bo} values of the two structures are compared, it is seen that the Φ_{Bo} values of the M/P/S structure are lower than the Φ_{Bo} values of the M/S structure. It can be said that this difference between the two structures is due to the polymer interfacial layer. In addition, the temperature-dependent behavior of n and Φ_{Bo} values of both structures is explained by barrier inhomogeneity in the literature (Evcin Baydilli et al., 2020).

4. CONCLUSION

In this study, serial resistance properties of Au/n-GaAs type M/S structure depending on temperature and voltage, were investigated by three diverse methods: principle of Ohm, Norde, and Cheungs' functions. I-V measurements taken at ±2 V voltage and 120K-360K temperature range were used for computation process. The findings indicate that the Rs values, which are calculated by three methods, decreased with the increase in temperature. Additionally, with a few minor exceptions, the R_s values are likewise compatible with one another. That explains these slight variations caused by the various I-V regions that are considered by all methods. It has been found that the existence of the interface coating in M/S structures lessens the impact of serial resistance as compared to the literature. It is therefore determined that the serial resistance characteristics of Au/n-GaAs type M/S type structures are a decisive function of temperature and applied voltage.

Table 5. *Comparative representation of n, R_s, and Φ_{Bo} values obtained by Principle of Ohm, Norde and Chungs' functions of Au/n-GaAs type M/S and Au/(%7 Gr-doped)PVA/n-GaAs type MPS structures (Evcin Baydilli et al., 2020)*

Methode/Temperature	120 K	180 K	240 K	300 K	360 K
Ohm's Law **(for Au/n-GaAs)**					
R_s (Ω)	25.73	22.08	21.76	20.42	19.99
Φ_{Bo} (eV)	0.398	0.549	0.582	0.609	0.622
n	2.25	2.11	1.44	1.26	1.04
Ohm's Law **(for Au/(%7 Gr-doped)PVA/n-GaAs)**					
R_s (Ω)	2.71	2.59	2.58	2.51	2.5
Φ_{Bo} (eV)	0.19	0.3	0.43	0.55	0.64
n	12.44	7.79	5.18	3.83	3.21
Norde Function **(for Au/n-GaAs)**					
R_s (Ω)	10.58	8.54	7.88	6.36	4.72
Φ_{Bo} (eV)	0.488	0.622	0.715	0.794	0.827
Norde Function **(for Au/(%7 Gr-doped)PVA/n-GaAs)**					
R_s (Ω)	0.19	0.29	0.32	0.47	0.5
Φ_{Bo} (eV)	0.23	0.34	0.45	0.55	0.67
Cheung's 1st Function **(for Au/n-GaAs)**					
R_s (Ω)	12.932	11.581	11.213	9.801	8.321
n	8.45	5.79	4.97	3.98	4.03
Cheung's 1st Function **(for Au/(%7 Gr-doped)PVA/n-GaAs)**					
R_s (Ω)	1.48	1.47	1.49	1.38	1.42
n	10.68	6.84	5.29	4.65	3.19
Cheung's 2nd Function **(for Au/n-GaAs)**					
R_s (W)	10.428	9.342	8.714	7.838	6.809
Φ_{Bo} (eV)	0.239	0.36	0.456	0.558	0.607
Cheung's 2nd Function **(for Au/(%7 Gr-doped)PVA/n-GaAs)**					
R_s (W)	1.27	1.31	1.3	1.22	1.26
Φ_{Bo} (eV)	0.19	0.28	0.39	0.46	0.65

ACKNOWLEDGEMENT

REFERENCES

Altındal Yerişkin, S. (2019). The investigation of effects of (Fe$_2$O$_4$-PVP) organic-layer, surface states, and serial resistance on the electrical characteristics and the sources of them. *Journal of Materials Science: Materials in Electronics*, *30*, 17032-17039. doi:10.1007/s10854-019-02045-x

Ashajyothi, S., & Reddy, V. R. (2021). Influence of tin oxide (SnO$_2$) interlayer on the electrical and reverse current conduction mechanism of Au/n-InP Schottky junction and its microstructural properties. *Thin Solid Films*, *740*, 139001. doi:10.1016/j.tsf.2021.139001

Baydilli, E. E., Tan, S. O., Tecimer, H. U., & Altındal, S. (2020). Detection of current transport mechanisms for graphene-doped-PVA interlayered metal/semiconductor structures. *Physica B Condens Matter*, *598*, 412457. doi:10.1016/j.physb.2020.412457

Bohlin, K. E. (1986). Generalized Norde plot including determination of the ideality factor. *Journal of Applied Physics*, *60*(3), 1223-1224. doi:10.1063/1.337372

Cheung, S. K., & Cheung, N. W. (1986). Extraction of Schottky diode parameters from forward current-voltage characteristics. *Applied Physics Letters*, *49*(2), 85-87. doi:10.1063/1.97359

Çaldıran, Z. (2020). Fabrication of Schottky barrier diodes with the lithium fluoride interface layer and electrical characterization in a wide temperature range. *Journal of Alloys and Compounds*, *816*, 152601. doi:10.1016/j.jallcom.2019.152601

Çiçek, O., Tecimer, H. U., Tan, S. O., Tecimer, H., Altındal, Ş., & Uslu, İ. (2016). Evaluation of electrical and photovoltaic behaviours as comparative of Au/n-GaAs (MS) diodes with and without pure and graphene (Gr)-doped polyvinyl alcohol (PVA) interfacial layer under dark and illuminated conditions. *Composites Part B: Engineering*, *98*, 260-268. doi:10.1016/j.compositesb.2016.05.042

Deniz, A. R., Taş, A. İ., Çaldıran, Z., İncekara, Ü., Biber, M., Aydoğan, Ş., & Türüt, A. (2022). Effects of PEDOT:PSS and crystal violet interface layers on current-voltage performance of Schottky barrier diodes as a function of temperature and variation of diode capacitance with frequency. *Current Applied Physics*, *39*, 173-182. doi:10.1016/j.cap.2022.03.017

Evcin Baydilli, E., Altındal, S., Tecimer, H., Kaymaz, A., & Uslu Tecimer, H. (2020). The determination of the temperature and voltage dependence of the main device parameters of Au/7%Gr-doped PVA/n-GaAs-type Schottky Diode (SD). *Journal of Materials Science: Materials in Electronics*, *31*, 17147-17157. doi:10.1007/s10854-020-03799-5

Helal, H., Benamara, Z., Arbia, M. B., Khettou, A., Rabehi, A., Kacha, A. H., & Amrani, M. (2020). A study of current-voltage and capacitance-voltage characteristics of Au/n-GaAs and Au/GaN/n-GaAs Schottky diodes in wide temperature range. *International Journal of Numerical Modelling: Electronic Networks, Devices and Fields*, *33*(4), e2714. doi:10.1002/jnm.2714

Norde, H. (1979). A modified forward I - V plot for Schottky diodes with high serial resistance. *Journal of Applied Physics*, *50*(7), 5052-5053. doi:10.1063/1.325607

Novoselov, K. S., Geim, A. K., Morozov, S. V., Jiang, D., Zhang, Y., Dubonos, S. V., Grigorieva, I. V., & Firsov, A. A. (2004). *Electric Field Effect in Atomically Thin Carbon Films*, *306*(5696), 666-669. doi:10.1126/science.1102896

Özdemir, A. F., Göksu, T., Yıldırım, N., Turut., A. (2021). Effects of measurement temperature and metal thickness on Schottky diode characteristics. *Physica B Condens Matter*, *616*, 413125. doi:10.1016/j.physb.2021.413125

Pehlivanoglu, S. A. (2021). Fabrication of p-Si/n-NiO:Zn photodiodes and current/capacitance-voltage characterizations. *Physica B Condens Matter*, *603*, 412482. doi:10.1016/j.physb.2020.412482

Rhoderick, E. H. (1978). *Metal-Semiconductor Contacts*. Clarendon Press Oxford.

Sadao, A. (2005). *Properties of Group-IV, III-V and II-VI Semiconductors*. Hoboken (USA) Wiley&Sons.

Sato, K., & Yasumura, Y. (1985). Study of forward I - V plot for Schottky diodes with high serial resistance. *Journal of Applied Physics*, *58*(9), 3655-3657. doi:10.1063/1.335750

Sevgili, Ö., Orak, İ., & Tiras, K. S. (2022). The examination of the electrical properties of Al/Mg$_2$Si/p-Si Schottky diodes with an ecofriendly interfacial layer depending on temperature and frequency. *Physica E: Low-dimensional Systems and Nanostructures*, *144*, 115380. doi:10.1016/j.physe.2022.115380

Taşyürek, L. B., Aydoğan, Ş., Sevim, M., & Çaldıran, Z. (2022). Analysis of the temperature dependent electrical parameters of the heterojunction obtained with Au nanoparticles decorated perovskite strontium titanate nanocubes. *Journal of Alloys and Compounds*, *914*, 165140. doi: 10.1016/j.jallcom.2022.165140

Uslu, H., Altındal, S., Aydemir, U., Dökme, I., & Afandiyeva, I. M. (2010). The interface states and serial resistance effects on the forward and reverse bias I-V, C-V and G/ω-V characteristics of Al-TiW-Pd 2Si/n-Si Schottky barrier diodes. *Journal of Alloys and Compounds*, *503*(1), 96-102. doi:10.1016/j.jallcom.2010.04.210

Werner, J. H., & Güttler, H. H. (1991). Barrier inhomogeneities at Schottky contacts. *Journal of Applied Physics*, *69*(3), 1522-1533. doi:10.1063/1.347243

Design, DFT Calculations and Antimicrobial Activity of New Synthesized Piperazine Derivative

Sinan Mithat MUHAMMET[1*] iD

[1]Department of Polymers Technology, Technology Sciences High School, Gazi University

Keywords	Abstract
Piperazine Derivatives DFT Calculation HOMO, LUMO Energies Antibacterial Activity MEP	The title compound (2,2'-(piperazine-1,4-diyl)bis(N'-((E)-5-chloro-2-hydroxybenzylidene) acetohydrazide) **(5-ClPAH)** was synthesized by reacting 1,4-Piperazinediacetic acid, 1,4-dihydrazide and 5-Chloro-2-hydroxybenzaldehyde. Mass spectrometry, ^{1}H, ^{13}C-NMR, IR results of the synthesized compound were examined. Many information about physical and chemical properties of **5-ClPAH** can be obtained by theoretical calculations. Density functional theory (DFT) is widely used theoretical method for predicting of chemical structures. The structure was optimized using DFT/6311G method with GAUSSIAN09. Frontier Molecular Orbitls (HOMO and LUMO) energies were calculated. Global reactivity descriptors and also electrophilic and nucleophilic regions were defined by molecular electrostatic potential surface. Antibacterial and fungal activity were evaluated.

1. INTRODUCTION

The imine group (azomethine) of Schiff bases attracted much attention due to widely usage in biological studies and which was use in chemistry (Venkataramana et al., 2010; Yan et al., 2012; Gupta & Goklani, 2017; Ermiş & Durmuş, 2020). Piperazine ring is also an important class of N-heterocyclics having biological activities including antitumor (Xu et al., 2019), antiviral drugs (Hooshmand et al., 2021), antibacterial (Jalagari et al., 2019) and antifungal etc (Suryavanshi & Rathore, 2017) and pharmaceutical applications (Ullh et al., 2022). Piperazine derivatives have been widely used in the production of new drugs in recent years (Shaquiquzzaman et al., 2015).

In this paper, titled compound (5-ClPAH) was obtained and structural characterized by elemental analyses, IR, mass spectrometry, ^{1}H, ^{13}C-NMR NMR methods. Antibacterial activity against six bacteria [*B.cereus* 709 ROMA, *S. aureus* ATCC 29213, *K. pneumonia* ATCC 13883,*P. aeruginos*a ATCC 27853, *S. aureus* ATCC 25923, *E. coli* ATCC 25922] was conducted. Microdilution (as MICs) and disc diffusion method were used to determine the antibacterial activity. Morever, the 5-ClPAH was evaluated for the activities against three fungal pathogens (*C. tropicalis* M002, *C. parapsilosis* M006 and *C. albicans* ATCC 80018) by agar well diffusion technique. The structure-activity relationship (SAR) of the5-ClPAH was also analysized in the present work. Frontier molecular orbital energies (FMOs), Global reactivity descriptors and MEP were studied at B3LYP/6-311G level of theory.

*Corresponding Author, e-mail: mithat@gazi.edu.tr

2. MATERIAL AND METHOD

2.1. Physical Measurements

Used chemicals were purchased from Merck (with high purifitiy). Fourier Transform Infrared spectra of the was performed between 400 and 4000 cm^{-1} from KBr pellets on. NMR spectras were carried out by Bruker-Spectrospin Avance DPX-400 Ultra-Shıeld (using d6-DMSO solvent). Mass spectrometry was recorded on an Agilent 6470 QQQ LC-MS/MS @ 1290 INF HPLC. The m.p. values were determined using an Opti Melt apparatus. All reactions were watched using Merck silica gel (60 F 254) by thin-layer chromatography (TLC). The elemental analysis was implemented out on a LECO CHNS 9320 type analyzer.

2.2. Synthesis of 2, 2'-(piperazine-1,4-diyl)bis(N'-((E)-5-chloro-2-hydroxybenzylidene)aceto hydrazide (5-ClPAH)

The solution of 1,4-piperazinediacetic acid, 1,4-dihydrazide (0,9 g, 4.5 mmol) (Koparde et al., 2018) in 25 mL of water- ethanol (1-4 rate) was slowly added with hot solution (50 ºC) of 5-Chloro-2-hydroxy-benzaldehyde (1.4g, 8.9 mmol) in 30 mL of ethanol and refluxed for 24 h. Reactions were watched by TLC. The precipitated product was cooled to room temperature an ~ 23ºC to crystallized from the ethanol/water (4:1) mixture and dried in vacuo. The reaction equation was given Figure 1. Yield 87%. M.p. 198-199ºC. LC-MS (100 eV, APCl): 507.8 (M+H$^+$, 100%), 507.2 (M+, 82%), IR (KBr) v/cm^{-1}: 2931 cm^{-1},C-H aliph; 3066, C-H arom.; 3187 , N-H. Elemental analysis for C$_{22}$H$_{24}$Cl$_2$N$_6$O$_4$ (MW:507.37 g/mol) (Calc.%) C: 52.08; H: 4.77; N; 16.56; Cl; 13.97, O; 12.61. (Found %) C, 51.01; H, 5.11; N, 17.04; O, 12.41; Cl, 14.44.
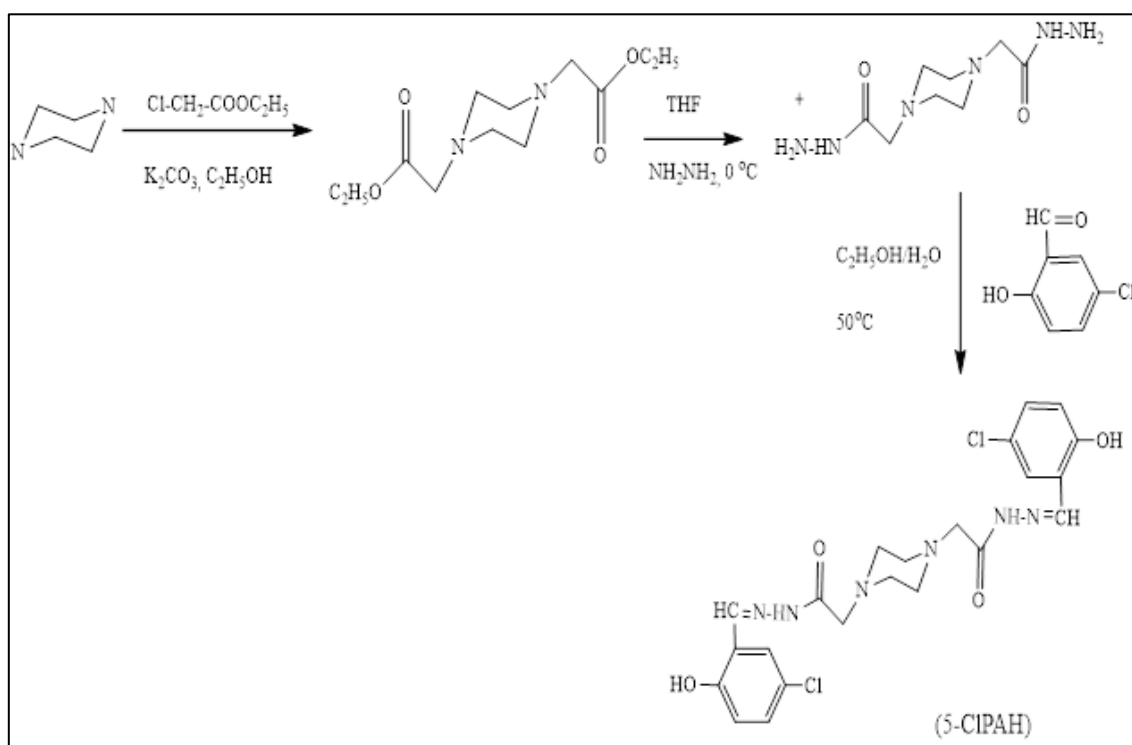
Figure 1. Preparation of 5-ClPAH

2.3. Procedure for Antibacterial Activity

Patogen bacterial cultures incubated for 24 hour at 37°C were acquired from Biology Department of Kırsehir Ahi Evran University.

The little discs 6 mm in diameter were treated with 50 μg Schiff bases and then were located on test plates. The paper discs containing 30 μg streptomycin and 50 μg Ampisilin were used as standard drugs. The **5-ClPAH** were tested against microorganisms three times and the activated zones were detected after a day (Luis Esaú et al., 2019).

A serial concentration was prepared by thin out the stock solution with 20 %DMSO solvent: 1250, 625, 312.5, 156.25, 78.125, 39.06, 19.53, 9.76, 4.88 µg mL^{-1}. After incubation at 37ºC for 24 h of the MIC of against microbial strain was defined by macroscopic observation (Koneman et al., 1997).

2.4. Antifungal activity (*in vitro*)

Candida albicans ATCC 80018, *Candida tropicalis* M002 and *Candida parapsilosis* M006 strains were obtained from Biology Department of Kırsehir Ahi Evran University. *In vitro,* antifungal activite was studied using agar well diffusion method (Suryavanshi & Rathore, 2017). The 50 µL of microbial suspension was disseminated over plate containing agar surface. The 5-ClPAH and standard drugs Ampisilin and Streptomycin were incubated at 303 K for 48 h.

2.5. Computation details

Molecular modeling of the compound was carried out by Gaussian 09 (Frisch et al., 2009) program using DFT/B3LYP (Prasad et al., 2022) density functional theory with 6-311G (Foresman & Frisch, 1996) base set and semi-emprical theory with AM1 (Austin Model 1) (Dewar et al., 1985) base set. HOMOs and LUMOs as frontier molecular orbitals computed by DFT method play a important role in the chemical reactivities, stabilities and electronic transition levels of molecules (Dennington et al., 2016).

3. RESULT AND DISCUSSION

3.1. Structure of the 5-ClPAH

IR spectrum of **5-ClPAH** is shown in Figure 2. As seen in Figure 2, a characteristic O-H stretching band is observed at 3344,40 cm^{-1}. Other stretching bands are observed at 3187 cm^{-1} (N-H), 3066 cm^{-1} (CH: aromatic), 1688cm^{-1} (C=O; amide), 1512 cm^{-1} (C=C: aromatic), 1294 cm^{-1} (C-N).
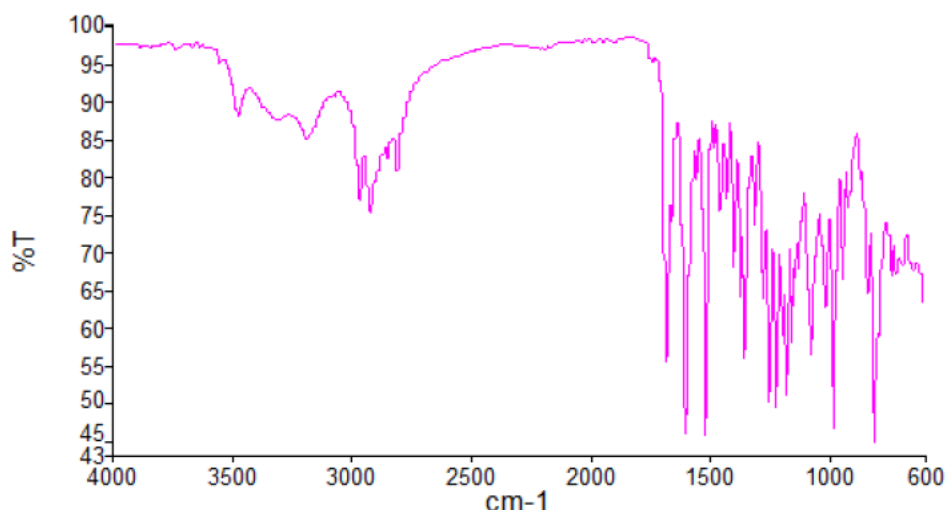
Figure 2. IR spectrum of 5-ClPAH

The NMR spectrums (^{1}H, ^{13}C) of 5-ClPAH were obtained and interpreted in *d6* –DMSO. In ^{1}H-NMR, the protons of piperazine appeared at 2.38 (m, 4H) and 2.62 (m, 4H) ppm respectively. The protons belonging to N=CH (8.4 ppm), and C-NH (11.2–11.51 ppm) were detected a singlet. The aromatic-H peaks were observed between 6.94-7.60 ppm.

In ^{13}C NMR of Schiff base, piperazine ring peak and azomethine CH=N carbon peak were observed at 53.60 ,163.5 ppm, respectively. The aromatic-C peaks were also observed between 107.7-156.5 ppm.

The mass spectrum of 5-ClPAH is presented in Figure 3. Molecular ion [M+H]$^{1+}$peak is observed as base peak at 507.8 (m/z). The main peaks (82%), [M$^+$] at (m/z) 507.2 and (75%), [M+3H]$^+$.at (m/z) 509.8 are observed.
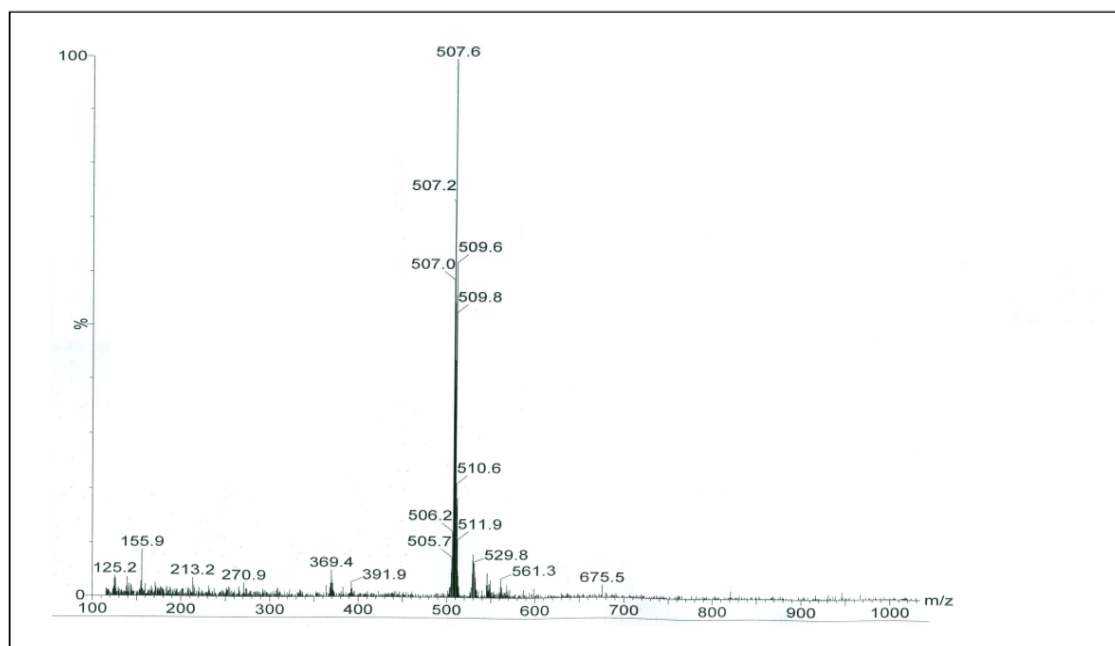
*Figure 3. Mass spectrum of **5-ClPAH***

3.2. Antimicrobial activity results

The tested strains selected for this study were categorized as three Gram negative bacteria (*E. coli*, *K. pneumoni*, *P. aeruginosa*), three Gram positive bacteria (*S. aureus**,*B. cereus*, *S. aureus*) and three fungi (*C. tropicalis*, *C. albicans* and *C. parapsilosis*). The 5-ClPAH was dissolved in DMSO (20%) at proper concentration.The antibacterial results were given in Table 1, Table 2 by MICs and disc diffusion, respectively. The positive control used in this study as antibacterial and antifungal agents is Ampisilin, and Streptomycin and were compared **(**Figure 4**).**

As the disc diffusion technique results show that the compound exhibits a moderate inhibition effect against tested all bacteria. The compound was significant activity against *P. aeruginosa* ATCC whereas Ampisilin and Streptomycin, the drugs used as standart, have been determined a bit active (10-12 mm) against the six bacteria.

Table 1. Measured diameter (mm) of the compounds

Compounds	Gram-negative			Gram-positive		
	K.pneumonie ATCC 13883	*E.coli* ATCC 25922	*P.aeruginoa* ATCC 27853	*B. cereus* Roma 709	*S. aureus* ATCC 29213	*S.aureus* ATCC 25923
5-ClPAH	15	15	16	10	10	8
Streptomycin	12	20	10	15	18	19
Ampisilin	12	16	12	15	18	18
<10: weak; >10: moderate; >16: significant Ampisilin (50 µg/disk) Streptomycin (30 µg/disk)						
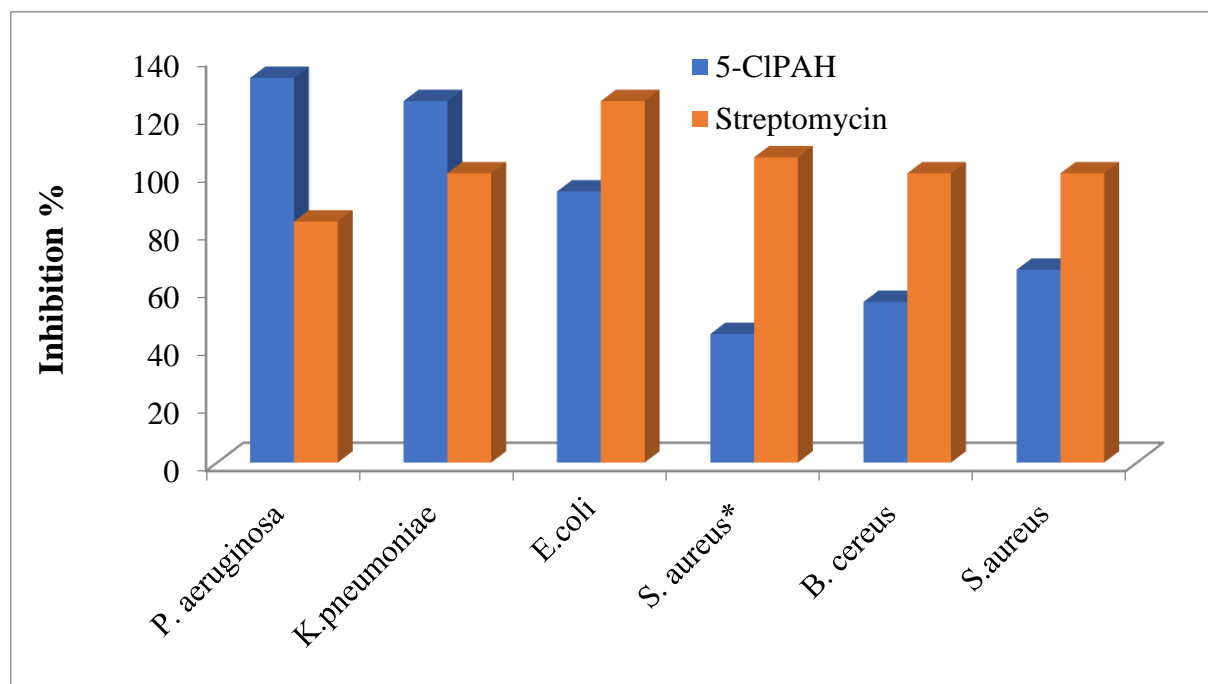
Figure 4. *Percentage of inhibition of 5-ClPAH and Streptomycin against Ampisilin*

The percentage of inhibition for 5-ClPAH molecule and standard drug Streptomycin showed in Figure 4. The 5-ClPAH molecule and Streptomycinshow good activity against Gram-negative *K. pneumonia* (125% 100%), respectively (Ampisilin was accepted 100% inhibition).

The 5-ClPAH molecule showed excellent inhibiting activity against bacterial strains with MIC value less than that of standard drugs Ampisilin and Streptomycin. The 5-ClPAH molecule was excellent inhibition (MIC=78.12 µg/mL) against *S. aureus* ATCC 25923 and *S. aureus* ATCC 29213.

Table 2. *The MICs (**µg/mL**), (**mM**) of antibacterial activity of 5-ClPAH and standard drugs*

Bacteria strain	MICs *µg/mL (mM)*		
Gram- negative	**5-ClPAH**	**Ampisilin**	**Streptomycin**
P. aeruginosa ATCC 27853	156.25 **(0.308)**	93.75 **(0.268)**	93.75 **(0.161)**
E. coli ATCC 25922	156.25 **(0.308)**	93.75 **(0.268)**	46.87 **(0.0806)**
K.pneumoniae ATCC 13883	156.25 **(0.308)**	93.75 **(0.268)**	93.75 **(0.161)**
Gram-positive			
S. aureus ATCC 29213	78.125 **(0.154)**	46.87 **(0.134)**	46.87 **(0.0806)**
B. cereus Roma 709	156.25 **(0.308)**	93,75 **(0.268)**	93.75 **(0.161).**
S. aureus ATCC 25923	78.125 **(0.154)**	46,87 **(0.134)**	46.87 **(0.0806)**

The antifungal stud of the 5-ClPAH molecule was carried out *Candida tropicalis* M002, *Candida parapsilosis* M006 and *Candida albicans* ATCC 80018 fungal strains (Table 3) (Rahman et al., 2001). The antifungal activity results of Schiff base and standard drugs; Ampisilin and Streptomycin were exhibited in Table 3 (Figure 5). From the antifungal activity results, 5-ClPAH exhibited excellent inhibition against *Candida albicans*, *Candida parapsilosis* and *Candida tropicalis* with disk 10-22 mm than the standard drugs Ampisilin (7-8 mm), Streptomycin (10-12mm). As seen in Figure 5, The 5-ClPAH showed excellent activity against *C.albicans* (214.28 %) *C. parapsilosis* (314.28%) and *C. glabrata* (125%).

***Table 3.** Inhibition zone diameter (mm) of 5-ClPAH and standard drugs*

Compounds	Zone of Inhibition (mm)		
	Candida tropicalis M002	*Candida parapsilosis M006*	*Candida albicans ATCC 80018*
5-ClPAH	10	22	15
Streptomycin	12	11	10
Ampisilin	8	7	7

The HOMOs and LUMOs which are responsible for chemical reactivities are known as the FMO. HOMO is the highest energy filled molecular orbital and LUMO is the lowest energy vacant molecular orbital. HOMO represents the desire to donate an electron while LUMO represents the desire to gain an electron (Fleming, 2010; Benabid et al., 2020). HOMO and LUMO have been carefully evaluated to understand the ligand reaction and to specify the reactive sites. These orbital energy levels are used to determine intermolecular charge transfers, and to calculate Global reactivity descriptors such as electron affinity, electronegativity, electrophilicity index, potential chemical reactivity and ionization (Ayers & Parr, 2008; Sultan et al., 2016; Oueslati et al., 2019). The energies of HOMO and LUMO orbitals of *5-ClPAH* molecule are -8,01eV and -5.52 eV, respectively. The HOMO and LUMO orbital energy gap ($\Delta E: E_{HOMO}-E_{LUMO}$) calculated using B3LYP/6311G method is 2,49 eV(Table 4, Figure 6). The values of global softness (S), ionisation potential (IP=-HOMO), electronegativity (χ), electron affinity (EA=-LUMO), chemical hardness (η), and electrophilicity index (ω) for **5-ClPAH** molecule at B3LYP/6311 basis are given in Table 4.
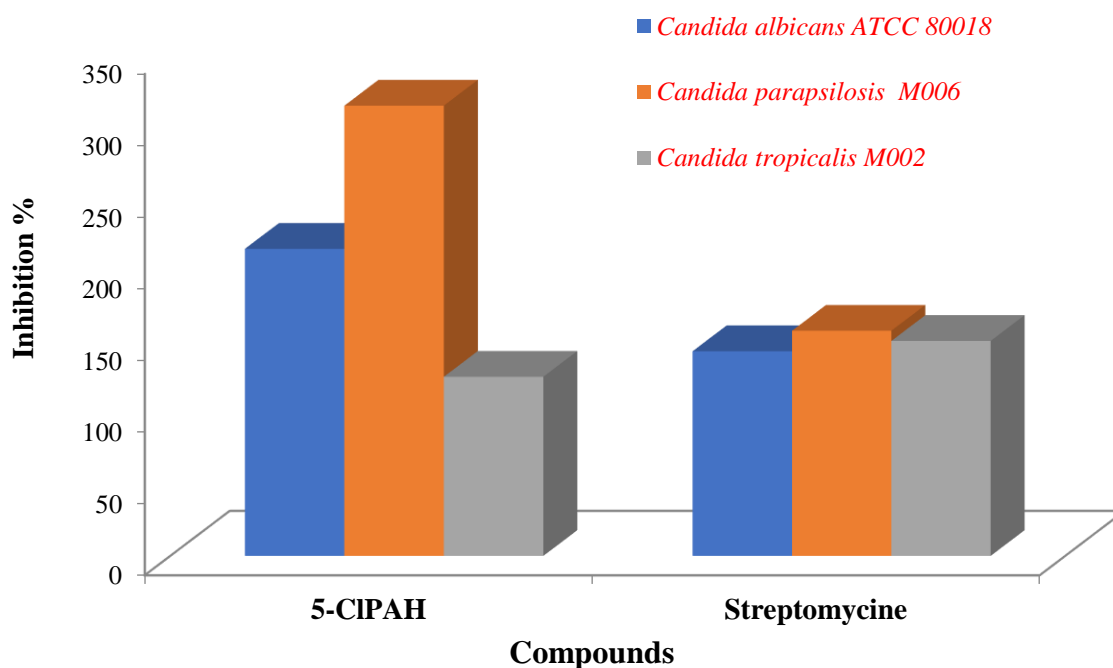
***Figure 5.** Percentage of inhibition of 5-ClPAH and Streptomycin against Ampisilin*

Table 4. *The Traditional and Chemical Reactivity Descriptors of 5-ClPAH obtained using B3LYP with 6311G basis set*

Molecular Properties (eV)	a.u.	ev
E_{LUMO}	-0.20	-5.52
E_{HOMO}	-0.29	-8.01
$\Delta E_{HOMO\text{-}LUMO}$	-0.09	-2.49
IP	0.29	8.01
EA	0.20	5.52
η	0.05	1.25
χ	0.25	6.76
μ	-0.25	-6.76
S (ev⁻¹)	10.92	297.06
ω	0.67	18.35

The MEP diagram for ***5-ClPAH*** molecule was shown in Figure 7. The red colors in the MEP indicates showing electrophilic reactivity Whereas the blue colors in the MEP show nucleophilic reactivity. From the MEP of the molecule, the positive and negative potential sites occur over nitrogen (N12, N16, N21,N34) and oxygen (O8, O11, O20) atoms, respectively.

-2,49 eV

-8,01eV   **- 5,52eV**

HOMO   **LUMO**
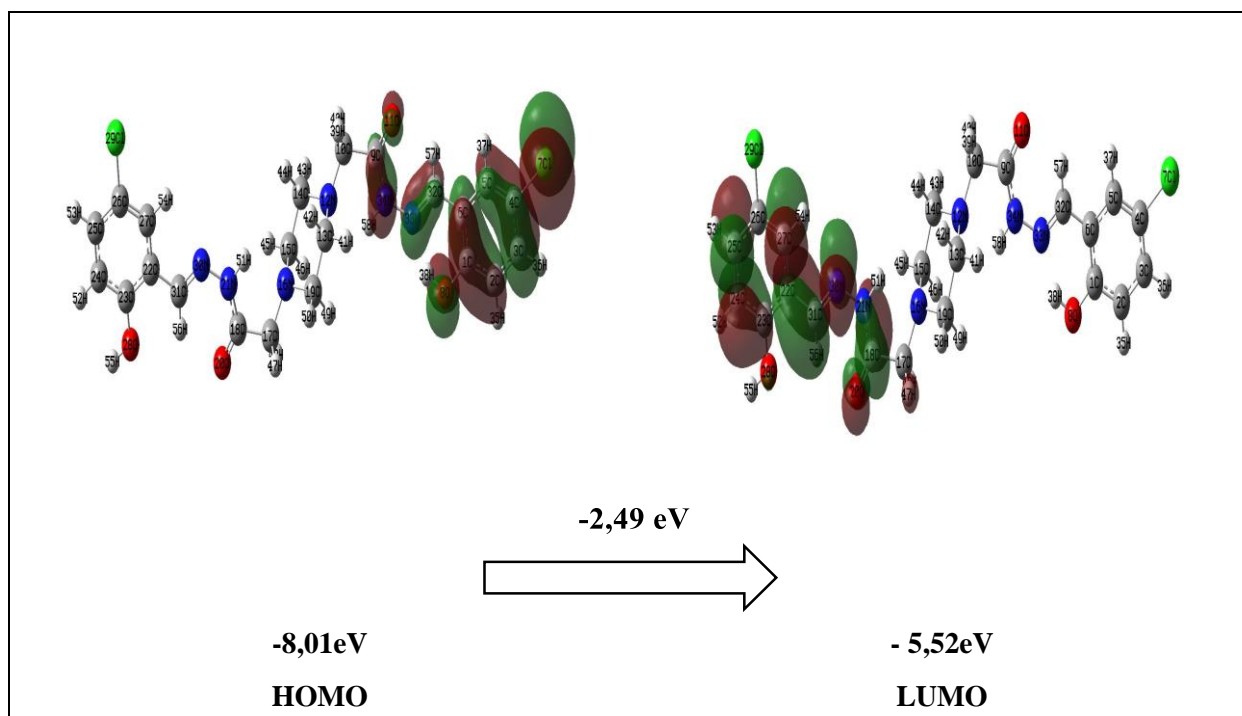
Figure 6. *Representation of Frontier orbitals of **5-ClPAH** molecule*
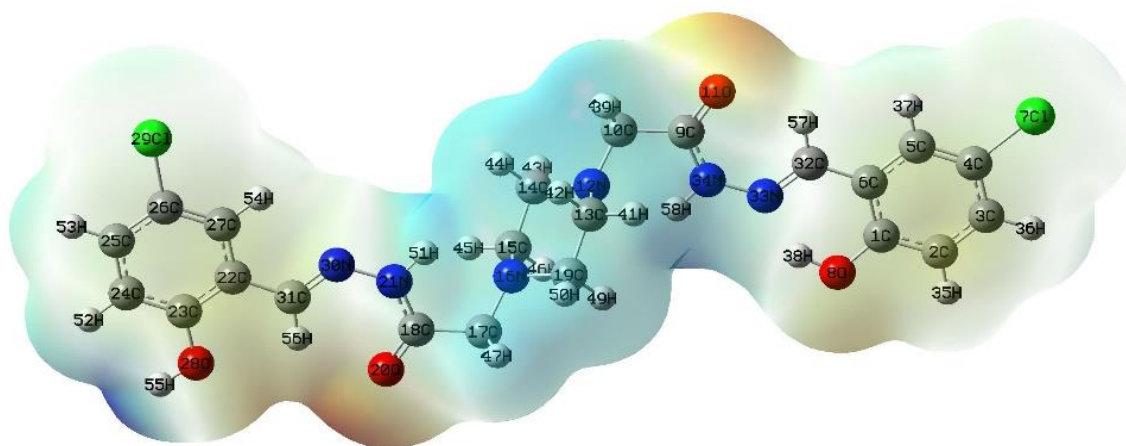
Figure 7. Derived MEP surface analysis representation of 5-ClPAH molecule

4. CONCLUSION

In this study, 5-ClPAH molecule with the chemical formula $C_{22}H_{24}Cl_2N_6O_4$. was synthesized and characterized. DFT based calculations were used to theoretically analyze the 3D optimized structure of 5-ClPAH molecule. The HOMO and LUMO energies were used to predict quantum chemical properties like hardness, electrophilicity and softness. Stable structure of 5-ClPAH molecule was obtained by PES analysis. The HOMO energy gap value for 5-ClPAH molecule was found to be -8.01 eV at B3LYP/6-311 G level of theory. In vitro biological tests show that 5-ClPAH molecule have moderate efficacy as antibacterial and antifungal reagents.

CONFLICT OF INTEREST

The author declares no conflict of interest.

REFERENCES

Ayers, P. W., & Parr, R. G. (2008). Local hardness equalization: Exploiting the ambiguity. *The Journal of Chemical Physics*, *128*(18), 184108. doi:10.1063/1.2918731

Benabid, W., Ouari, K., Bendia, S., Bourzami, R., & Ali, M. A. (2020). Crystal structure, spectroscopic studies, DFT calculations, cyclic voltammetry and biological activity of a copper (II) Schiff base complex. *Journal of Molecular Structure*, *1203*, 127313. doi:10.1016/j.molstruc.2019.127313

Dennington, R., Keith, T. A., & Millam, J. M. (2016). *GaussView 6.0. 16*. Semichem Inc.:Shawnee Mission, KS, USA.

Dewar, M. J. S., Zoebisch, E. G., Healy, E. F., & Stewart, J. J. P. (1985). Development and Use of Quantum Mechanical Molecular Models. 76. AM1: A New General Purpose Quantum Mechanical Model. *J. Am. Chem. Soc.*, *107*(13), 3902-3909. doi:10.1021/ja00299a024

Ermiş, E., & Durmuş, K. (2020). Novel thiophene-benzothiazole derivative azomethine and amine compounds: Microwave assisted synthesis, spectroscopic characterization, solvent effects on UV–Vis absorption and DFT studies. *Journal of Molecular Structure*, *1217*, 128354. doi:10.1016/j.molstruc.2020.128354

Fleming, I. (2010). *Molecular Orbitals and Organic Chemical Reactions, Reference Edition*. John Wiley & Sons. doi:10.1002/9780470689493

Foresman, J. B., & Frisch, A. (1996). *Exploring Chemistry with Electronic Structure Methods*. 2nd Edition. *Gaussian Inc*., Pittsburgh.

Frisch, M. J., Trucks, G. W., Schlegel, H. B., Scuseria, G. E., Robb, M. A., Cheeseman, J. R., Scalmani, G., Barone, V., Mennucci, B., & Petersson, G. A. (2009). *Gaussian 09, revision a. 02*, gaussian. Inc., Wallingford.

Gupta, A., & Goklani, P. (2017). Synthesis and Characterization of Various Alkyl, Aryl and Hetero Aryl Substituted Hydrazines and Study of their Biological Activity. *Oriental Journal of Chemistry*, *33*(2), 1041-1044. doi:10.13005/ojc/330262

Hooshmand, S. A., Ghobadi, M. Z., Hooshmand, S. E., Jamalkandi, S. A., Alavi, S. M., & Masoudi-Nejad, A. (2021). A multimodal deep learning-based drug repurposing approach for treatment of COVID-19. *Mol. Divers.*, *25*(3), 1717-1730. doi:10.1007/s11030-020-10144-9

Jalageri, M. D., Puttaiahgowda, Y. M., Parambil, A. M., & Kulal, A. (2019). Design of multifunctionalized piperazine polymer and its activity toward pathogenic microorganisms. *Journal of Applied Polymer Science*, *136*(19), 47521. doi:10.1002/app.47521

Koneman, E. W., Allen, S. D., Janda, W. M., Schreckenberger, P. C., & Winn Jr., W. C. (1997). *Color Atlas and Textbook of Diagnostic Microbiology*. 5th Edition. JB Lippincot Company.

Koparde, S., Hosamani, K. M., Kulkarni, V., Joshi, D. S. (2018). Synthesis of coumarin-piperazine derivatives as potent anti-microbial and anti-inflammatory agents, and molecular docking studies. *Chemical Data Collections*, *15-16*, 197-206. doi:10.1016/j.cdc.2018.06.001

Luis Esaú, L.-J., Christian Rodolfo, R.-G., Melissa, H.-D., Claudia Adriana, C.-C., Rodolfo, G.-C., & Rafael, F.-C. (2019). An alternative disk diffusion test in broth and macrodilution method for colistin susceptibility in Enterobacteriales. *Journal of Microbiological Methods*, *167*, 105765. doi:10.1016/j.mimet.2019.105765

Oueslati, Y., Kansız, S., Valkonen, A., Sahbani, T., Dege, N., & Smirani W. (2019). Synthesis, crystal structure, DFT calculations, Hirshfeld surface, vibrational and optical properties of a novel hybrid non-centrosymmetric material (C10H15N2)2H2P2O7. *Journal of Molecular Structure*, *1196*, 499-507. doi:10.1016/j.molstruc.2019.06.110

Prasad, H. S. N., Ananda, A. P., Lohith, T. N., Prabhuprasad, P., Jayanth, H. S., Krishnamurthy, N. B., Sridhar, M. A., Mallesha, L., & Mallu, P. (2022). Design, synthesis, molecular docking and DFT computational insight on the structure of Piperazine sulfynol derivatives as a new antibacterial contender against superbugs MRSA. *Journal of Molecular Structure*, *1247*, 131333. doi:10.1016/j.molstruc.2021.131333

Rahman, A.-u., Choudhary, M. I., & Thomsen, W. J. (2001). *Bioassay Techniques for Drug Development*. Harwood Academic Publishers, The Netherlands.

Shaquiquzzaman, M., Verma, G., Marella, A., Akhter, M., Akhtar, W., Khan, M. F., Tasneem, S., & Alam, M. M. (2015). Piperazine scaffold: A remarkable tool in generation of diverse pharmacological agents. *European Journal of Medicinal Chemistry*, *102*, 487-529. doi:10.1016/j.ejmech.2015.07.026

Sultan, M. A., Karama, U., Almansour, A. I., & Soliman, S. M. (2016). Theoretical study on regioselectivity of the Diels-Alder reaction between 1,8-dichloroanthracene and acrolein. *Molecules*, *21*(10), 1277. doi:10.3390/molecules21101277

Suryavanshi, H. R., & Rathore, M. M. (2017). Synthesis and biological activities of piperazine derivatives as antimicrobial and antifungal agents. *Org. Commun.*, *10*(3), 228-238. doi:10.25135/acg.oc.23.17.05.026

Ullh, Z., Al-Otaibi, J. S., Mary, Y. S., & Kwon, H. W. (2022). Computational study of furosemide-piperazine (FS – PZ) and 2,3,5,6-tetramethylpyrazine (FS-TP) co-crystals. *Journal of Molecular Liquids*, *360*, 119537. doi:10.1016/j.molliq.2022.119537

Venkataramana, H. S. C., Singh, A., Tiwari, A., & Tiwari, V. (2010). Synthesis of Phenyl Hydrazine Substituted Benzimidazole Derivatives and Their Biological Activity. *International Journal of Pharmaceutical Sciences and Research*, *1*(1), 34-38. doi:10.13040/IJPSR.0975-8232.1(1).34-38

Xu, Y., Liang, P., Rashid, H. ur, Wu, L., Xie, P., Wang, H., Zhang, S., Wang, L., & Jiang, J. (2019). Design, synthesis, and biological evaluation of matrine derivatives possessing piperazine moiety as antitumor agents. *Medicinal Chemistry Research*, *28*(10), 1618-1627. doi:10.1007/s00044-019-02398-2

Yan, T., Yu, S., Liu, P., Liu, Z., Wang, B., Xiong, L., & Li, Z-m. (2012). Design, Synthesis and Biological Activities of Novel Benzoyl Hydrazines Containing Pyrazole. *Chinese Journal of Chemistry*, *30*(4), 919-923. doi:10.1002/cjoc.201100347

Risk Analysis of Natech Accidents Trigged by Lightnings and Floods

Meryem Merve KURT[1] (iD) Saliha ÇETİNYOKUŞ[2]* (iD)

[1]Gazi University, Graduate School of Natural and Applied Sciences, Environmental and Technical Research of Accidents, Ankara, Türkiye
[2]Gazi University, Faculty of Engineering, Chemical Engineering, Ankara, Türkiye

Keywords	Abstract
Natech Acidents	Natural Hazard Triggered Technical Accidents (Natech) cause serious loss of life, environment and property and affect life negatively. Risk analysis studies of these accidents are important. In this study, it was aimed to analyze the risk of Natech accidents for Türkiye. Statistical evaluation of Natech accidents was made through various databases for selecting the province and organization where the application will be made. Because of these evaluations, two exemplary gas storage organizations (Organization 1: includes 5 cylindrical tanks of the same volume, Organization 2: includes 4 cylindrical tanks of the same volume and 1 large volume spherical tank) were selected within the scope of the legislation in Erzurum, which stands out in terms of flood and lightning risk. Flood-triggered Natech accidents were analyzed using the preliminary hazard list and Fine-Kinney methods, and lightning-triggered Natech accidents were analyzed through the YILKOMER and RADSAN programs. For Organization 1 and Organization 2, the protection level was determined as 3 and 4, respectively, according to the effectiveness value. While 34 hazard effects were graded with the preliminary hazard list for Organization 1 and 22 hazard effects by Fine-Kinney; for Organization 2, hazard effects were graded 37 with the preliminary hazard list and 28 with Fine-Kinney. Because of the analyses carried out, Organization 2 was found to be more risky in terms of Natech accidents triggered by both lightning and flooding. It can be said that this situation is because the relevant organization is located in a more congested area and within the organized industry, and that it contains more voluminous tanks. It is important that emergency plans be prepared by considering the Natech risks, based on the characteristics of the industrial facility and the type of natural disaster in the region.
Risk Analysis	
Lightning	
Floods	

1. INTRODUCTION

A disaster is defined as a natural, technological, or human-induced event that affects the whole or a certain part of the society, cause economic, social and physical losses in the society, interrupts normal life, and in which the local opportunities are insufficient. Natural hazards such as earthquakes, floods, storms, extreme temperatures can trigger fires, explosions, toxic or radioactive releases in facilities that process, store, or transport hazardous materials, and these are called Natural Hazard Triggered Technical Accidents (Natech) (eNatech, 2022). Natech causes serious life, economic and environmental losses. Natech risk assessment is extremely important to identify areas where such accidents can occur, to identify possible risks and to take the necessary measures to reduce risk. In Türkiye, with the Gölcük Earthquake on August 17, 1999, a fire occurred in TÜPRAŞ and it was determined that there were 80 million dollars of damage because of the fire. Then, because of the LPG explosion in Akçagaz in July 2002, 3 trillion Turkish liras damage occurred (Çetinyokuş, 2018; Güneş & Çetinyokuş, 2020). The increase in industrial facilities and population in the risky area will increase the damage that may occur in the region in case of disaster (Krausmann & Musthaq, 2008). This situation reveals the importance of planning and supervised settlement.

*Corresponding Author, e-mail: salihakilicarslan@gazi.edu.tr

There is no special regulation for Natural Hazard Triggered Technical Accidents in Türkiye. However, Natural Hazard Triggered Technical Accidents can be evaluated within the scope of the "Regulation on the Prevention of Major Industrial Accidents and Reduction of Their Effects" prepared and published on March 2, 2019 by the Ministry of Family, Labor and Social Services, the Ministry of Environment and Urbanization and the Ministry of Interior (Official Gazette, 2019) .The regulation emphasizes the necessity of considering natural disasters in the determination of industrial accident risks in the relevant annexes.

Studies on the analysis of Natech accident data are remarkable. The trend of Natech events, their geographical distribution, final technological scenarios were evaluated in terms of life and property losses by Ricci et al. (2021). In the study, data were analyzed using eMARS, MHIDAS, NRC, TAD IChemE, ARIA and CONCAWE databases. In another study by Ricci et al. (2020), the trend of Natech accidents caused by cold air and heat waves over the years was evaluated in terms of geographical location, final scenarios and related industrial sectors, through ARIA, eMARS, MHIDAS and FACTS databases. Moreno et al. (2019) analyzed the data of accidents affecting the chemical and process industry through ARIA, FACTS and eMARS databases by grouping them in terms of geographical location, type of disaster that triggered and type of asset affected, and graphs were obtained. The ARIA, NRC, MHIDAS, FACTS, MARS and TAD databases were used by Renni et al. (2010) to contribute to the development of a quantitative approach for assessing lightning risk in industrial facilities. The data obtained were evaluated according to the criteria of loss of hazardous materials, industrial activity containing hazardous materials, major accident scenarios on or off the field. Krausmann and Musthaq (2008) analyzed past cases and used expert opinions to demonstrate major flood-induced technological damage or failure pathways that have the potential to cause hazardous material releases. The potential impact of flood severity on specific industrial facilities that store and/or process toxic, flammable, or explosive materials has been qualitatively analyzed.

It is seen that different methods are used for risk assessment and analysis of Natech accidents in the literature. In the study by Wang and Weng (2021), a simplified methodology is presented to quickly assess the vulnerability of atmospheric storage tanks in Natech events. In this study, deterministic and probabilistic analyzes were applied using Uncertain Parameter Set (UPS) and Monte Carlo Simulation methods. Girgin et al. (2019) demonstrated that the National Risk Assessment (NRA) can be developed in the assessment of Natech risks, and although it is national, it can be evaluated to a lesser extent regionally. Naderpour et al. (2019) used Geographic Information System (GIS) based analysis to predict the amount of air and humidity in forest fires according to the probability of fire and to model Natech events. In the study by Olivar (2018), the vulnerability of industrial storage equipment that may be exposed to Natech events was analyzed with a computer tool called Natech Tank Analyzer (NaTanks). A methodology for Quantitative Risk Assessment (QRA) of lightning-induced accidents was developed by Necci et al. (2016). To this end, a model was created to assess the probability of lightning strikes on process equipment and certain equipment vulnerability models and combined these into event trees that allow the measurement of risk indices. Hazardous liquid pipeline system incidents on land reported to The Pipeline and Hazardous Materials Safety Administration (PHMSA) by Girgin and Krausmann (2016) were investigated using data mining.

In this study, it is aimed to analyze the risk of Natech Accidents, which has not been studied before in Türkiye. For this purpose, first, Natech accidents were analyzed through various disaster/accidents databases, and then sample industrial organizations that had obligations on the relevant legal legislation were determined. Then, risk analysis was carried out by using various risk analysis methods for Natech accidents triggered by floods and lightning. The results obtained were compared and organizations were evaluated in terms of Natech risk.

2. MATERIAL AND METHOD

The study started with the analysis of Natech accidents that occurred in the last 15 years through various databases, and the dominant natural disaster types and the process equipment they affected were evaluated. Then, the selection of provinces and organizations, which include the prominent types of natural disasters and process equipment, and where risk analysis studies will be conducted, were made. In the last stage, risk analysis studies of Natech accidents were conducted in selected organizations using different risk analysis methods.

Statistical Evaluation of Natech Accidents

For the statistical evaluation of Natech accidents, eMARS, EM-DAT and eNatech databases were analyzed and Natech accidents that occurred between 2006–2021 were determined.

Selection of Provinces and Organizations for Risk Analysis

The types of natural disasters and the equipment affected by Natech accidents were evaluated. The province containing these disaster types in Türkiye and the organizations in this province hosting the mentioned equipment types within the scope of the relevant Regulation was selected (Official Gazette, 2019).

Risk Analysis of Natech Accidents Triggered by Lightning in Organizations

Natech accidents triggered by lightning were analyzed in selected organizations with the YILKOMER and RADSAN programs. It has been observed that the YILKOMER risk analysis program has been put into practice for the Faraday cage and the RADSAN (2021) risk analysis program has been put into practice for the lightning rod system. The assumption of both programs is to reach the efficiency level of the systems on the facility in the event of a lightning strike. In the lightning risk calculation, the structure, environmental condition, occupancy, structural features, usage parameters are considered. The analysis is carried out through the formulas defined in the program by processing the height, length, width and number of lightning days of the area to be studied. Everything is defined and clearly stated in the program. This provides ease of use. Parameters for the program are listed in Table 1.

Table 1. *Parameters in the program*

		Environmental Coefficients (C1)		
C1	0.25	If the structure is the same or between higher trees and structures		
	0.5	if it is surrounded by buildings of low height		
	1	If the distance to the nearest building is 3h		
	2	If it is the highest in the area		
		Structural Coefficients (C2)		
C2	Structure/Roof	Metal	Brick	Flammable/Combustible
	Metal	0.5	1	2
	Brick/Concrete	1	1.5	2.5
	Flammable	2	2.5	3
		Structural Coefficients (C3)		
C3	0.5	Insignificant, Non-Flammable		
	1	Normal, Flammable		
	2	Important, Flammable		
	3	Flammable, Combustible		
		Building Occupancies (C4)		
C4	0.5	Unemployed building		
	1	Normal crowd		
	3	Risky of panic, difficulty evacuating		
		Building Occupancies/Lightning Results (C5)		
C5	1	No continuous use, worthless in the environment		
	5	In continuous use, worthless in the environment		
	10	Valuable in the environment		

C1 Environmental Coefficient is the parameter of the location of the building in the environment relative to the buildings and trees close to the building. It was evaluated from 0.25 to 2. C2 Structural coefficient is the coefficient parameter of the building according to the type of material used in the construction phase and the type of roof. C3 Structural coefficient is the parameter in which the fire risk of the building is determined. It was evaluated from 0.5 to 3. C4 Building Occupancy is the parameter of the building's hazard status for people. It was evaluated from 0.5 to 3. C5 Structure Occupancy/Lightning Result is used for the Faraday cage. The parameter evaluates the importance of a building in the environment from 1 to 5.

Within the Efficiency and Protection parameter, the efficiency level of the system used as a maximum of 0.98 and a minimum of zero is classified as the protection level and area of effect. The scenario with the strongest lightning strikes with a current value of 200 kA at protection level 1 is considered. Such strong lightning strikes are rarely experienced in Türkiye. Petrochemical plants located in areas that receive strong lightning strikes are in the high hazard class. Protection level 2 covers lightning strikes with a current value of 150 kA. Incoming strong blows involve a high risk for buildings from hospitals to factories. Protection levels 3 and 4 cover lightning strikes with a current rating of 100 kA. Many regions in Türkiye frequently receive lightning strikes of this strength; industrial enterprises and factories in these regions carry serious risks (YILKOMER, 2022).

Lightning current parameters according to the protection levels within the scope of the Lightning Protection Regulation are given in Table 2. The peak value of the current I(kA) parameter is the highest value of the lightning current, the total electric charge Q_{top} (C) parameter is the electron charge in the lightning occurring between the opposite electrically charged cloud and the ground, the pulse electric charge Q_{pulse} (C) parameter is the electron charge of the effect resulting from the lightning strike. The specific energy parameter expresses the time integral of the square of the lightning current during the lightning discharge period, and the mean steepness parameter expresses the perpendicularity of the lightning current to the front. Damages caused by the induced voltage depend on the facade steepness and for design purposes, an average slope of 30%-90% of the current peak value is used in the average steepness parameter.

Table 2. Lightning current parameters according to protection levels (YILKOMER, 2020)

Lightning parameter	Protection level		
	1	2	3–4
Peak value of current I (kA)	200	150	100
Total electric charge Q_{top} (C)	300	225	150
Pulse electric charge Q_{pulse} (C)	100	75	50
Specific energy W/R (kJ/Ω)	10000	5600	2500
Average steepness $di/dt_{\%30-90}$ (kA/µs)	200	150	100

In the calculations section of the program, the length, width and height of the building and the numerical values determined above for C1, C2, C3, C4, C5 are processed, and the next stage is the formula section. The formulas and definitions defined in the program are given in Table 3.

Table 3. Formulas and definitions

Formulas	Definitions
$Ae=LxW+6xHx (L+W)+9x\pi xH^2$	Effective equivalent area
$Ng=0.04xNk^{1.25}$	Lightning intensity
$Nd=NgxAexC1x10^{-6}$	Expected number of lightning strikes at the facility
$Nk=17.8$	The number of lightning days for the selected province
$C=C2xC3xC4xC5$	Product of the coefficients
$Nc=5.5x10^{-3}/C$	Approved lightning strike count
$E=1-(Nc/Nd)$	Efficiency

The value of N_k in the region to be studied was defined according to the Türkiye Thunderstorm Map given in the program for the average number of lightning days in the formulas section. After this identification, analysis occurred, the efficacy value and protection level were obtained.

Risk Analysis of Natech Accidents Triggered by Flood in Organizations

Pre-hazard list and risk analysis with Fine Kinney were carried out in selected organizations. With the information obtained, first, a preliminary hazard list was prepared to determine the potential hazards and mishaps that may occur. Potentially hazarded elements, subsystems and hazardous situations were used as data in the determination of hazards. The effects of hazards were also considered (Demirdöğen & Çetinyokuş, 2021).

The grading of risks with the Fine-Kinney Method is made by multiplying the numerical values of the probability of occurrence of the risks, the severity of the hazard and frequency of exposure to the hazard. Probability, frequency, severity scales (Table 4) and risk-level table (Table 5) are used for calculating the risk value and classifying the risks. The priority of the measures to be taken is determined according to the risk value determined by the probability, frequency and severity values. When making risk analysis with the Fine-Kinney method, it is critical for the people exposed to risk, the relations of exposure to risk, the possibilities of taking precautions, the continuity of the safety measures and the reliability of the safety measures.

Table 4. *Probability, frequency and severity scales of the Fine-Kinney method (Demirdöğen&Çetinyokuş, 2021)*

POSSIBILITY	
Value	Definition
0.2	Unexpected
0.5	Unexpected but possible
1	Possible but unlikely
3	Possible
6	High/highly possible
10	Definitely expected
FREQUENCY	
Value	Definition
0.5	Very rare (annually or less frequently)
1	Rare (several times a year)
2	Not often (once or several times a month)
3	Occasionally (once or several times a week)
6	Often (once or several times a day)
10	Almost constantly (several times an hour)
SEVERITY	
Value	Definition
1	No near misses, no lost work hours, no first aid required, no environmental damage
3	Minor injury, minor damage, no loss of working days, requires first aid, limited environmental damage
7	Injury, significant damage, outpatient treatment, external first aid, lost working days, low environmental impact
15	Permanent damage, serious injury, long-term treatment, occupational disease, lost work/workday, moderate environmental damage
40	Fatal accident/environmental damage
100	Multiple fatal accidents/environmental disasters

Table 5. *Risk-level values and actions to be taken according to the risk level of Fine-Kinney method (Demirdöğen & Çetinyokuş, 2021)*

Risk Index		Actions to be Taken
Value	The risk category	
R<20	Acceptable Risk	Additional control processes may not be needed to eliminate the identified risks.
20<R<70	Possible Risk	Existing controls should be maintained and audited
70<R<200	Significant Risk	Corrective/preventive actions should be initiated in the long term to reduce the identified risks.
200<R<400	High Risk	For these risks, measures should be taken in the short term and corrective/preventive action should be initiated.
R>400	Very High Risk	Work should not be initiated until the identified risk is reduced to an acceptable level, and if there is an ongoing activity, it should be stopped. If it is impossible to reduce the risk despite the activities carried out, the activity should be blocked.

Damages that may occur in and around the facility because of the flood disaster triggering Natech events in LPG storage and distribution facilities are presented in Table 6.

Table 6. *A qualitative damage scale of flood triggering Natech events for LPG storage and distribution facilities (Krausmann & Musthaq, 2008)*

Flood severity levels	Low	Moderate	High
Wholesale and retail storage and distribution (including LPG, fuel, etc.)	• No stop of operations. • No flood protection measures were implemented. • Warehouse buildings do not have embankments around the warehouses. • No displacement of tanks. • Small cylindrical tanks have a low risk of displacement.	• There is damage to the warehouse buildings. • Dangerous substances are carried by flood waters. • Small storage tanks have buoyancy and displacement. • There is a potential release of hazardous materials at the site. • There is little potential for off-site pollution. • There are fires and explosions in the presence of an ignition source.	• There is severe damage to the warehouse buildings. • Tanks have buoyancy and displacement. • There is damage to the equipment. • There is a potentially large release of toxic substances into the water or air from defective tanks or ruptured pipe connections. • There is potential for serious off-site pollution. • There is a risk of fire and explosion if flammable and/or explosive substances are released in the presence of an ignition source. • There is an increased risk of release, fire and/or explosion due to collisions between tanks and vessels and with debris. • There is a risk of unexpected side reactions due to the wide variety of substances present.

Floods are difficult to control by their nature and large volumes of water can reach industrial facilities by overcoming obstacles and causing negative consequences. Industrial facilities have unique characteristics in terms of production processes and hazardous materials used or produced. As a result, LPG storage and distribution facilities also have certain danger potential and vulnerability in terms of the hazardous materials they use.

3. RESULTS AND DISCUSSION

Statistical studies conducted for risk analysis of technological accidents triggered by natural disasters, and details of risk analysis studies of Natech accidents caused by floods and lightning in selected organizations, over different methodologies, are presented in the following sections.

Statistical Evaluation of Natech Accidents

21 Natech accidents have been detected in the last 15 years. The data obtained from the databases were processed into the SPSS program based on the titles of date, location, natural disaster subgroup, natural disaster type, affected facility and affected equipment type. When the statistics of the data processed in the program were evaluated, it was seen that meteorological disasters were more important than geological disasters with a rate of 57% in terms of natural disaster subgroup. Considering the types of natural disasters that occurred, it was seen that among the meteorological disasters, flood and lightning stood out with a rate of 19.0%, while among the geological disasters, landslides with a rate of 19.0% and tsunami with a rate of 14% came to the fore (Kurt & Çetinyokuş, 2021) (Figure 1).
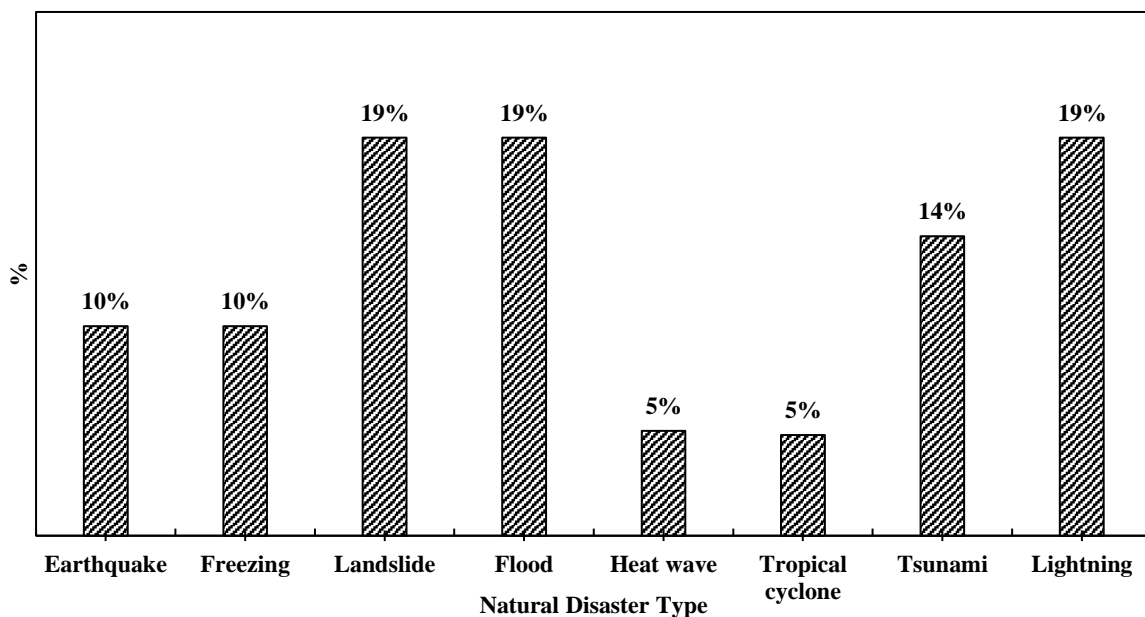
Figure 1. Distribution of types of natural disasters causing Natech accidents

Equipment with loss of containment, which causes technological accidents because of triggering natural disasters, was also evaluated. The distribution of equipment affected in the Natech accidents is presented in Figure 2.

It was seen from Figure 2 that atmospheric storage tanks were the type of equipment that is most affected by the effects of natural disasters and had a loss of containment (19%). This was followed by the pipeline (14%). It was stated in the literature that 85% of Natech accidents in the world were triggered by meteorological disasters and the equipment most affected by this process was storage tanks (Renni et al., 2010; Ricci et al., 2021). Additionally, it was stated that 36% of meteorological disasters caused Natech accidents in the dangerous liquid pipeline system on land (Girgin et al., 2019).
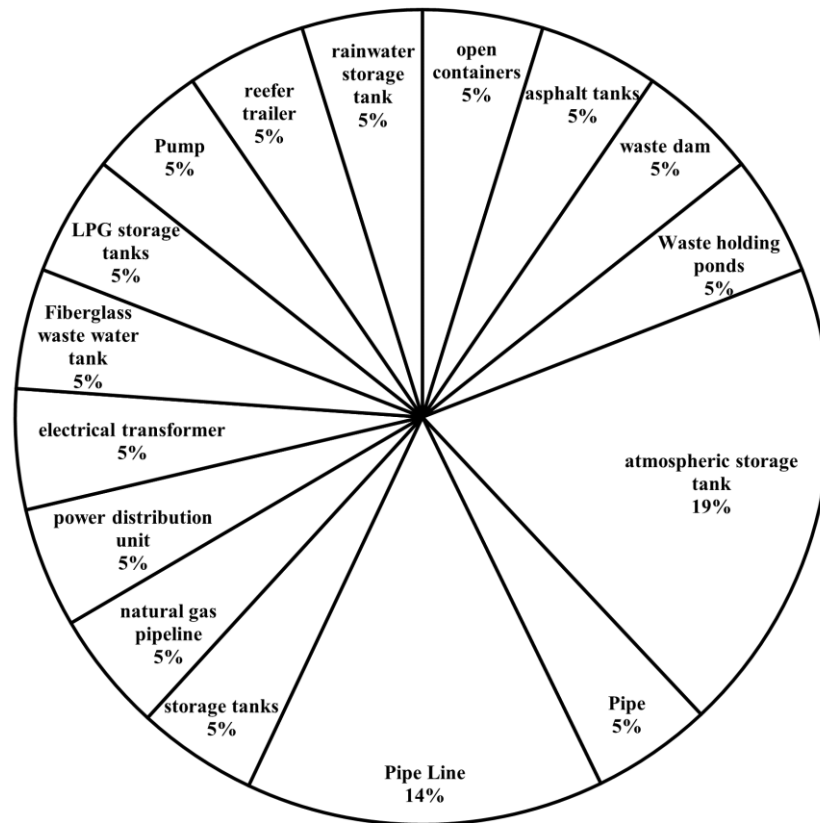
Figure 2. Distribution of equipment affected in Natech accidents

Risk Analysis of Natech Accidents Triggered by Lightning in Organizations

The statistical evaluation showed that natural disaster types such as landslide, flood and lightning stood out in the Natech accidents. For this reason, the intensities of landslides, floods and lightning that occurred in Türkiye were examined on the basis of provinces and it was desired to determine a province containing all the prominent disasters. Considering the Türkiye landslide disaster map and Türkiye flood map, it was determined that Erzurum was among the most risky provinces in terms of landslide and flood intensity. No information could be obtained for lightning, but it was predicted that it would be compatible with flood and landslide data. To conduct the risk analysis study of technological accidents triggered by natural disasters in Erzurum province, sample organizations within the scope of the Regulation were selected in two different locations. The selected organizations carried out gas storage and filling facility operations. They represent high-level organizations within the scope of the relevant regulation. It is also stated in the literature that gas filling and storage facilities are one of the risky facilities most damaged by overvoltage and lightning strikes (Acikgoz, 2012). This makes it important to analyze and evaluate such facilities. Hazardous chemicals in gas filling and storage facilities such as propane, butane and LPG were also considered in the selection of the organizations.

Risk Analysis of Natech Accidents Triggered by Lightning in Organizations

In the literature, it has been stated that jet fire will occur in pressurized storage tanks where flammable materials are stored due to lightning strikes and puncture (Misuri et al., 2020). An analysis of Natech historical accidents also showed that many accidents resulted in jet fires (35%) (Renni et al., 2010). The analyses made on the relevant programs for the sample organizations in Erzurum are presented in two sub-titles.

Organization 1

In Organization 1, there are 5 storage tanks with a volume of 115 m³ with 85% fill rate. Among these, three tanks contained 70% butane-30% propane, one of the remaining two tanks contained 50% butane-50% propane

and the other 100% propane. All the tanks have the same properties, except for the chemical in them, and data on the chemical is not requested in the program. For this reason, it was found to be sufficient to enter the information of any tank into the program. Since the protection system of the organization is the faraday cage, the risk analysis program of the faraday cage obtained from YILKOMER was applied:

- ✓ When the environmental location was examined, the breeding cattle farm was located in the closest and the C1 value was taken as 1 because it was 3h away.
- ✓ The C2 value was determined as 2 by choosing metal and combustible options since the structure was a tank.
- ✓ Because of the presence of flammable and combustible materials in the tanks, the C3 value of the building's fire risk was chosen as 3.
- ✓ The C4 value was chosen as 3 since the building may cause panic and evacuation difficulties on people due to the presence of flammable and combustible materials.
- ✓ The C5 value was taken as 10 because the building contained hazardous materials and may cause fire and explosion because of a lightning strike.

The length and width of the structure were taken from the tank information, the Nk value was specified as 17.8 for Erzurum, then the efficiency value was obtained as 0.882537. According to the efficiency value, the protection level was determined as 3, the cage spacing was 15 m*15 m, and the landing range was 20 m. This includes lightning strikes with a current value of 100 kA. Industrial enterprises and factories in this region carry serious risks. If new structures were built around the organization, attention should be paid to the distance to the relevant facility and the length of the facility, awareness of the employees should be raised on this issue, and periodic controls of the faraday cage, which is a protection system, should be made (Kurt & Çetinyokuş, 2021).

Organization 2

- ✓ In Organization 2, there are spherical tanks with a volume of 3000 m^3 and 4 horizontal cylindrical tanks with a volume of 115 m^3. The spherical tank contains 70% Butane-30% propane and has a 40% fill rate. Three of the horizontal cylindrical tanks store auto gas LPG and one stores commercial propane. Auto gas LPG tanks contain 60% Butane-40% Propane, and two have 50% and one 70% fill rate. The auto gas LPG tank with the highest fill rate (70% fill) was used for the analysis. Since the protection system of the organization is a lightning rod, the risk analysis program of the lightning rod system obtained from RADSAN was applied:
- ✓ C1 value was taken as 0.25 because the organization was among similar structures in terms of environmental location.
- ✓ The C2 value was chosen as 2 by choosing metal and combustible options because the structure was a tank.
- ✓ Because of the presence of flammable materials in the tanks, the C3 value of the building was taken as 3.
- ✓ The C4 value was chosen as 3 since the building may cause panic and evacuation difficulties due to the cramped environment, as well as the fact that the building contained flammable materials.
- ✓ The C5 value was taken as 10 because the building contained hazardous matter and may cause fire and explosion because of a lightning strike.

The length and width of the structure were taken from the tank information and processed, and the Nk value was specified as 17.8 for Erzurum, then the efficiency value was calculated as 0.605682. According to the efficiency value, the protection level was 4 and the radius of the lightning rod protection area was 107 m. In many places in Türkiye, lightning strikes of 100 kA corresponding to this value are frequently experienced, and similar to Organization 1, industrial enterprises and factories in this region carry serious risks. It was stated that for storage tanks of industrial importance, the probability of contingent damage from the impact of lightning strikes is higher than 10^{-2} for atmospheric tanks and at least one-fold lower in the case of pressurized tanks (Necci et al., 2013a). The lightning strike frequency and thus the lightning NaTech risk can be greatly reduced by the use of one (or more) lightning protection masts (Necci et al., 2013b).

The lightning rod, which attracts the lightning with the metal rod attached to its end at the highest point of the buildings and flows the lightning current to the ground, prevents the lightning from falling directly on the buildings and prevents the possible fire risk. However, it does not protect the electrical installations and the devices connected to the electrical installations against overvoltage and overcurrent due to lightning strikes. For this reason, since the lightning rod system alone will not provide high protection, additional measures should be taken to the system such as surge arresters (YILKOMER, 2020). The fact that Organization 2 is located in the organized industrial zone and in a more crowded area and has a larger tank compared to Organization 1 increases the risk of damage. It is necessary to raise awareness of the organization, the surrounding community, and all institutions and organizations that have a possible domino effect in the organized industrial zone (Kurt & Çetinyokuş, 2021).

Risk Analysis of Natech Accidents Triggered by Flood in Organizations

The analyses carried out specific to the determined organizations are presented under two separate headings.

Organization 1

Organization 1 has 3 pump suction pipelines with a diameter of 115 mm, 3 tank liquid pipelines with a diameter of 80 mm, gas phase suction and gas phase discharge pipelines with a diameter of 50 mm. Additionally, the organization has a return mix pipeline with a diameter of 80 mm and 2 return pipelines with a diameter of 50 mm, a tube filling mix with a diameter of 80 mm and a propane pipeline with a tube with a diameter of 50 mm. Pipeline pressures vary between 2.5 and 6.5 bar and its height from the ground is 1 meter. In line with these data, the preliminary hazard list applied specifically to the flood disaster triggering mechanism for Organization 1 is presented in Table 7.

Table 7. *Preliminary hazard list for Organization 1*

#	Source of Hazard	Effects of Hazard	Recommendations
D1	Storage tank	Environmental pollution because of chemicals in tanks mixing with flood waters	Protections against flood water should be constructed. Safety measures should be established before the disaster.
D2		Spontaneous ignition and explosion because of mixing of chemicals in tanks with flood waters	Flood disasters should be included in planning.
D3		Loss of life and property due to fire because of transporting the storage tank with flood waters	Strengthening work should be done for storage tanks. Fixing should be done.
D4		Loss of life and property due to explosion because of transporting the storage tank with flood waters	
D5		Loss of life and property due to fire because of the overturning of the storage tank	Dikes should be built around storage tanks.
D6		Loss of life and property due to explosion due to overturning of storage tank	
D7		Loss of life and property due to toxic spread because of the overturning of the storage tank	
D8	Wastewater tank	Waste overflow because of flood water passing through the wastewater tank enclosures	Waste water tanks must be flooding-resistant .
D9		Disruption of water treatment and disposal systems because of flood waters passing through wastewater tank enclosures, toxic release	In preparation for heavy rain, the wastewater tank level should be kept low and disposed of immediately if possible.
D10		Toxic release because of flood waters passing through the wastewater tank enclosures	

Table 7 *(continued)*

#	Source of Hazard	Effects of Hazard	Recommendations
D11	Electrical connections	Loss of life and property due to fire that may occur because of electric current/spark	The electrical installations should be enclosed by protected mechanisms.
D12		Loss of life and property due to an explosion that may occur because of an electric current/spark	
D13	Connection equipment	Explosions because of leakage that may occur due to possible deformation in connection equipment	Periodic checks of connection equipment such as , valve, safety valve, inlet-outlet line should be made.
D14		Environmental pollution because of leakage that may occur due to possible deformation in connection equipment	
D15	Fuel transfer pump	Environmental pollution because of fuel spillage through the pump due to the gasket failure of the fuel transfer pump.	Periodic maintenance of the pumps should be done. It can be positioned so that it is higher than the flood water level.
D16	Safety barriers	Property damage to the facility due to the failure of the emergency shutdown system in case of flood	Periodic maintenance of safety barriers should be monitored and controlled by running them during exercises.
D17		Loss of life because of the conductivity of the electric current in the flood water due to the failure of the electric current	
D18		Fires due to rupture in pipelines connected to flood waters	Improved barrier should be designed around the piping.
D19	Pipelines	Environmental pollution because of rupture in pipelines connected to flood waters	
D20		Toxic release due to rupture of pipelines due to flood waters	
D21	Lack of disaster training among employees	Loss of life and property because of unconscious actions of employees during floods	Disaster training should be given to the employees in a way that gives priority to the disasters they may be exposed to in terms of their region.
D23	Vehicles and construction machinery	Loss of life of workers in the field due to flood waters dragging vehicles and work machines	A sheltered area away from employees should be determined for the working areas of vehicles and work machines.
D24		Property damage because of flood waters dragging vehicles and construction equipment	
D25	Tanker loading terminal	Damage to the terminal due to the strength of the flood water	Necessary reinforcements should be made at the terminal and material selection can be made according to the danger during the construction phase.
D26	Tanker	Environmental pollution because of overturning of the tanker due to the force of the flood water	Tanks should be fixed in a flood-resistant manner.
D27	Heavy snowmelt in the spring in the facility area	Loss of life and property because of flood waters due to heavy snowmelt transporting unfixed equipment	The equipment should be fixed and the equipment to be used should be selected in accordance with the flood risk.
D28		Damage to equipment such as valves, reactors and sensors by flood waters due to heavy snowmelt	

Table 7 *(continued)*

#	Source of Hazard	Effects of Hazard	Recommendations
D29	Pressure relief valve	Property damage because of failure to control the pressure due to the loss of function of the pressure relief valve because of flood waters	Periodic maintenance of the pressure relief valve should be performed.
D30		Rupture in tanks because of failure to control the pressure due to the loss of function of the pressure relief valve because of flood waters	
D31		Explosion in tanks because of failure to control the pressure due to the loss of function of the pressure relief valve because of flood waters.	
D32	Drainage system	Property damage because of failure to control flood waters due to the drainage system's failure to drain the flood water	A drainage system should be provided for the facility and its controls should be implemented.
D33	LPG contains hydrocarbon compounds	Fire because of deformation in the tank because LPG contains hydrocarbon compounds.	The structure of the tanks should be strengthened to prevent the release of hydrocarbon, which is a flammable substance, from the tanks.
D34		Explosion because of deformation that may occur in the tank because LPG contains hydrocarbon compounds.	

Because of the preliminary hazard list in Organization 1, 34 hazard effects caused by the flood disaster were determined. Multiple hazard effects were obtained for the storage tank, waste water tank, pipeline and pressure relief valve.

For the identified hazard effects, the risk value was obtained by multiplying the probability of occurrence of the risks, the frequency of exposure to the hazard and the numerical values of the effect it creates. Erzurum province becomes prone to floods due to heavy snow melt in the spring months. The facilities are located in the altitude range of 1600–1750 m (HGM, 2022). Considering snowmelt and altitude factors, the frequency of exposure to the hazard was evaluated according to the frequency of the flood disaster. The obtained risk value determines the priority of the measures to be taken. Flooding has direct and indirect consequences in industrial facilities such as buckling, buoyancy up to 30 meters, tipping, hard friction, slippage, displacement, hydraulic pressure, failure of flanges and connections (Olivar, 2018). Fine Kinney evaluation report for Organization 1 is presented in Table 8.

Twenty-two hazard effects were rated in the Fine Kinney method. The main parameters affecting the probability of storage tank failure are water height, water velocity and tank filling level (Landucci et al., 2014). Because of the risk rating, it was observed that there were four significant risks and two high risks in Organization 1. LPG contains hydrocarbon compounds and that electric current becoming more conductive with flood water posed a high risk. Periodic maintenance of safety barriers should be monitored and controlled to reduce the electric current conductivity with flood water. The structure of the tanks should be strengthened to prevent the release of hydrocarbon, which is a flammable substance, from the tanks. Other recommendations for each hazard effects and risk are presented in Table 8.

Table 8. *Fine Kinney evaluation report for Organization 1*

#	Hazard	Risk	Those affected	Possibility	Frequency	Severity	Risk Value	Actions to be Taken
1	Mixing of chemicals into flood water because of a storage tank rupture	Environmental pollution, self-ignition, explosion	Employees, living creatures (plants, animals), third parties	3	1	15	45 Possible Risk	Protections against flood waters should be built. Flood disasters should be included in planning. Safety measures should be established before the disaster.
2	Fire because of transporting the storage tank with flood waters	Loss of life and property	Employees and third parties	1	1	7	7 Acceptable Risk	Strengthening work should be done for storage tanks. Fixing should be done.
3	Explosions because of transporting the storage tank with flood waters	Loss of life and property	Employees and third parties	1	0.5	40	20 Possible Risk	
4	Fire due to overturning of storage tanks	Loss of life and property	Employees and third parties	3	0.5	7	10.5 Acceptable Risk	Dikes should be built around storage tanks.
5	Explosion due to overturning of storage tanks	Loss of life and property	Employees and third parties	3	0.5	15	22.5 Possible Risk	
6	Toxic release from overturning a storage tank	Loss of life and property	Employees, living creatures (plants, animals), third parties	3	0.5	15	22.5 Possible Risk	
7	Flood waters passing through wastewater tank enclosures	Disruption of water treatment and disposal systems, waste overflow, toxic release, skin and eye diseases	Employees, living creatures (plants, animals), third parties	6	1	15	90 Significant Risk	Waste water tanks must be flooding-resistant. In preparation for heavy rain, the wastewater tank level should be kept low and disposed of immediately if possible.
8	Fire due to electric current/spark	Loss of life and property	Employees	6	1	15	90 Significant Risk	The electrical installations should be enclosed by protected mechanisms.

Table 8 (continued)

#	Hazard	Risk	Those affected	Possibility	Frequency	Severity	Risk Value	Actions to be Taken
							Risk Grading	
9	Explosion by electric current/spark	Loss of life and property	Employees and third parties	3	0.5	40	60 Possible Risk	
10	Leakage due to deformation in connecting equipment	Explosion, environmental pollution	Employees, living creatures (plants, animals)	3	0.5	15	22.5 Possible Risk	Periodic checks of connection equipment such as , valve, safety valve, inlet-outlet line should be made.
11	Fuel spillage due to fuel transfer pump seal failure	Environmental pollution	Living creatures (plants, animals)	1	0.5	7	3.5 Acceptable Risk	Periodic maintenance of the pumps should be done. It should be positioned so that it is higher than the flood water level.
12	Failure of the emergency shutdown system in case of flood	Property damage	Employees	1	1	1	1 Acceptable Risk	Periodic maintenance of safety barriers should be monitored and controlled by running them during exercises.
13	Electric current becoming more conductive with flood water	Injury, death	Employees and third parties	6	1	40	240 High Risk	
14	Rupture in pipelines connected to flood waters	Fire, environmental pollution	Employees, living creatures (plants, animals), third parties	3	1	40	120 Significant Risk	Improved barrier should be designed around the piping.
15	Rupture of pipelines because of flood waters	Toxic spread	Employees, living creatures (plants, animals), third parties	3	1	40	120 Significant Risk	
16	Lack of disaster training among employees	Loss of life and property	Employees and third parties	6	1	7	42 Possible Risk	Disaster training should be given to the employees in a way that gives priority to the disasters they may be exposed to in terms of their region.
17	Dragging of vehicles and construction equipment by flood waters	Loss of life and property	Employees	3	0.5	1	1.5 Acceptable Risk	A sheltered area away from employees should be determined for the working areas of vehicles and work machines.

Table 8 *(continued)*

#	Hazard	Risk	Those affected	Possibility	Frequency	Severity	Risk Value	Actions to be Taken
							Risk Grading	
18	Overturning of the tanker due to the force of the flood water	Environmental pollution	Employees, driver	3	0.5	7	10.5 Acceptable Risk	These tanks can be fixed.
19	Carrying unfixed equipment from flood waters due to heavy snow melt	Loss of life and property	Employees and third parties	3	1	7	21 Possible Risk	Equipment should be fixed, equipment to be used should be selected in accordance with the risk of flooding..
20	Loss of function of the pressure relief valve because of flood waters	Property damage, rupture, and explosions in tanks	Employees	1	0.5	15	7.5 Acceptable Risk	Periodic maintenance of the pressure relief valve should be performed.
21	Failure of the drainage system to drain the flood waters	Property damage	Employees	3	0.5	3	4.5 Acceptable Risk	A drainage system should be provided for the facility and its controls should be implemented.
22	LPG contains hydrocarbon compounds	Fire, explosion	Employees and third parties	6	0.5	40	240 High Risk	The structure of the tanks should be strengthened to prevent the release of hydrocarbon, which is a flammable substance, from the tanks.

Organization 2

There are 4 pipelines: a tank filling line with a diameter of 77.9 mm, a tank emptying line, an LPG cylinder filling line and an LPG compressor line with a diameter of 52.5 mm in 2. The pipeline has a pressure of 16 bar. Organization 2, unlike Organization 1, is located within the organized industrial zone. In line with these data, Organization 2 was analyzed specifically for the trigger mechanism of flood disaster, and the preliminary hazard list analysis applied is presented in Table 9.

In Organization 2, 37 hazard effects were determined because of the preliminary hazard list. Multiple hazard effects were obtained for the storage tank, the waste water tank, the pipeline, the organization's location within the organized industrial zone, and the pressure relief valve.

The risks were graded because the organization was located within the organized industrial zone. The Fine Kinney evaluation report for Organization 2 is presented in Table 10.

Table 9. *Preliminary hazard list for Organization 2*

#	Source of Hazard	Effects of Hazard	Recommendations
D1	Storage tank	Environmental pollution because of mixing of chemicals in tanks with flood water	Enclosures should be constructed against flood waters. Flood disasters should be included in planning.
D2		Spontaneous ignition and explosion because of mixing of chemicals in tanks with flood waters	Safety measures should be established before the disaster.
D3		Loss of life and property due to fire because of transporting the storage tank with flood waters	Strengthening work should be done for storage tanks. Fixing should be done.
D4		Loss of life and property due to explosion because of transporting the storage tank with flood waters	
D5		Loss of life and property due to fire because of the overturning of the storage tank	Dikes should be built around storage tanks.
D6		Loss of life and property due to explosion due to overturning of storage tank	
D7		Loss of life and property due to toxic spread because of the overturning of the storage tank	
D8	Wastewater tank	Deterioration of water treatment and disposal systems because of flood waters passing through the wastewater tank enclosures	Waste water tanks must be flooding-resistant .
D9		Waste overflow because of flood water passing through the wastewater tank enclosures	In preparation for heavy rain, the wastewater tank level should be kept low and disposed of immediately if possible.
D10		Toxic release because of flood waters passing through the wastewater tank enclosures	
D11	Electrical connections	Loss of life and property due to fire that may occur because of electric current/spark	The electrical installations should be enclosed by protected mechanisms.
D12		Loss of life and property due to explosion due to electric shock, electric current/spark	
D13	Connection equipment	Explosions because of leakage that may occur due to deformation that may occur in connection equipment.	Periodic checks of connection equipment such as , valve, safety valve, inlet-outlet line should be made.
D14		Environmental pollution because of leakage that may occur due to deformation in connection equipment	
D15	Fuel transfer pump	Environmental pollution because of fuel spillage from the pump due to the gasket failure of the fuel transfer pump.	Periodic maintenance of the pumps should be done. It can be positioned so that it is higher than the flood water level.
D16	Safety barriers	Property damage to the facility due to the failure of the emergency shutdown system in case of flood	Periodic maintenance of safety barriers should be monitored and controlled by running them during exercises.
D17		Loss of life because of the conductivity of the electric current in the flood water due to the failure of the electric current	

Table 9 *(continued)*

#	Source of Hazard	Effects of Hazard	Recommendations
D18	Pipelines	Fires due to rupture in pipelines connected to flood waters	Improved barrier should be designed around the piping.
D19		Environmental pollution because of rupture in pipelines connected to flood waters	
D20		Toxic release because of rupture of pipelines connected to flood waters	
D21	Lack of disaster training among employees	Loss of life and property because of unconscious actions of employees during floods	Disaster training should be given to the employees in a way that gives priority to the disasters they may be exposed to in terms of their region.
D22	Vehicles and construction machinery	Loss of life of workers in the field due to flood waters dragging vehicles and work machines	A sheltered area away from employees should be determined for the working areas of vehicles and work machines.
D23		Property damage because of flood waters dragging vehicles and construction equipment	
D24	Tanker loading terminal	Damage to the terminal due to the strength of the flood water	Necessary reinforcements should be made at the terminal and material selection can be made according to the danger during the construction phase.
D25	The organization is located within the organized industrial zone.	Illness, loss of life because of chemicals carried by flood water	Public awareness should be raised. Safety measures can also be improved. Flood disaster should definitely be considered in emergency plans.
D26		Injury, loss of life and property because of fires and explosions	
D27		Affecting the surrounding structures from possible environmental pollution because of storage tanks rupture	
D28		The domino effect of institutions and organizations around the organization	It should be ensured that institutions and organizations take safety measures against chemicals in the environment. Employees in environmental institutions and organizations should be made aware.
D29	Tanker	Soil and water pollution because of the tanker overturning due to the force of the flood water	Tanks should be fixed in a flood-resistant manner. Dikes should be added around tanks at a certain height and area, impermeable.
D30	Heavy snowmelt in the spring in the facility area	Loss of life and property because of flood waters due to heavy snowmelt transporting unfixed equipment	The equipment should be fixed and the equipment to be used should be selected in accordance with the flood risk.
D31		Damage to equipment such as valves, reactors and sensors by flood waters due to heavy snowmelt	
D32	Pressure relief valve	Property damage because of failure to control the pressure due to the loss of function of the pressure relief valve because of flood waters	Periodic maintenance of the pressure relief valve should be performed.
D33		Rupture in tanks because of failure to control the pressure due to the loss of function of the pressure relief valve because of flood waters	
D34		Explosion in tanks because of failure to control the pressure due to the loss of function of the pressure relief valve because of flood waters.	
D35	Drainage system	Property damage because of failure to control flood waters due to the drainage system's failure to drain the flood water	A drainage system should be provided for the facility and its controls should be implemented.
D36	LPG contains hydrocarbon compounds	Fire because of deformation in the tank because LPG contains hydrocarbon compounds.	The structure of the tanks should be strengthened to prevent the release of hydrocarbon, which is a flammable substance, from the tanks.
D37		Explosion because of deformation that may occur in the tank because LPG contains hydrocarbon compounds.	

Table 10. *Fine Kinney evaluation report for Organization 2*

#	Hazard	Risk	Those affected	Possibility	Frequency	Severity	Risk Value	Actions to be Taken
				Risk Grading				
1	Mixing of chemicals into flood water because of a storage tank rupture	Environmental pollution, spontaneous combustion, explosion	Employees, living creatures (plants, animals), third parties	3	1	15	45 Possible Risk	Protections against flood waters can be constructed. Flood disasters should be included in planning. Safety measures should be established before the disaster.
2	Fire because of transporting the storage tank with flood waters	Loss of life and property	Employees, third parties	1	1	7	7 Acceptable Risk	Strengthening work can be done for storage tanks. Fixing should be done.
3	Explosions because of transporting the storage tank with flood waters	Loss of life and property	Employees, third parties	1	0.5	40	20 Possible Risk	Enclosures should be built around storage tanks.
4	Fire due to overturning of storage tanks	Loss of life and property	Employees, third parties	3	0.5	7	10.5 Acceptable Risk	Bundles and enclosures should be built around the storage tanks so that they are not affected by possible sparks.
5	Explosion due to overturning of storage tanks	Loss of life and property	Employees, third parties	3	0.5	15	22.5 Possible Risk	By taking the storage tank into the pool, it can be ensured that the fire does not spill out from the pool.
6	Toxic release from overturning a storage tank	Loss of life and property	Employees, living creatures (plants, animals), third parties	3	0.5	15	22.5 Possible Risk	The potential toxic spread should be prevented by constructing bunds and enclosures around storage tanks.
7	Flood waters passing through wastewater tank enclosures	Disruption of water treatment and disposal systems, waste overflow, toxic release, skin and eye diseases	Employees, living creatures (plants, animals), third parties	6	1	15	90 Significant Risk	Waste water tanks must be flooding-resistant . In preparation for heavy rain, the wastewater tank level should be kept low and disposed of immediately if possible.
8	Fire due to electric current/spark	Loss of life and property	Employees	6	1	15	90 Significant Risk	Electric installations should be enclosed by sheltered mechanisms.
9	Explosion by electric current/spark	Loss of life and property	Employees, third parties	3	0.5	40	60 Possible Risk	Periodic checks should be made. All electrical panels must have an insulation material in front of them.

Table 10 (continued)

#	Hazard	Risk	Those affected	Possibility	Frequency	Severity	Risk Value	Actions to be Taken
							Risk Grading	
10	Leakage due to deformation in connecting equipment	Explosion, environmental pollution	Employees, living creatures (plants, animals)	3	0.5	15	22.5 Possible Risk	Periodic checks of connection equipment such as , valve, safety valve, inlet-outlet line should be made.
11	Fuel spillage due to fuel transfer pump seal failure	Environmental pollution	Living creatures (plants, animals)	1	0.5	7	3.5 Acceptable Risk	Periodic maintenance of the pumps should be done. It can be positioned so that it is higher than the flood water level.
12	Failure of the emergency shutdown system in case of flood	Property damage	Employees	1	1	1	1 Acceptable Risk	Periodic maintenance of safety barriers should be monitored and controlled by running them during exercises.
13	Electric current becoming more conductive with flood water	Injury, death	Employees, third parties	6	1	40	240 High Risk	To cut off the contact of electricity with the flood water, electricity should be installed inside the covered areas or insulation materials should be used to completely cut the contact of the electricity with the flood water. Personnel must be prevented from entering the electrical risky areas.
14	Rupture in pipelines connected to flood waters	Fire, environmental pollution	Employees, living creatures (plants, animals), third parties	3	1	40	120 Significant Risk	Improved barrier can be designed around the piping.
15	Rupture of pipelines connected to flood waters	Toxic spread	Employees, living creatures (plants, animals), third parties	3	1	40	120 Significant Risk	
16	Lack of disaster training among employees	Loss of life and property	Employees, third parties	6	1	7	42 Possible Risk	Disaster training should be given to the employees in a way that gives priority to the disasters they may be exposed to in terms of their region.
17	Dragging of vehicles and construction equipment by flood waters	Loss of life and property	Employees	3	0.5	1	1.5 Acceptable Risk	A sheltered area away from employees can be determined for the working areas of vehicles and work machines.

Table 10 (continued)

#	Hazard	Risk	Those affected	Risk Grading				Actions to be Taken
				Possibility	Frequency	Severity	Risk Value	
18	Transport of chemicals to the settlement area by flood water	Illness and loss of life	Employees, living creatures (plants, animals), third parties	6	1	100	600 Very High Risk	Enclosures should be built around an organization. Improvements should be made to the drainage systems.
19	The spread of the fire within the organization to the surrounding organizations	Loss of life and property	Employees, third parties	6	1	40	240 High Risk	Environmental awareness should be raised. Necessary precautions for fire and fire response systems should be developed within the organization.
20	The explosion experienced within the organization has effects on the environmental organizations	Loss of life and property	Employees, third parties	6	1	100	600 Very High Risk	Structures should be established around the establishment boundary to eliminate the effects of explosion immediately. The immediate evacuation of personnel and the public in the relevant areas should be ensured.
21	Overturning of the tanker due to the force of the flood water	Environmental pollution	Employees, driver	3	0.5	7	10.5 Acceptable Risk	Tanks should be designed to withstand flood water severity. Strong fixation of the tanks must be ensured.
22	Carrying unfixed equipment from flood waters due to heavy snow melt	Loss of life and property	Employees, third parties	3	1	7	21 Possible Risk	Equipment must be fixed. The equipment to be used should be selected in accordance with the flood risk.
23	Loss of function of the pressure relief valve because of flood waters	Property damage, rupture, and explosions in tanks	Employees	1	0.5	15	7.5 Acceptable Risk	Periodic maintenance of the pressure relief valve should be performed.
24	Failure of the drainage system to drain the flood waters	Property damage	Employees	3	0.5	3	4.5 Acceptable Risk	A drainage system should be provided for the facility and its controls should be implemented. The drainage system should be improved.
25	LPG contains hydrocarbon compounds	Fire, explosion	Employees, third parties	6	0.5	40	240 High Risk	The structure of the tanks can be strengthened to prevent the release of hydrocarbon, which is a flammable substance, from the tanks.

Table 10 (continued)

#	Hazard	Risk	Those affected	Possibility	Frequency	Severity	Risk Value	Actions to be Taken
							Risk Grading	
26	Chemical spillage in the residential area because of the storage tank rupture	Environmental pollution, skin and eye diseases	Living creatures (plants, animals), third parties	3	0.5	15	22.5 Possible Risk	Dikes should be built around the storage tanks, so that the settlement area is not affected or affected with the least damage in case of a possible flood disaster.
27	The people living in the residential area are unconscious and vulnerable to dangers.	Injury, loss of life, property damage	Public	6	1	15	90 Significant Risk	The public should be made aware. Safety measures should be selected according to the residential area.
28	The institutions and organizations around the organization are vulnerable to possible domino effects.	Injury, loss of life, property damage	Employees	6	1	100	600 Very High Risk	It should be ensured that institutions and organizations take safety measures against chemicals in the environment. Employees in environmental institutions and organizations should be made aware.

Twenty eight hazard effects were graded in the Fine Kinney method. Because of the risk rating, it was observed that there were three very high risks and three high risks in Organization 2. It was indicated that the institutions and organizations around the organization are vulnerable to possible domino effects, the explosion experienced within the organization has affects on the environmental organizations and the transport of chemicals to the settlement area by flood water had very high risks. To eliminate the hazard on the transport of chemicals to the settlement area by flood water, enclosures should be built around the organization and improvements should be made to the drainage system. Other recommendations for each hazard effects and risk are presented in Table 10. It can be said that Organization 2 is more risky than Organization 1. Increasing the severity of the flood increases either the water height or the water velocity and increases the vulnerability of the equipment (Caratozzolo et al., 2022). The degree of damage caused by the flood is determined by the characteristics of the flood, the location of the settlement and the characteristics of the population. Building standards, system design, the presence of warning systems, the presence of toxic and reactive substances, structural strength, drainage capacity, and anchoring to the ground are among the factors that affect damage due to flood-triggered Natech accidents (Rota et al., 2008).

4. CONCLUSION

Analysis of past Natech accident data showed that meteorological disasters were more dominant. Therefore, risk management of Natech accidents triggered by meteorological disasters is particularly important. It was determined that Erzurum was among the most risky provinces in terms of landslides (19%) and floods (19) from meteorological disasters. It was assumed that lightning was compatible with flood and landslide data. It was shown that various storage tanks can be affected by Natech accidents, and within the scope of the relevant To conduct Natech risk analysis studies, high-level organizations within the scope of the Regulation containing the relevant equipment were selected. Natech accidents triggered by lightning were analyzed by YILKOMER and RADSAN. The environmental condition, occupancy, structural features, usage parameters of the building as well as the height and width information of the building were processed into the analysis program. Protection

levels were obtained for Organization 1 and Organization 2 as 3 and 4, respectively. Although a similar risk level was determined for the organizations in the analyses carried out, the damage risk of Organization 2 was found to be higher. Natech accidents triggered by the flood were examined with the preliminary hazard list and Fine-Kinney methods. In Organization 2, more hazard effects were determined with both methods, and it was determined that Organization 2 could create possible domino effects on the surrounding structures/buildings. Considering Türkiye's disaster nature, the study will constitute an important resource in the risk analysis of technological accidents triggered by natural disasters and it is foreseen that it will make significant contributions to both legislation and scientific studies.

CONFLICT OF INTEREST

The authors declare no conflicts of interest.

REFERENCES

Acikgoz, V. (2012). Modeling of fire and explosion situations in LPG storage tanks. MSc Thesis, Yildiz Technical University, Institute of Science and Technology, Istanbul, Türkiye.

Caratozzolo, V., Misuri, A., & Cozzani, V. (2022). A generalized equipment vulnerability model for the quantitative risk assessment of horizontal vessels involved in Natech scenarios triggered by floods. *Reliability Engineering and System Safety*, *223*, 108504. doi:10.1016/j.ress.2022.108504

Çetinyokuş, S. (2018). Consequences Modeling of the Akcagaz Accident through Land Use Planning (LUP) Approach. *Iranian Journal of Chemistry and Chemical Engineering-International English Edition*, *37*(4), 253-264. doi:10.30492/ijcce.2018.35109

Demirdöğen, M. M., & Çetinyokuş, S. (2021). Risk Assessment in a Ready-Mixed Concrete Plant Located in an Earthquake Zone. *OHS Academic*, *3*(1), 79-98.

eNatech Database. (2022). (Accessed: 14/12/2022) URL

Girgin, S., & Krausmann, E. (2016). Historical analysis of U.S. onshore hazardous liquid pipeline accidents triggered by natural hazards. *Journal of Loss Prevention in the Process Industries*, *40*, 578-590. doi:10.1016/j.jlp.2016.02.008

Girgin, S., Necci, A & Krausmann, E. (2019). Dealing with cascading multi-hazard risks in national risk assessment: The case of Natech accidents. *International Journal of Disaster Risk Reduction*, *35*, 101072. doi:10.1016/j.ijdrr.2019.101072

Güneş, Y., & Çetinyokuş, S. (2020). The Problem of Land Use Planning (LUP) for Industrial Accidents in Turkey. *Journal of Humanities and Tourism Research, 10*(2), 226-248. doi:10.14230/johut768

HGM, General Directorate of Mapping. (2022). Physical Map of Erzurum City. (Accessed: 22/03/2022) URL

Krausmann , E., & Musthaq, F. (2008). A qualitative Natech damage scale for the impact of floods on selected industrial facilities. *Natural Hazards*, *46*, 179-197. doi:10.1007/s11069-007-9203-5

Kurt, M. M., & Çetinyokuş, S. (2021, December 17-18). *Risk Analysis of Technological Accidents Triggered by Natural Disasters*. In: B. Topuz (Eds.), Proceedings of the 12th International Scientific Research Congress - Science and Engineering (UBAK 2021), (pp. 48-59). Ankara, Turkiye.

Landucci, G., Necci, A., Antonioni, G., Tugnoli, A., & Cozzani, V. (2014). Release of hazardous substances in flood events: damage model for horizontal cylindrical vessels. *Reliability Engineering & System Safety*, *132*, 125-145. doi:10.1016/j.ress.2014.07.016

Misuri, A., Antonioni, G., & Cozzani, V. (2020). Quantitative risk assessment of domino effect in Natech scenarios triggered by lightning. *Journal of Loss Prevention in the Process Industries*, 64, 104095. doi:10.1016/j.jlp.2020.104095

Moreno, V. C., Ricci, F., Sorichetti, R., Misuri, A., & Cozzani, V. (2019). Analysis of Past Accidents Triggered by Natural Events in the Chemical and Process Industry. *Chemical Engineering Transactions*, *74*, 1405-1410. doi:10.3303/CET1974235

Naderpour, M., Rizeei, H. M., Khakzad, N., & Pradhan, B. (2019). Forest fire induced Natech risk assessment: A survey of geospatial technologies. *Reliability Engineering & System Safety*, *191*, 106558. doi:10.1016/j.ress.2019.106558

Necci, A., Antonioni, G., Cozzani, V., Krausmann, E., Borghetti, A., & Nucci, C. A. (2013a). A model for process equipment damage probability assessment due to lightning. *Reliability Engineering & System Safety*, *115*, 91-99. doi:10.1016/j.ress.2013.02.018

Necci, A., Antonioni, G., Cozzani, V., Borghetti, A., & Nucci, C. A. (2013b). Reduction of NaTech Risk Due to Lightning by the Use of Protection Systems. *Chemical Engineering Transactions*, *31*, 763-768. doi:10.3303/CET1331128

Necci, A., Antonioni, G., Bonvicini, S., & Cozzani, V. (2016). Quantitative assessment of risk due to major accidents triggered by lightning. *Reliability Engineering & System Safety*, *154*, 60-72. doi:10.1016/j.ress.2016.05.009

Official Gazette (2019, March 2). Prevention of Major Industrial Accidents and Reduction of Their Effects (*Büyük Endüstriyel Kazaların Önlenmesi ve Etkilerinin Azaltılması Hakkında Yönetmelik*). Official Gazette of the Republic of Turkey, 30702. URL

Olivar, O. J. R. (2018). Fragility Assessment Methodology of Storage Tanks in NaTech Events. MSC Thesis, Universidad de los Andes Faculty of Engineering, Department of Chemical Engineering, Bogotá, Colombia.

RADSAN. (2021). Radsan Risk Analysis Lightning Rod. (Accessed: 14/12/2022) URL

Renni, E., Krausmann, E., & Cozzani, V. (2010). Industrial accidents triggered by lightning. *Journal of Hazardous Materials*, *184*(1-3), 42-48. doi:10.1016/j.jhazmat.2010.07.118

Ricci, F., Moreno, V. C., & Cozzani, V. (2020). Analysis of NaTech Accidents Triggered by Extreme Temperatures in the Chemical and Process Industry. *Chemical Engineering Transactions*, *82*, 79-84. doi:10.3303/CET2082014

Ricci, F., Moreno, V. C., & Cozzani, V. (2021). A comprehensive analysis of the occurrence of Natech events in the process industry. *Process Safety and Environmental Protection*, *147*, 703-713. doi:10.1016/j.psep.2020.12.031

Rota, R., Caragliano, S., Brambilla, S., & Manca, D. (2008, May 18-23). *Comparing floods and industrial accidents: A conceptual framework for multi-risk assessmen*t. In: Proceedings of PSAM-9 International Conference on Probabilistic Safety Assessment and Management, (pp. 1668-1675), Hong Kong, China.

Wang, J., & Weng, W. (2021). A simplified methodology for rapidly analyzing the effect of multi-hazard scenario on atmospheric storage tanks. *Research Square*. Preprint. doi:10.21203/rs.3.rs-1119680/v1

YILKOMER. (2020). Lightning Protection Regulation (Accessed: 14/12/2022) URL

YILKOMER. (2022). Lightning Protection Levels (Accessed: 14/12/2022) URL

A Study on the Wide Frequency Range Electrical Variables in the Al/Coumarin–PVA/p-Si Diodes at Room Temperature

Selçuk DEMİREZEN[1*]

[1]*Sabuncuoğlu Şerefeddin Vocational School of Health Services, Amasya University, Amasya, Türkiye*

Keywords	Abstract
Coumarin-PVA Interlayer Surface States Frequency and Voltage Dependency Series Resistance	Coumarin-PVA is deposited onto p-Si wafers using the spin coating technique. I examined the fundamental electrical variables of the Al/Coumarin–PVA/p-Si type Schottky barrier diodes (SBDs), by utilizing capacitance/voltage(C-V) and conductance/voltage (G-V) measurements at different frequencies varied from 10kHz to1MHz. I have thoroughly explored how the Coumarin–PVA interlayer, series resistance (R_s) and surface states (N_{ss}) affect the electrical properties of SBDs. In order to remove R_s's influence on the observed C and G values, I corrected them. The observed high values of C/G measured at low frequencies result from the existence of interfacial states. There is evidence that while N_A decreases exponentially with increasing frequency, Φ_B increases exponentially. A particular distribution of N_{ss} density, polarization processes, and the existence of an interfacial layer can all contribute to explaining these characteristic features of them. According to experimental findings, I conclude that the interfacial polymer Coumarin–PVA layer as well as the N_{ss} and R_s also have a significant impact on the C/G-V quantities of SBDs.

1. INTRODUCTION

The search for high-performance electronic and optoelectronic devices has been evolving at an incredible pace thanks to new materials, architectures, manufacturing tools and processes. Advances in electronic systems aim at high density, high speed as well as reduced power dissipation. Due to their basis in electrical systems and ongoing importance in technology, much research has focus on semiconductors. Schottky barrier diodes (SBDs),known as metal/semiconductor (MS) contacts, offer several outstanding characteristics including very quick reaction time and low forward bias. The device becomes a metal/(metal-doped polymer)/semiconductor (MPS) SBD when there is a thin interfacial polymer film placed at the metal/semiconductor(M/S) interface. This interface layer can cause a biased interface state charge due to an extra electric field and affect the electrical properties of the diode (Sze, 1981; Sharma & Tripathi, 2013; Demirezen et al., 2022). Due to their use in the high-speed electrical, optoelectronic, and microelectronic industries, these diodes have surpassed metal/semiconductor (MS) type SBDs in importance. As a result, these gadgets' functionality is crucial. Therefore, current studies in this field have focused on device performance improvement with the use of interfacial layer/layers and complex preparation methods (Sharma & Tripathi, 2013).

As an interfacial polymer layer made of polyaniline, Poly (3-Substituted thiophene), polyvinyl-pyrrolidone, polyethylene-oxide, and polyvinyl alcohol (PVA) have attracted great interest from chemists, physicists and electrical engineers. Among these polymers, polyvinyl alcohol (PVA) has received a lot of interest due to its unique electrical and optoelectronic applications such as low cost, more charge-storage capacity, low molecular weight, nontoxicity, good film formation capacity, flexibility and ease of production process in

comparison with the other materials. Thus, it is widely exercised in fibber technology, paper, weaving, thin film plating and contact lens (Ashery et al., 2021).

Coumarin and its derivatives have become the focus of chemistry, physics, biology and medical research interest. This is because they exhibit numerous appealing features such as fluorescence in the electromagnetic spectrum's visible zone, high quantum yields and high solubility (Wang et al., 2005; Liu et al., 2012). Coumarin and their derivatives are also commonly utilized in sensors (Wang et al., 2005), dye lasers, organic light-emitting diodes (LEDs) (Liu et al., 2012), fluorescent markers, solar energy collectors, dye-sensitized solar cells (DSCs), and nonlinear optical applications (Ghouili et al., 2014).

In our earlier study (Demirezen & Altındal Yerişkin, 2020), we formed Al/p–Si (MS) structures with different Coumarin-PVA interlayer ratios (5, 10 and 20%) and compared their photovoltaic and electrical properties. We concluded that the %5 coumarin−PVA interlayer performed well in terms of higher RR and shunt resistance (R_{sh}) values as well as lower N_{ss} and R_s. In this sense, the main premise of this current study is to seek for more information on the capacitance/conductance-voltage characteristics for Al/(%5wt coumarin−PVA)/p-Si structures across in a wide range of frequency (10kHz-1MHz) and voltage (±5V by 0.05V steps).

2. MATERIAL AND METHOD

In this research, I constructed Al/(Coumarin−PVA)/p-Si structure onto the p-Si (Boron-doped) wafer. To achieve this, firstly, Al back contact was coated backside of the wafer in a vacuum environment (10^{-6} Torr) after that was annealed at 500°C to get lower-resistivity or better ohmic contact. Secondly, stirred (%5wt coumarin−PVA) solution was covered for 30 seconds at 2000 rpm and 80 °C by using the Fytronix spin-coater system. After all, high-purity Al rectifier contacts with 0.785 mm^2 area were formed onto the interfacial layer. More information on the manufacturing procedures of these structures can be available in our former study (Demirezen & Altındal Yerişkin, 2020).

3. RESULTS AND DISCUSSION

In this study, I examined how the Coumarin−PVA interlayer, series resistance (Rs) and surface states (Nss) affect the electrical properties of SBDs. Based on the findings, Figure 1 displays The C-V and G-V curves of the Al/(Coumarin−PVA)/p-Si SBD at ambient temperature. As evident in these figs, both the frequency and voltage are more effective on the C/G variables. While the C and G exhibit significant dispersion in both the accumulation and depletion zones, they exhibit virtually complete frequency independent in the inversion region. In addition, C-V curves clearly show two peaks (weak and strong) that are located in the inversion and accumulation regions, respectively. The first peak (weak peak) can be attributed to a particular dispersion of N_{ss} at the interface and dipole or surface polarization, particularly at lower frequencies. The second peak (strong peak) can be ascribed to the R_s and interface layer. Additionally, in the meantime, peak positions show differences because of the rearrangement of the N_{ss} with direct current(dc) electric field, shifting towards the accumulation zone. On the other hand, the magnitude of these peaks decreases with increasing frequency. This results from the N_{ss} which cannot comply with the applied alternating field and does not supply an extra capacitance (C_{ex}) and conductance (G_{ex}/ω) (Card & Rhoderick, 1971; Nicollian & Brews, 1982).

In order to see the frequency dependency of capacitance and conductance more clearly, C and G data versus frequency were plotted between -1V and 4V by 0.5V steps. Figures 2a and 2b show frequency-dependent C and G/ω plots. As shown in these graphs, the C and G/ω values diminish with increasing frequency because the surface states comply with the applied alternating field at lower frequencies, therefore supplying an excess capacitance.
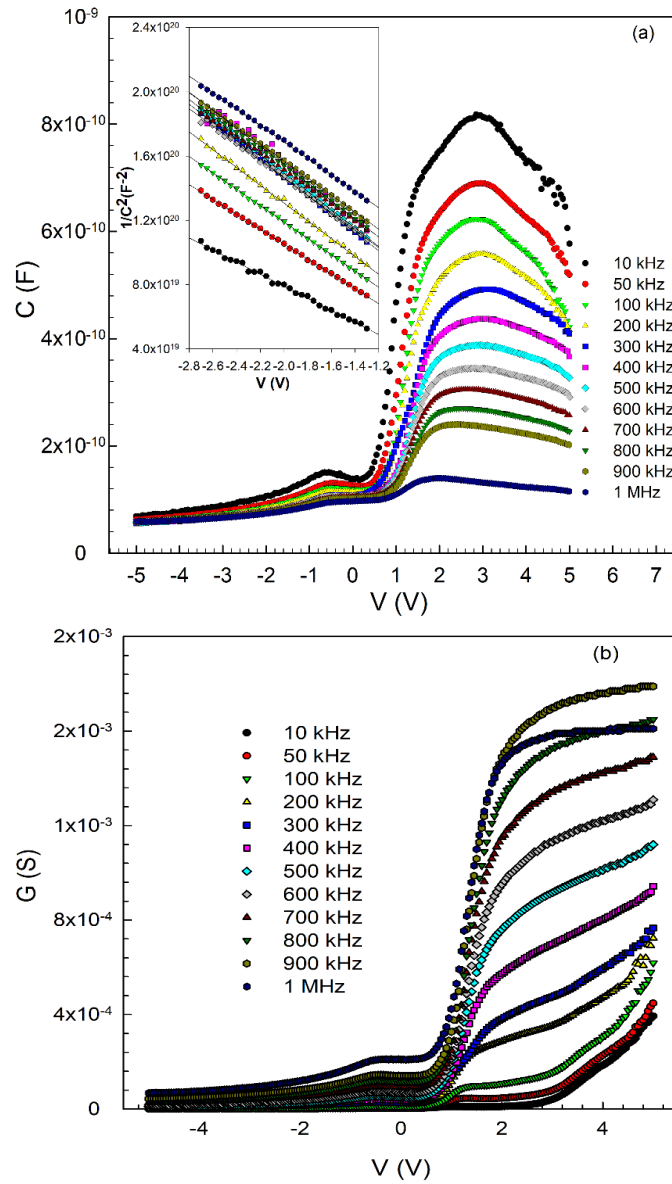
Figure 1. The applied bias voltage dependent a) C-V, b) G-V curves of the Al/Coumarin−PVA/p-Si SBD
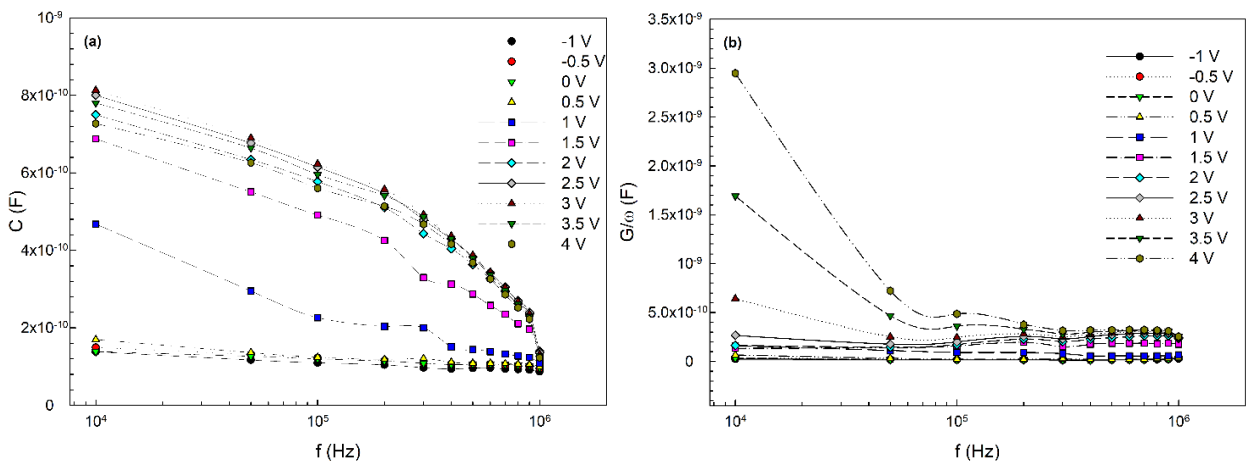

Figure 2. a) Capacitance-frequency and
b) Conductance-frequency plots of the Al/(Coumarin−PVA)/p-Si SBD

As mentioned above, R_s can have a significant impact on the C and G measurements, particularly at high frequencies in the accumulation zone/regime. The most popular technique for avoiding this inaccuracy is to measure R_s and then use it to alter the values of measured Cm and Gm/ω in a strong accumulation zone. As developed by Nicollian and Brews (1982), the subsequent equation may also be used to extract the voltage-dependent resistance (R_i) of the MIS type:

$$R_i = \frac{G_m}{G_m^2 + \left(\omega C_m\right)^2}$$
(1)

Using this approach, the R_s matches to the real R_i, particularly in the accumulation zone and above 500 kHz frequency. The angular frequency is denoted in this equation ω (=2πf), and the C and G are represented by C_m and G_m/ω in the strong accumulation zone. Thus, applied bias voltage and frequency-dependent R_s values were calculated and depicted in Figures 3a and 3b, respectively.
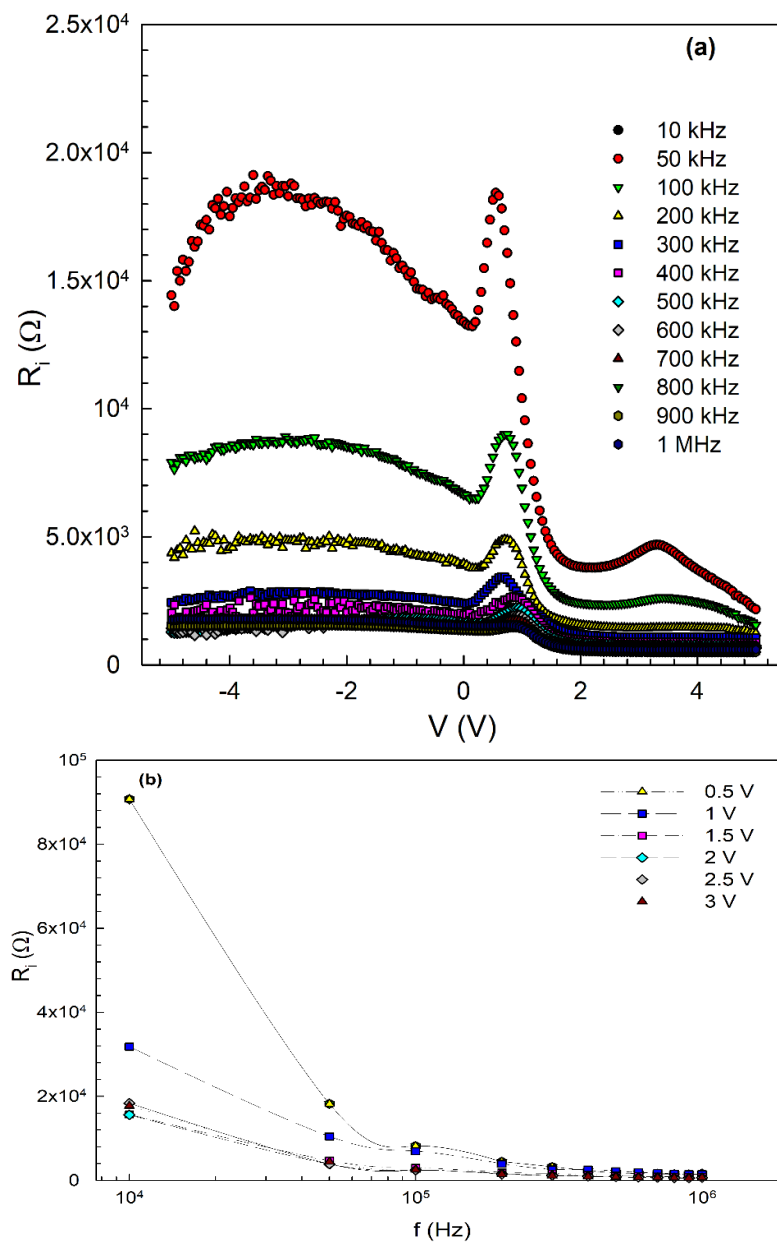

Figure 3. *The experimental R_i-V curves **a)** applied bias voltage dependency,*
***b)** frequency dependency of the Al/(Coumarin−PVA)/p-Si SBD*

Figures 3a and 3b shows that both in the depletion and accumulation zones the R_s value decreases as the frequency increases. Further, as shown in Figure 3a, the R_i curves exhibit a distinct peak and its magnitude decreases with increasing frequency and peaks tend to move in the direction of the accumulation zone as a result of the reorganization and reconstructing of N_{ss} under an electric field. This is due to the frequency and relaxation time (τ) of surface states, electronic charges in these states/traps can comply with an external ac signal at weak frequencies. Therefore, interfacial dipoles have less time at high frequencies to get into a position parallel to the alternative electrical field (Sze, 1981). For each applied bias voltage, R_i values decrease as frequency increases, as shown in Figure 3a and reach a constant value at the high forward bias (powerful accumulation zone). Therefore, the real R_s values correspond to accumulation at 5 V and are given at Table 1. Equation 1 can be used to correct C_m and G_m values by considered the value of R_s in order to avoid Rs effects on the real values of them.

$$C_c = \frac{\left[G_m^2 + (\omega C_m)^2\right]C_m}{a^2 + (\omega C_m)^2} \tag{2a}$$

$$G_c = \frac{G_m^2 + (\omega C_m)^2\, a}{a^2 + (\omega C_m)^2} \tag{2b}$$

where a's value is supplied in the following form (Nicollian & Brews, 1982).

$$a = C_m - \left[G_m^2 + (\omega C_m)^2\right]R_s \tag{2c}$$

There is evidence to suggest that the R_s is the most critical factor responsible for the non-ideal electrical properties of SBDs. With a view to get the correct diode capacitance (C_c) and conductance (G_c), the C_m and G_m values were obtained by considering R_s influence by using Equation 2 and given in Figures 4a and 4b for 1 MHz. As can be seen in Figure 4a, the corrected C value increase as the bias voltage increases especially at the accumulation zone for the elimination Rs effect. I conclude that R_s can influence C and G measurements in depletion and accumulation zones at high frequencies, and therefore, this must be considered while calculating the electric and dielectric characteristics.

The straight-line part of C^{-2}-V graphs (inset Figure 1a) with different frequencies give important electrical characteristics of SBD, such as Φ_B, diffusion potential (V_D), Fermi energy level (E_F), depletion layer width (W_D) and concentration of acceptor atom (N_A). The C^{-2}-V curves display well linear behavior and are extrapolated to the voltage axis to determine the V_D values (Sze, 1981). One way to express the SBD depletion layer width is as follows:

$$W_D = \sqrt{\frac{2\varepsilon_s V_D}{q N_A}} \tag{3}$$

The N_A values may be computable via C^{-2}-V plot's slope for all frequencies. Hence, the E_F and N_A quantities were determined at various frequencies via following relations (Sze, 1981):

$$V_0 = V_D - \frac{kT}{q} \tag{4}$$

and E_F may be given as:

$$E_F = \frac{kT}{q}\ln(\frac{N_V}{N_A}) \tag{5}$$

with

$$N_V = 4.82x10^{15}T^{3/2}\left[\frac{m_h^*}{m_0}\right]^{3/2} \tag{6}$$

where N_V is the effective density state in the Si valance band, $m_h^* = 0.16m_0$ is the effective mass for holes (Sze, 1981), and m_0 (9.1x10^{-31} kg) is the electron's rest mass.
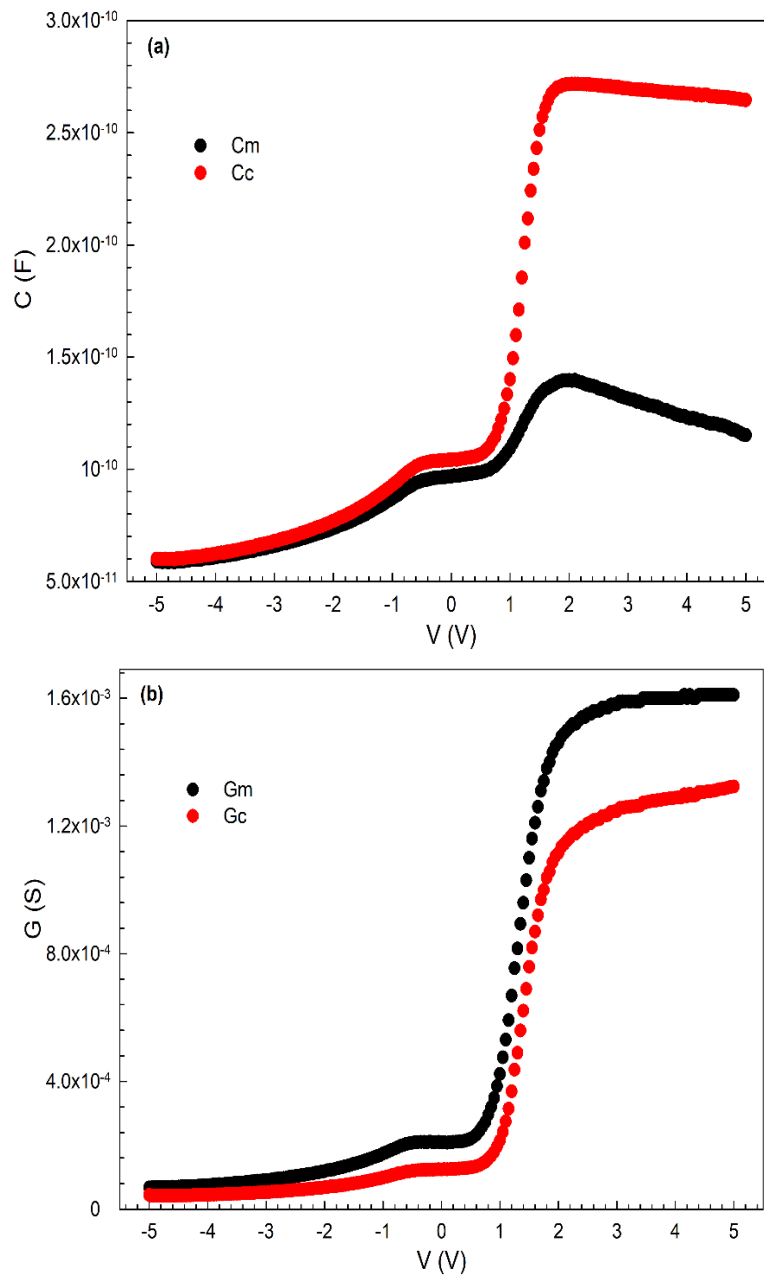

Figure 4. *Voltage dependent **a)** C_c and **b)** G_c/ω curves (without R_s) of the Al/(Coumarin–PVA)/p-Si SBD*

$$N_A = \frac{2}{q\varepsilon_s A^2 \tan(\theta)} \tag{7}$$

Here, ε_s is the permittivity of the Si. As a result, the following relation may be utilized to determine the Φ_B values for each frequency:

$$\Phi_B(C-V) = V_D + E_F \tag{8}$$

Table 1 lists the obtained V_D, N_A, E_F, W_D and $\Phi_B(C\text{-}V)$ parameters for each frequency. This kind of N_A and $\Phi_B(C\text{-}V)$ behavior is predicted and is ascribed to the specific density dispersion of N_{ss} and the interfacial layer (Çokduygulular et al., 2020; Cetinkaya et al., 2022).

Table 1. The frequency dependent some electric quantities of the Al/(Coumarin−PVA)/p-Si SBD

f (kHz)	N_A (cm^{-3})	V_D (eV)	E_F (eV)	W_D (cm)	Φ_B (eV)	Rs (Ω)	Nss (eV^{-1}cm^{-2})
10	5.13×10^{15}	0.21	0.15	2.28×10^{-5}	0.32	2541.78	7.73×10^{13}
50	4.25×10^{15}	0.31	0.15	3.09×10^{-5}	0.41	2163.57	1.76×10^{13}
100	4.12×10^{15}	0.45	0.15	3.77×10^{-5}	0.54	1545.69	1.22×10^{13}
200	4.02×10^{15}	0.58	0.16	4.33×10^{-5}	0.67	1223.62	7.11×10^{12}
300	3.99×10^{15}	0.69	0.16	4.72×10^{-5}	0.78	1041.29	5.02×10^{12}
400	3.96×10^{15}	0.74	0.16	4.90×10^{-5}	0.82	856.48	4.64×10^{12}
500	3.95×10^{15}	0.82	0.16	5.17×10^{-5}	0.91	737.99	4.41×10^{12}
600	3.93×10^{15}	0.84	0.16	5.26×10^{-5}	0.93	649.72	4.30×10^{12}
700	3.69×10^{15}	0.87	0.16	5.51×10^{-5}	0.95	586.98	4.19×10^{12}
800	3.68×10^{15}	0.90	0.16	5.64×10^{-5}	0.99	541.46	4.06×10^{12}
900	3.57×10^{15}	0.97	0.16	5.94×10^{-5}	1.05	507.04	3.92×10^{12}
1000	3.56×10^{15}	1.02	0.16	6.08×10^{-5}	1.10	591.28	3.17×10^{12}

In this work, the Hill-Coleman approach was also employed to obtain the Nss for each frequency and are also tabulate in Table 1 (Hill & Coleman, 1980):

$$N_{SS} = \frac{2}{qA} \frac{(G/\omega)_m}{\left\{ [(G/\omega)_m / C_i]^2 + (1 - C_m/C_i)^2 \right\}} \tag{9}$$

where the contact area represented by A, angular frequency represented by $\omega = 2\pi f$, capacitance and conductance represented by C_m and G_m/ω that in line with the peak values, respectively. Interfacial layer capacitance (C_i) calculated from the strong accumulation zone as (Hill & Coleman, 1980):

$$C_i = C_m \left[1 + \frac{G_m^2}{(\omega C_m)^2} \right] = \frac{\varepsilon_i \varepsilon_o A}{d} \tag{10}$$

Table 1 shows the R_s (at 5 V) and N_{ss} (V) which are corresponding to the peak value of C-V plots as functions of frequency by using Equations 1 and 9, respectively. As indicated in the table, the values of N_{ss} and R_s decrease as frequency increases. This R_s behavior is caused by the interfacial layer and a special dispersion of interface states densities among organic and inorganic semiconductor interfaces (Sze, 1981). Based on these findings, I conclude that both the R_s and N_{ss} values represent greater efficacy on C-V and G-V measurements and have the potential to affect calculations significantly.

4. CONCLUSION

The C-G/ω-V measurements of the Al/(Coumarin-PVA)/p-Si SBD were implemented at ambient temperature in the frequency 1 kHz- 1 MHz range. All of these measurements were performed between (-5V) and (+5V) by 0.05V increment. The effect of Coumarin–PVA interlayer, R_s and N_{ss} on electrical characteristics of the SBD have been investigated in detail. R_s-V plots which acquired using the C and G values displayed a peak behavior at each frequency. These peak magnitudes decrease as the frequency increase in the depletion zone. The observed C and G values were corrected as C_c and G_c by considering Rs for 1MHz. Moreover, the observed lower C and G values at lower frequencies were ascribed to the existence of N_{ss} and polarization processes. While the $\Phi_B(C$-$V)$ values exponentially increase with increasing frequency the N_A value decreases. This predicted propensity of N_A and $\Phi_B(C$-$V)$ is explained by a special density distribution of N_{ss} between p-Si and organic interfacial layer, dipole and surface polarization. The acquired experimental results provide evidence to suggest that the Coumarin–PVA layer has a significant effect on the C-V and G-V measurements of SBDs, as well as R_s and N_{ss}.

ACKNOWLEDGEMENT

REFERENCES

Ashery, A., Gad, S. A., & Turky, G. M. (2021). Analysis of Electrical and Capacitance–Voltage of PVA/nSi. *Journal of Electronic Materials*, *50*(6), 3498-3516. doi:10.1007/s11664-021-08867-y

Card, H. C., & Rhoderick, E. H. (1971). Studies of tunnel MOS diodes I. Interface effects in silicon Schottky diodes. *Journal of Physics D: Applied Physics*, *4*(10), 1589-1601. doi:10.1088/0022-3727/4/10/319

Cetinkaya, H. G., Cicek, O., Altindal, S., Badali, Y., & Demirezen, S. (2022). Vertical CdTe:PVP/ p -Si-Based Temperature Sensor by Using Aluminum Anode Schottky Contact. *IEEE Sensors Journal*, *22*(23), 22391-22397. doi:10.1109/JSEN.2022.3212867

Çokduygulular, E., Çetinkaya, Ç., Yalçın, Y., & Kınacı, B. (2020). A comprehensive study on Cu-doped ZnO (CZO) interlayered MOS structure. *Journal of Materials Science: Materials in Electronics*, *31*(16), 13646-13656. doi:10.1007/s10854-020-03922-6

Demirezen, S., Çetinkaya, H. G., & Altındal, Ş. (2022). Doping rate, Interface states and Polarization Effects on Dielectric Properties, Electric Modulus, and AC Conductivity in PCBM/NiO:ZnO/p-Si Structures in Wide Frequency Range. *Silicon*, *14*(14), 8517-8527. doi:10.1007/s12633-021-01640-0

Demirezen, S., & Altındal Yerişkin, S. (2020). A detailed comparative study on electrical and photovoltaic characteristics of Al/p-Si photodiodes with coumarin-doped PVA interfacial layer: the effect of doping concentration. *Polymer Bulletin*, *77*(1), 49-71. doi:10.1007/s00289-019-02704-3

Ghouili, A., Dusek, M., Petricek, V., Ayed, T. B., & Hassen, R. B. (2014). Synthesis, crystal structure and spectral characteristics of highly fluorescent chalcone-based coumarin in solution and in polymer matrix. *Journal of Physics and Chemistry of Solids*, *75*(2), 188-193. doi:10.1016/j.jpcs.2013.09.011

Hill, W. A., & Coleman, C. C. (1980). A single-frequency approximation for interface-state density determination. *Solid-State Electronics*, *23*(9), 987-993. doi:10.1016/0038-1101(80)90064-7

Liu, X., Cole, J. M., Waddell, P. G., Lin, T.-C., Radia, J., & Zeidler, A. (2012). Molecular Origins of Optoelectronic Properties in Coumarin Dyes: Toward Designer Solar Cell and Laser Applications. *The Journal of Physical Chemistry A*, *116*(1), 727-737. doi:10.1021/jp209925y

Nicollian, E. H., & Brews, J. R. (1982). *Metal oxide semiconductor (MOS) physics and technology*. Wiley.

Sharma, M., & Tripathi, S. K. (2013). Analysis of interface states and series resistance for Al/PVA: N-CdS nanocomposite metal-semiconductor and metal-insulator-semiconductor diode structures. *Applied Physics A: Materials Science & Processing*, *113*(2), 491-499. doi:10.1007/s00339-013-7552-3

Sze, S. M. (1981). *Physics of Semiconductor Devices* (2nd Ed.). Wiley.

Wang, Z.-S., Hara, K., Dan-oh, Y., Kasada, C., Shinpo, A., Suga, S., Arakawa, H., & Sugihara, H. (2005). Photophysical and (Photo)electrochemical Properties of a Coumarin Dye. *The Journal of Physical Chemistry B*, *109*(9), 3907-3914. doi:10.1021/jp044851v

A Comparison Electronic Specifications of the MS & MPS type Schottky Diodes (SDs) via Utilizing Voltage-Current (V-I) Characteristics

Çiğdem Şükriye GÜÇLÜ[1]* iD

[1]Department of Physics, Faculty of Science, Gazi University, 06500, Ankara-Türkiye

Keywords	Abstract
(TeO$_2$:Cu-doped PVP) Interlayer On Performance MS, MPS Type SDs Difference Between Calculation Methods Density of Surface States	The effects of the application of the (TeO$_2$:Cu-PVP) interface to the Al/p-Si (MS) type SD on the performance of the new Al/(TeO$_2$:Cu doped PVP)/p-Si (MPS) SD were reviewed using forward and reverse bias V-I measurements. The thermionic emission (TE) and Cheung & Cheung functions were employed to ascertain the influences of an additional organic interfacial layer on the comparative outcomes of this research. Thus, some essential electrical attributes such as saturation current (I_s), ideality factor (n), rectification-ratio (R.R.=$I_{forward/Ireverse}$), barrier height B.H. (Φ_{bo}), and series/shunt resistances (R_s/R_{sh}) were computed. Furthermore, the density of surface states (N_{ss}) was acquired from the V-I plots according to the Card & Rhoderick method. The observed experimental results indicated that the (TeO$_2$:Cu-PVP) inter-layer enhanced the quality of MS type SD as respects obtained low reverse current, N_{ss}, R_s, and high R_{sh} and R.R. values. All these results indicate that (TeO$_2$:Cu-PVP) inter-layer can be used successfully instead of conventional insulators for its favored specifications like easy fabrication processes, low cost, and flexibility features.

1. INTRODUCTION

Metal/semiconductor (MS) structures are critical emphasis in semiconductor technology. The interfacial layer added between the metal and the semiconductor changes the performance of the structure. When native or deposited inter-layer is performed between metal and semiconductor, MS type SD transforms to metal/inter-layer/semiconductor (MIS) type SDs. The functioning or quality of these structures is dependent on various parameters or factors like surface preparation, the nature of B.H. and inter-layer located M/S interface, their homogeneity, the concentration of donor/acceptor atoms, the existence of N_{ss}/ D_{it}, R_s and R_{sh}, and fabrication processes (Sze, 1981; Sharma, 1984; Rhoderick & Williams, 1988; Reddy et al., 2017; Tanrıkulu et al., 2017). Although conventional SiO$_2$ is stable and abundant since it cannot passivate all unwanted surface states or dislocations, the leakage current and surface states are very high (Sze, 1981; Sharma, 1984; Rhoderick & Williams, 1988; Reddy et al., 2017). Therefore, in recent years, many researchers have started to use an organic/polymer interlayer instead of conventional SnO$_2$ or SiO$_2$ grown by a traditional method like thermal and wed-oxidation.

Organics/polymers are popular in semiconductor-based device technology with some outstanding advantages over insulators. Some of these prominent advantages can be listed as the easy grown process on the surface, low weight/cost/energy consumption, elasticity, high dynamic durability, ability to dissolve in water, and good charge-storage capacity (Altındal et al., 2019; Tataroğlu et al., 2020; Barkhordari et al., 2021). Among polymer materials, polyvinyl-pyrrolidone (PVP) has a semi-crystalline, high water-solubility, nontoxic-polymer, wide

range of crystallinity, high dielectric strength, good charge storage capacity, interesting physical properties which arise from OH groups and formation of hydrogen bonding.

Known as a nonlinear optical material, TeO_2 is widely preferred in optical device technology as tunable filters, deflectors, and modulators (Bindra et al., 2001). It is believed that an extra added thin organic layer with high-dielectric) grown between metal and the semiconductor will increase the efficiency and quality of the designed device. Various basic techniques such as electro-spinning (Altındal et al., 2019), simple reactive thermal-evaporation, sol-gel (Coste et al., 2007), melt quenching (Shivachev et al., 2009), and ultrasound-assisted (Suslick & Doktycz, 1990) are used to create an organic interface with high dielectric permittivity. Due to its apparent advantages in the literature, the ultrasound-assisted method was used within this study to form the tellurium dioxide (TeO_2)-Cu doped PVP organic interface that has grown at M/S interface.

The main purpose of this study is to fabricate Al/p-Si (MS) and Al/(TeO_2:Cu-PVP)/p-Si (MPS) SDs on the same p-Si wafer to determine this organic interlayer effects on the SD by utilizing the V-I measurements in wide range of voltage (±5V). For this aim, the basic electrical parameters of them were extracted from these data and compered each other. In addition, the values of Nss as a function of energy were also extracted from the V-I data, regarding the ideality factor and the voltage dependence of BH. Experimental results show that there was a step-up in R.R. and Rsh values and a lessening in leakage-current, Rs, and Nss values. These results were attributed to the used organic (TeO_2:Cu-PVP) thin film as an interfacial layer at the inter-surfaces of the SD (Card & Rhoderick, 1971; Çetinkaya et al., 2021; Demirezen et al., 2022; Ulusoy et al., 2023).

2. MATERIAL AND METHOD

Both the type-1 and the type-2 SDs were chemically grown on the selfsame p-Si substrate at identical status. Two same-quarter Boron-doped (p-Si) substrates were cleaned in the ultrasonic bath by using standard RCA method (5 units deionize-water (H_2O), 1unit ammonium hydroxide (27% NH4OH), 1 unit hydrogen peroxide (30% H_2O_2) for 15 minutes, rinsed in deionize-water for prolonged time, and dried up with a high percentage of purity level dry nitrogen gas (N_2). Secondly, high-pure Al (99.99%) was thermally evaporated onto the entire rear of two p-Si substrates at 10^{-6} Torr and then annealed in the nitrogen-ambient at 450°C to get satisfactory ohmic contact. Copper acetate-dehydrates ($Cu(CH_3COO)_2$) sodium-telluride/hydroxide (Na_2TeO_3, NaOH) was purchased from the Rankem, Lobachemi, and Merck Company, respectively, and they used for the preparation of the (TeO_2:Cu) nanostructures. After that 0.2 M of the solution of cooper acetate, 0.2 M of Na_2TeO_3 solution, and 2 M NaOH solution were prepared by using deionize-water. The performed cationic and anionic solutions were added together and kept under exposure of 100 W ultrasonic-waves for 15 minutes and so the product was centrifuged and washed using an ultrasonic-bath and centrifuged devices for 5 times, and finally it dried at 40 °C for 45 hours in an oven. The arranged (TeO_2:Cu-PVP) solution was grown onto frond of first-quarter p-Si wafer by using ultrasonic assisted method. Finally, the same Al rectifier contacts with 1 mm diameter were grown onto the (TeO_2:Cu-PVP) and onto front of second p-Si wafer. More explanation both on the cleaning procedure, growing of organic interlayer, and ohmic/rectifier contacts can be seen in (Pirgholi-Givi et al., 2021) references. The schematic impression of two type SDs were provided in Figure 1. The V-I measurements of them were performed by utilizing the Keithley-2400 source-meter.
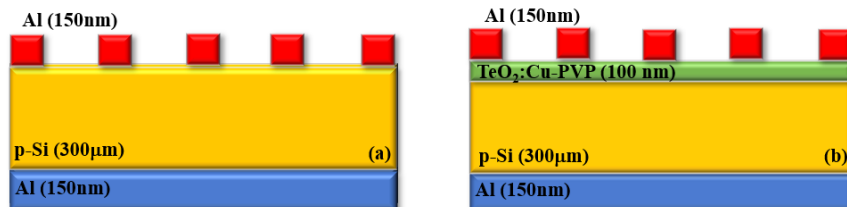

Figure 1. *Schematic diagram of the a) M-S and b) M-P-S type SDs*

3. RESULTS AND DISCUSSION

Some critical and fundamental electrical parameters, which are saturation-current (I_o), ideality-factor (n) and zero-bias B. H. (Φ_{b0}), and series resistance (R_s) of the manufactured MS and MIS diodes are conventionally calculated from the forward bias V-I records by employing thermionic-emission (TE) model (Sze, 1981;

Sharma, 1984; Rhoderick & Williams, 1988). When these structures have R_s and ideality factor higher than unity, the correlation between I and V is provided as presented below for $V_F \geq 3.(kT/q)$ (Sharma, 1984; Rhoderick & Williams, 1988):

$$I(V) = I_o[\exp\left(\frac{q(V - IR_s)}{nkT}\right) - 1]$$

(1)

In Equation 1, the values of I_o and n can be calculated via using the intercept and slope changes in the linear section of lnI vs V plot as given following relation, respectively.

$$I_o = AA^*T^2\exp\left(-\frac{q\phi_{bo}}{kT}\right) \text{ and } n = \frac{q}{kT}\left(\frac{dV}{d(\ln I)}\right)$$

(2)

Hence, Φ_{b0} value was calculated using I_o and A values as given follows.

$$\Phi_{bo} = (\frac{kT}{q})ln\left[\left(\frac{AA^*T^2}{I_0}\right)\right]$$

(3)

Figure 2 shows the ln (I_F)-V_F characteristics of the constructed type-1 and the type-2 SDs. It is seen that the lnI-V plots of these diodes have satisfying rectifying characteristic.

The value of R.R. is the ratio of the current at the exact same positive and negative voltages. Thus, I_o, n, Φ_{bo}, and R.R. (at ±5V) were obtained from the V-I data as 2.2×10^{-8} A, 1.829, 0.692 eV, 51.1 for Al/p-Si type and 2.3×10^{-6} A, 2.348, 0.576 eV, 286.2 for Al/(TeO$_2$:Cu-PVP)/p-Si type SDs, respectively. These structures series and shunt resistances also showed noteworthy effectuality in V-I measurements. While the value of R_s leads to deviation from linearity at high enough voltages in positive bias, R_{sh} leads to non-saturated in the reverse bias V-I plot, respectively (Çetinkaya et al., 2021; Ulusoy et al., 2023).
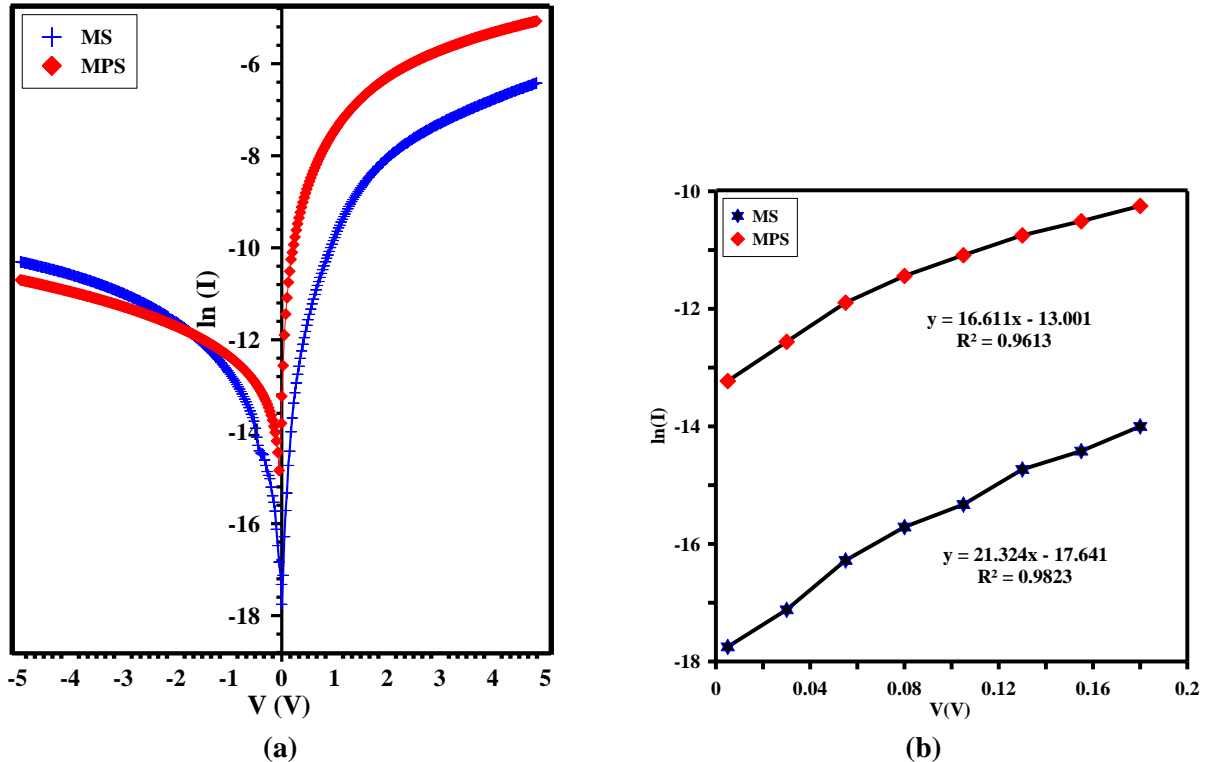

Figure 2. *a) The ln(I_F) - V_F curves for the two different kinds of fabricated SDs,*
b) The ln(I_F) – zoom (0 V_F -0.2 V_F) curves for the two different kinds of fabricated SDs

Both the existence of R_s and N_{ss} are more effective on the forward bias V-I characteristics. In general, R_s can be originated from the ohmic and rectifier contacts, the used probe wires to rectifier contact, the resistivity of bulk-semiconductor, and non-homogeneities of doping atoms in the semiconductor, the perform native or deposited interfacial layer at M/S interface. (Nicollian & Brews, 1982). There are different approaches to obtaining R_s in the literature, but Ohm's Law is the best (Sze, 1981; Sharma, 1984). According to this method, the structures resistance (R_i) shows dependency on voltage (V_i), but the actual R_s values for these structures show strong relations with high forward bias voltages. Obtained R_i values are shown in Figure 3 with R_i vs V graphs.

The voltage-dependent R_i ($=dV_i/dI_i$) versus V_i profile corresponds to higher reverse voltages, while R_s corresponds to higher forward voltages. R_i-and-R_s values for MS type are 2.86 kΩ, 0.15 MΩ, while 0.76 kΩ, 0.22 MΩ for MPS type SD. All basic electronic parameters (I_o, n, Φ_{bo}, R.R., R_s, R_{sh}) were also tabularized in Table 1. It is clear that there is an improvement in the MPS type SD compared to the MS type SD at room temperature.
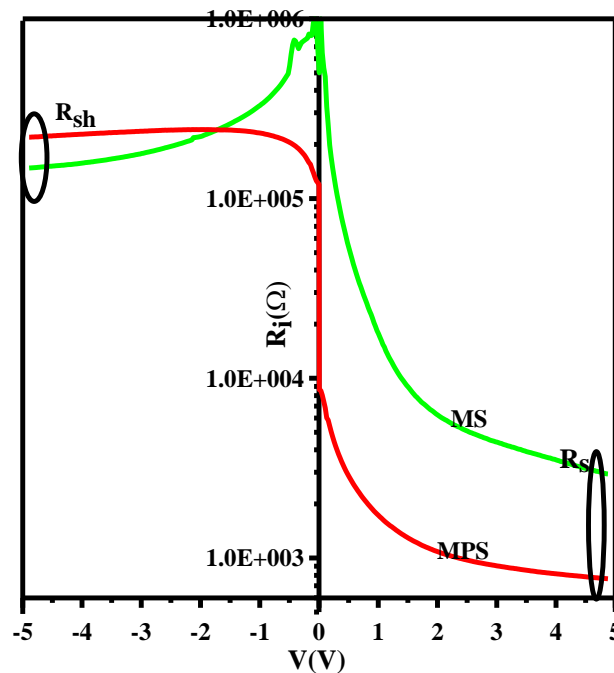

Figure 3. The Ln(R_i) vs V records of the fabricated M-S , M-P-S type SDs

Table 1. Fundamental electronic attributes of the type-1 and the type-2 SDs using the TE and Cheung's method

Samples	TE Theory				Cheung's Functions			
	I_0 (A)	n	Φ_b (eV)	R.R.	n	R_s (kΩ) dV/dln(I)-I	Φ_b (eV)	R_s (kΩ) H(I)-I
Al/p-Si	2.2×10^{-8}	1.83	0.692	51.1	6.84	2.31	0.54	2.56
Al/(PVP-TeO$_2$:Cu)/p-Si	2.3×10^{-6}	2.35	0.576	286.2	3.55	0.61	0.65	0.65

Table 1 indicates the used structures and methods, which show organic interfacial layer grown between interfaces, the efficiency of the MS type SD is directly related to the growth in R.R. and R_{sh} values versus the lessening of leakage-current, R_s, and N_{ss} values. The fundamental electrical parameters (n, Φ_{bo}, R_s) for two SDs were also calculated from the Cheung's functions as a second way (Cheung & Cheung, 1986). According to Cheung and Cheung (1986), the n, Φ_{bo}, R_s values were acquired alternatively by using I-V data in the light of following relations:

$$\frac{dV}{d(lnI)} = n\left(\frac{kT}{q}\right) + R_s I \tag{4a}$$

$$H(I) = V - n\left(\frac{kT}{q}\right) ln\left(\frac{I}{AA^*T^2}\right) = n\Phi_b + R_s I \tag{4b}$$

Figures 4a and 4b show the dV/dln(I) vs I and H(I) vs I plots of the type-1 and the type-2 SDs, in turn. As seen, these plots exhibit satisfying linear characteristics in a wide range of currents. The interception & inclination of the linear fit of dV/dLn(I)-I yielded the values of n & R_s as 6.84, 2.31 kΩ for MS and 3.55, 0.61 kΩ for MPS type SDs, respectively. After that by using these values of n in Equation 4(b), H(I) vs I yielded Φ_b and R_s as 0.54 eV, 2.56 kΩ for type-1 SD and 0.65 eV, 0.65 kΩ for the type-2 SD, in turn. Both the R_s and B.H. values were calculated by Cheung functions and compared to Ohm's Law. The observed discrepancies are the result of the nature of the chosen method and its dependence on voltage (Orak et al., 2017; Tanrıkulu et al., 2017; Altındal Yerişkin, 2019).
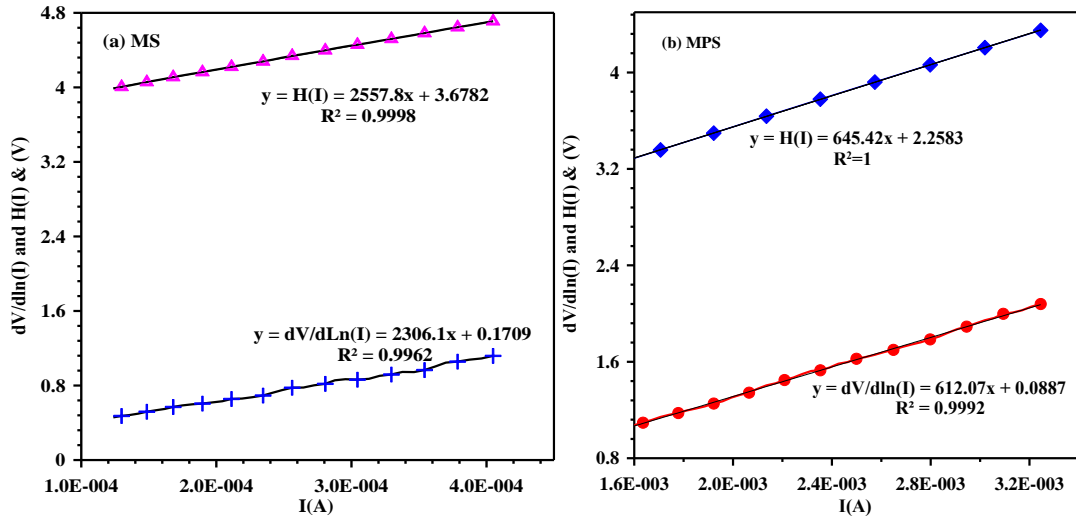

Figure 4. a), b) *The scatter* dV/dln(I) vs I and H(I) vs I *graphs of the M-S and M-P-S type SDs*

The effectiveness of surface states/traps (N_{ss}) on the conduction mechanisms is significantly greater in the intermediate forward polarization region. Defects or traps that have occurred between the semiconductor/interface with energy during the manufacture of the devices correspond to the semiconductors' band gap. These traps are usually rooted from the interruption of the periodic lattice-structure of the surface, cleaning of surface preparation, some impurities in the semiconductor, and the organic pollution in the laboratory environment and the energy dependence of them was calculated by subtracting positive polarization V-I data by using the Card & Rhoderick method (1971). The N_{ss} vs energy curve was extracted from V_F-I_F data by using following relations (Card & Rhoderick, 1971; Sharma, 1984; Altındal et al., 2019):

$$n(V) = \frac{qV_i}{kTln\left(\frac{I_i}{I_0}\right)} = 1 + \frac{d_i}{\varepsilon_i}\left[\frac{\varepsilon_s}{W_D} + qN_{ss}(V)\right] \tag{5a}$$

$$\Phi_e - \Phi_{b0} = \left(1 - \frac{1}{n(V)}\right)V_i \tag{5b}$$

In Equation 5 (a, b), the variables are presented successively as d_i, ε_s, ε_i, and W_D for the statements, the permittivity of the semiconductor, permittivity of the inter-layer, depletion layer breadth and the thickness of

inter-layer. Expression of N_{ss} in a dependency relation to energy is obtained from the following equation (5c) when considering the top of the E_v valence band (Card & Rhoderick, 1971).

$$E_{ss} - E_v = q(\Phi_e - V) \tag{5c}$$

For the MS and MPS type SDs, N_{ss} vs (E_{ss} - E_v) plots were obtained from Equation 5 (a-c) by using current-voltage measurements in forward bias voltage and given in Figure 5.
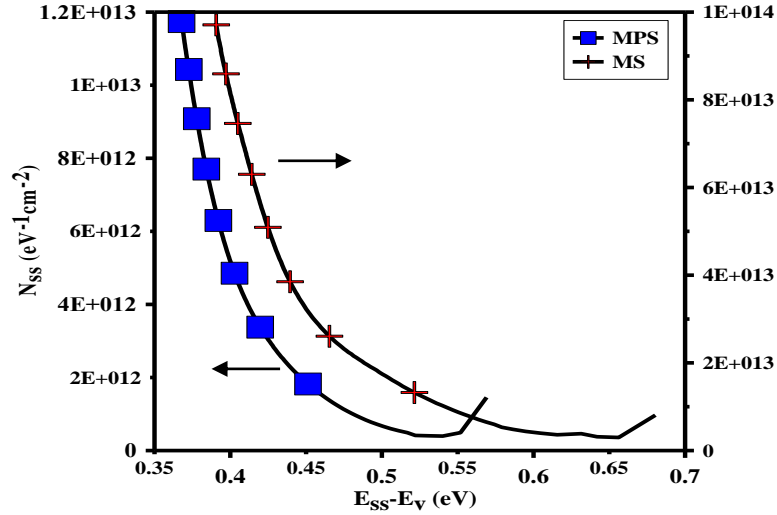

Figure 5. *The N_{ss}-(E_{ss}-E_v) profile of M-S and M-P-S type SDs*

The values of N_{ss} almost scaled up from the midgap of Si to the peak point of the valence-band E_v, as seen in Figure 5. While the value of N_{ss} changed between (9.71×10^{13} eV^{-1}cm^{-2}) at (0.39-E_v) and (8.07×10^{12} eV^{-1}cm^{-2}) at (0.68-E_v) for MS and (1.17×10^{13} eV^{-1}cm^{-2}) at (0.368-E_v) and (1.46×10^{12} eV^{-1}cm^{-2}) at (0.57-E_v) for MPS kind SD, in turn. These obtained values of N_{ss} are also suitable for the type-1 and the type-2 SDs. The N_{ss} value for the interlayered SD is about one order lower than the SD without an interfacial layer by virtue of the passivation effect of the (TeO$_2$:Cu-PVP) inter-layer used. For this reason, organic (TeO$_2$:Cu-PVP) can be a sufficient substitute for customary interfacial layers. Similar observations were also obtained by various researchers in the literature very recently (Demirezen & Altındal Yerişkin, 2020). Similar results on the R$_s$, N$_{ss}$, and interfacial layer in the SDs were also reported in the recent years (Çetinkaya et al., 2021; Demirezen et al., 2022; Ulusoy et al., 2023).

4. CONCLUSION

In this work, the MPS and MS-type SDs were fabricated onto a selfsame p-Si substrate to define the outcomes on fundamental electrical parameters of the (TeO$_2$:Cu-PVP) structure as an inter-layer by utilizing the V-I measurements in a voltage scale of ($\pm$5V) at room temperature. Since TE is available at moderate bias voltage ranges, and Cheung's functions are effective at high enough forward bias voltages, to observe the voltage and method dependencies of the fundamental electrical attributes of these structures, (n, Φ_{bo}, R$_s$) were acquired from both TE theory and Cheung's functions. Besides, the R$_{sh}$ and rectification-ratio values of aforesaid structures were also calculated from V-I data records at $\pm$5V. Finally, plots of surface state effects N$_{ss}$, highly related to energy, were also obtained from the V$_F$-I$_F$ data, the voltage dependency of $n(V)$ and B.H. The values of N$_{ss}$ changed from 9.71×10^{13} eV^{-1}.cm^{-2} at (0.39-E_v) to 8.07×10^{12} eV^{-1}.cm^{-2} at (0.68-E_v) for MS type SD and 1.17×10^{13} eV^{-1}.cm^{-2} at (0.368-E_v) to 1.46×10^{12} eV^{-1}.cm^{-2} at (0.57-E_v) for MPS type SD, respectively. These spin-offs reveal that the N$_{ss}$ value for type-1 SD is about one order higher than the type-2 SD because of the passivation effect of the organic (TeO$_2$:Cu-PVP) inter-layer investigated in this study. In other words, the used inter-layer leads to improvement of the M/S type SD, taking into account low leakage current/R$_s$/N$_{ss}$ values, and higher B.H., R.R., and R$_{sh}$ values. For this reason, organic (TeO$_2$:Cu-PVP) is a good candidate with satisfying electrical features for inter-layer replacements compared to traditional ones already in use.

ACKNOWLEDGEMENT

CONFLICT OF INTEREST

The author declares no conflict of interest.

REFERENCES

Altındal, Ş., Sevgili, Ö., & Azizian-Kalandaragh, Y. (2019). The structural and electrical properties of the Au/n-Si (MS) diodes with nanocomposites interlayer (Ag-doped ZnO/PVP) by using the simple ultrasound-assisted method. *IEEE Transactions on Electron Devices*, *66*(7), 3103-3109. doi:10.1109/TED.2019.2913906

Altındal Yerişkin, S. (2019). The investigation of effects of (Fe$_2$O$_4$-PVP) organic-layer, surface states, and series resistance on the electrical characteristics and the sources of them. *Journal of Material Sciences: Materials in Electronics*, *30*, 17032-17039. doi:10.1007/s10854-019-02045-x

Barkhordari, A., Özçelik, S., Altındal, Ş., Pirgholi-Givi, G., Mashayekhi, H., & Azizian Kalandaragh., Y. (2021). The effect of PVP: BaTiO$_3$ interlayer on the conduction mechanism and electrical properties at MPS structures. *Physica Scripta*, *96*(8), 085805. doi:10.1088/1402-4896/abeba8

Bindra, K., Bookey, H., Kar, A., Wherrett, B., Liu, X., & Jha, A. (2001). Nonlinear optical properties of chalcogenide glasses: Observation of multiphoton absorption. *Applied Physics Letters*, *79*, 1939–1941. doi:10.1063/1.1402158

Card, H. C., & Rhoderick, E. H. (1971). Studies of tunnel MOS diodes I. Interface effects in silicon Schottky diodes. *Journal of Physics D: Applied Physics*, *4*(10), 1589-1601. doi:10.1088/0022-3727/4/10/319

Cheung, S. K., & Cheung, N. W. (1986). Extraction of Schottky diode parameters from forward current-voltage characteristics. *Applied Physics Letters*, *49*, 85. doi:10.1063/1.97359

Coste, S., Lecomte, A., Thomas, P., Merle-M´ejean, T., & Champarnaud-Mesjard, J. C. (2007). Sol-gel synthesis of TeO$_2$-based materials using citric acid as hydrolysis modifier. *Journal of Sol-Gel Science and Technology*, *41*, 79–86. doi:10.1007/s10971-006-0117-6

Çetinkaya, H. G., Demirezen, S., & Altındal Yerişkin, S. (2021). Electrical parameters of Au/(%1Ni-PVA)/n-Si (MPS) structure: Surface states and their lifetimes. *Physica B: Condensed Matter*, *621*, 413207. doi:10.1016/j.physb.2021.413207

Demirezen, S., & Altındal Yerişkin, S. (2020). A detailed comparative study on electrical and photovoltaic characteristics of Al/p-Si photodiodes with coumarin-doped PVA interfacial layer: the effect of doping concentration. *Polymer Bulletin*, *77*, 49-71; doi:10.1007/s00289-019-02704-3

Demirezen, S., Altındal, Ş., Azizian-Kalandaragh, Y., & Akbaş, A. M. (2022) A comparison of Au/n-Si Schottky diodes (SDs) with/without a nanographite (NG) interfacial layer by considering interlayer, surface states (N$_{ss}$) and series resistance (R$_s$) effects. *Physica Scripta*, *97*(5), 055811. doi:10.1088/1402-4896/ac645f

Nicollian, E. H., & Brews, J. R. (1982). *MOS (Metal Oxide Semiconductor) Physics and Technology*. New York, USA: Wiley.

Orak., I., Koçyiğit, A., & Altındal, Ş. (2017). Electrical and dielectric characterization of Au/ZnO/n-Si device depending frequency and voltage. *Chinese Physics B*, *26*(2). doi:10.1088/1674-1056/26/2/028102

Pirgholi-Givi, G., Altındal, Ş., Asl., M. S., Namini, A. S., Farazin, J., & Azizian-Kalandaragh, Y. (2021) The effect of cadmium impurities in the (PVP–TeO$_2$) interlayer in Al/p-Si (MS) Schottky barrier diodes (SBDs): Exploring its electrophysical parameters. *Physica B: Condensed Matter*, *604*, 412617. doi:10.1016/j.physb.2020.412617

Reddy, M. S. P., Sreenu, K., Rajagopal Reddy, V., & Park, C. (2017) Modified electrical properties and transport mechanism of Ti/p-InP Schottky structure with a polyvinylpyrrolidone (PVP) polymer interlayer. *Journal of Material Science: Materials in Electronics, 28,* 4847-4855. doi:10.1007/s10854-016-6131-8

Rhoderick, E. H., & Williams, R. H. (1988). *Metal–Semiconductor Contacts*. Oxford. Clarendon Press.

Sharma, B. L. (1984). *Metal–Semiconductor Schottky Barrier Junctions and Their Applications*. New York and London. Plenum Press.

Shivachev, B. L., Petrov, T., Yoneda, H., Titorenkova, R., & Mihailova, B. (2009). Synthesis and nonlinear optical properties of TeO_2–Bi_2O_3–GeO_2 glasses. *Scripta Materialia*, *61*(5)*,* 493–496. doi:10.1016/j.scriptamat.2009.05.006

Suslick, K. S., & Doktycz, S. J. (1990). *The Effects of Ultrasound on Solids in Advances in Sonochemistry*, 1. Ed. T.J. Mason ed. New York. JAI Press.

Sze, S. M. (1981). *Physics of Semiconductor Devices*. New York. John Wiley & Sons.

Tanrıkulu, E. E., Demirezen, S., Altındal, Ş., & Uslu, İ. (2017). Analysis of electrical characteristics and conduction mechanisms in the Al/(%7 Zn-doped PVA)/p-Si (MPS) structure at room temperature. *Journal of Materials Science:Materials in Electronics*, *28*, 8844–8856. doi:10.1007/s10854-017-6613-3

Tataroğlu, A., Altındal, Ş., & Azizian-Kalandaragh, Y. (2020). C-V-f and G/ω-V-f characteristics of Au/(In_2O_3-PVP)/n-Si (MPS) structure. *Physica B: Condensed Matter*, *582*, 411996. doi:10.1016/j.physb.2020.411996

Ulusoy, M., Badali, Y., Pirgholi-Givi, G., Azizian-Kalandaragh, Y., & Altındal, Ş. (2023). The capacitance/conductance and surface state intensity characteristics of the Schottky structures with ruthenium dioxide-doped organic polymer interface. *Synthetic Metals*, *292*, 117243. doi:10.1016/j.synthmet.2022.117243

Analysis of Series Resistance's (R$_S$) Impact on Ag/Perylene/n-Si Schottky Barrier Diode (SBD) in Various Techniques

Esra YÜKSELTÜRK[1]* 🆔 Sedat ZEYREK[2] 🆔

[1]Ostim Technical University, Vocational School, Electronic and Automation Department, Ankara, Türkiye
[2]Kütahya Dumlupınar University, Faculty of Arts and Science, Physics Department, Kütahya, Türkiye

Keywords	Abstract
Ag/Perylene/n-Si SBD Series Resistance Ohm's Law Modified Norde Function Cheungs' Methods	The purpose of this research is to experimentally examine how R$_s$ affects the I-V curves of *Ag/Perylene/n-Si* SBD. Various plots of the experimental I-V measurements with the forward voltage are wielded in order to determine the parameter R$_s$. The I-V properties of *Ag/Perylene/n-Si* SBD was evaluated at room temperature (RT) based on Thermionic-Emission (TE) model. We specified the R$_s$ values using Ohm law, Cheungs', and modified Norde functions. We compared the R$_s$ values utilized various techniques. Modified Norde functions apply to the ln I-V graph's all forward voltage region. On the other hand, Cheung's approaches are just feasible in the non-linear section in the high voltage region. The R$_s$ values obtained from various techniques are distinct and are dedicated in the table. The reason for this inconsistency is shown in our research. It is evident that the values of the R$_s$ determined using various approaches are in good accordance with one another. The Ohm's law derived from sufficiently high forward voltages is the one among them that is the most straightforward, precise, and dependable. It was demonstrated by the I-V data that the dispersion of R$_s$ is a key factor affecting the electrical properties of diodes.

1. INTRODUCTION

Schottky barrier diodes, which are significant electronic devices in semiconductor technology, play a major role in metal-semiconductor technology because they feature an interface layer made of an insulator, ferroelectric, polymer, or composite materials. Metal-semiconductor-type SBDs transform into MIS/MFS/MPS-kind of SBDs when an interface is formed among metal and semiconductors. But, the inter-layer is higher than at about 4-5 hundred nanometers, this structures act a capacitor which storage more electrons or energy (Sze & Ng, 2007; Gencer Imer et al., 2019; Altındal et al., 2022). However, the used an interlayer can be considerably affect both the basic electrical parameters and conduction mechanism of these a structures. The performance or quality of these devices also depends on many parameters, such as the R$_s$, shunt-resistances (R$_{sh}$), barrier inhomogeneity, interface thickness and homogeneity, surface states (N$_{ss}$), and high-voltage (Norde, 1979; Cheung & Cheung, 1986; Sze & Ng, 2007; Rajagopal Reddy et al., 2014). According to Zeyrek et al. (2013) and Okur et al. (2019) the electrical features of these structures can be altered by using interfacial layers such as perylene, and DNA.

The prominence of MPS-type SBDs has increased because they have features like easy growth on the semiconductor, flexibility, and low cost in the last three decades (Sağlam et al., 2004; Yakuphanoglu, 2007; Özden et al., 2022). Among the conductive-polymers, the more important ones are the polythiophene, polyaniline, polyacetylene, PPy, and perylene because of they can easy to synthesize by chemical or electrochemical oxidation (Greene, 2009; Zeyrek et al., 2013). Therefore, we intended to build *Ag/Perylene/n-*

Si MPS-type SBDs rather than traditional MS or MIS. Then utilizing the I-V plots at RT, the electronic parameters n, Φ_B, R_s, R_{sh}, and rectification ratio (RR) was determined. Three linear regions with varying intercept points and slopes are depicted on the experimental I-V plot and correspond to low, moderate, and higher voltages. The I-V curve in the forward voltage shows the model of a multiple parallel diode.

2. MATERIAL AND METHOD

Ag/Perylene/n-Si MPS-type SBD was produced onto the n type Si. Before the processing, it was cleaned in trichloroethylene and ethanol, etched by CP4 (HNO3: HF: COOH C2H5: H2O =3:1:2:2 weight ratio) solution 30 s rinsed by propylene glycol. Following that, it washed with deionised-water (DW) and desiccated with N_2 gas. The wafer form tempered at 400°C to provide decent ohmic-contact. Here, Al was used as ohmic contact and Ag was used as rectifies contact. 1.26 mg of Perylene of 99% purity, branded Alfa Aesar, code L03047, was taken. It was mixed in 10 ml of Sigma-Aldrich brand 34856 coded Dichloromethane at 30°C for 2 hours on a magnetic stirrer. 0.5 mM (millimolar) solution was prepared. Afterward, Si wafers with ohmic contacts were coated with a layer of perylene using the spin coating method. The coating process was carried out at a rotation speed of 2000 rpm for 2 minutes. The processed was completed by thermally growing the rectifier contact on perylene at 10^{-6} Torr. The 3D structure diagram of perylene and schematic diagram of the sample were given in Figure 1. The measurements were realized at RT using Keithley-2400 SourceMeter.
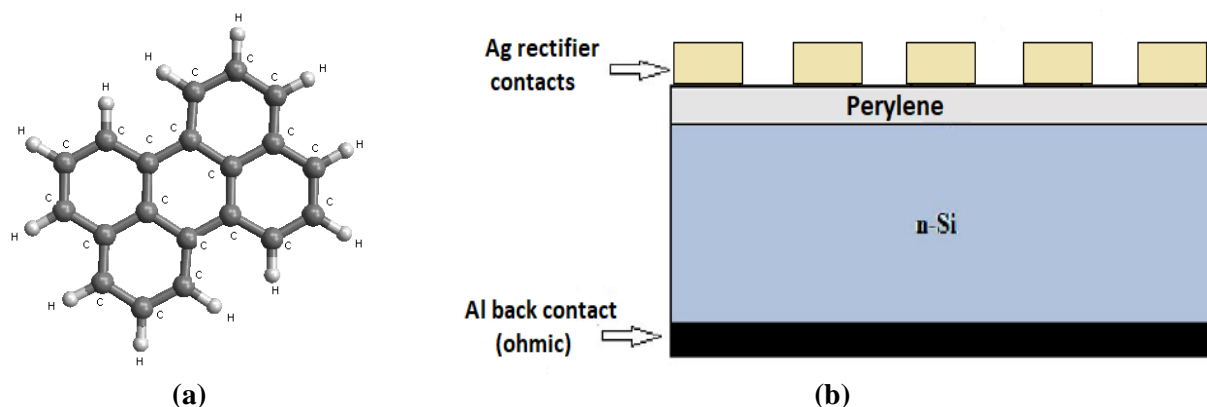

(a)   **(b)**

***Figure 1. a**)The 3D structure diagram of perylene ($C_{20}H_{12}$) (Zeyrek et al., 2013),*
***b)** The schematic illustration of the SBD.*

3. RESULTS AND DISCUSSION

The I-V curves of *Ag/Perylene/n-Si* SBD results examined at RT are shown in Figure 2. The I-V curve of the forward voltage increases exponentially. Furthermore, as illustrated in the inset of Figure 2, the I-V curve of the forward voltage has three different linear regions with distinct slopes, called region-1, 2 and 3 respectively. These multi-linear regions are referred to as the multi parallel diode model in the literature (Güçlü et al., 2016).

The rectification rates (RR=$I_{Forward}$/$I_{Reverse}$) were calculated in 0.5 V steps from ± 0.5 V to ±5 V and presented in Figure 3. The RR at V= ±0.5 V was even less than 1 (5.25×10^{-2}) (Figure 3), and especially reaching ~10^3 for ±5 V. This indicates that the *Ag/Perylene/n-Si* SBD could also be defined as a good diode as well as has being a high RR, good ohmic performance. Many investigations have demonstrated that a high rate of rectification is achieved by reducing the leakage current. Besides, it is also cognized that the RR, a crucial factor in diode efficiency, is affected by the interface quality and the impurities in the SiO_2/Si substrate. RRs are one of the most features for metal-semiconductor structures in electronic device technologies (Jaffery et al., 2020).

The I-V curve shows a linear behaviour but divergence from linearity owing to the impact of R_s under forward bias. The fundamental diode parameters such as n, Φ_{Bo}, I_o were derived using the TE equations for whole three regions based on the findings of I-V plot (Sze & Ng, 2007).

$$I_t = I_{01}\left[\exp\left(\frac{\beta(V\text{-}IR_S)}{n_1}\right) - 1\right] + I_{02}\left[\exp\left(\frac{\beta(V\text{-}IR_S)}{n_2}\right) - 1\right] + I_{03}\left[\exp\left(\frac{\beta(V\text{-}IR_S)}{n_3}\right) - 1\right] + \left(\frac{V - IR_S}{R_{sh}}\right) \tag{1}$$

$$n_i = \beta\left(\frac{dV}{d(lnI)}\right) \tag{2}$$

$$\Phi_{B0i} = \frac{1}{\beta} ln\left[\frac{AA^*T^2}{I_0}\right] \tag{3}$$

where β is a variable that changes with temperature and is calculated using the equation $\beta = q/kT$ (q, k, and T are well-known values in the literature). n, A, A*, and Φ_{Bo} are the ideality factor, contact-area of the diode, Richardson-constant of the semiconductor (for n-Si, it is equal to 112 A/(cm^2.K^2)), and zero-bias BH, respectively. I_o is the saturation current, and $I \cdot R_S$ denotes the voltage drop across the series resistor. The n_i, I_{oi}, and Φ_{Boi} values were found from the slope and intercept of the linear part ln(I)-V plot for three linear regions as 5.947, 4.37x10^{-7} A, 0.661 eV (for Region-I), 8.433, 4.64x10^{-6} A, 0.600 eV (for Region-II), and 7.593, 2.00x10^{-6} A, 0.621 eV (for Region-III), respectively. It is clear that these parameters are different in different voltage regions due to the voltage dependent of them.
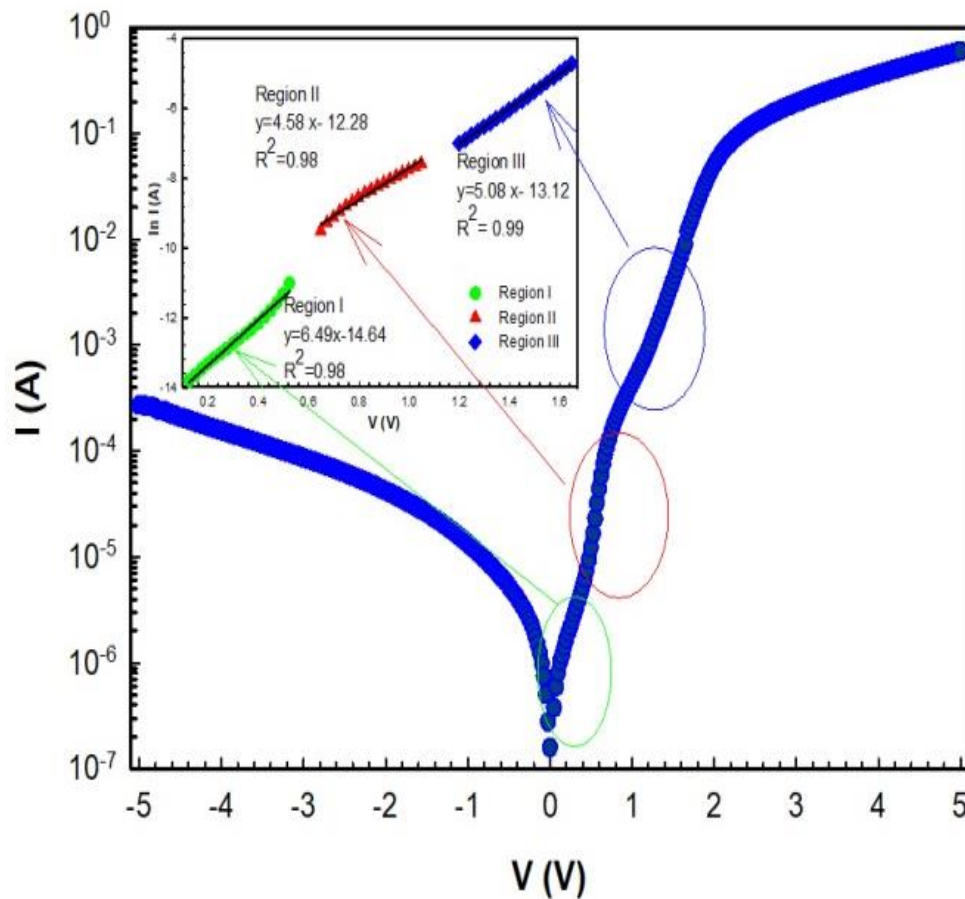
Figure 2. *I–V graph of the Ag/Perylene/n-Si SBD (inset the Region I, II, and III)*

Ohm's law ($R_i = V_i/I_i$) was used to calculate the measurements due to the significant influence of R_S. I-V plots for the samples were used and the results were shown in Figure 4. R_i values are constant in both the high forward and high reverse bias regions, and R_i corresponds to R_{sh} and R_s values in these regions. The R_{Sh} and R_S values were determined to be 18.45 kΩ and 8.347 Ω at (-5 V) and (+5V) voltage values, respectively.

Figure 3. Rectification Rates of the Ag/Perylene/n-Si SBD

Figure 4. Resistance values of the Ag/Perylene/n-Si SBD as a voltage dependent
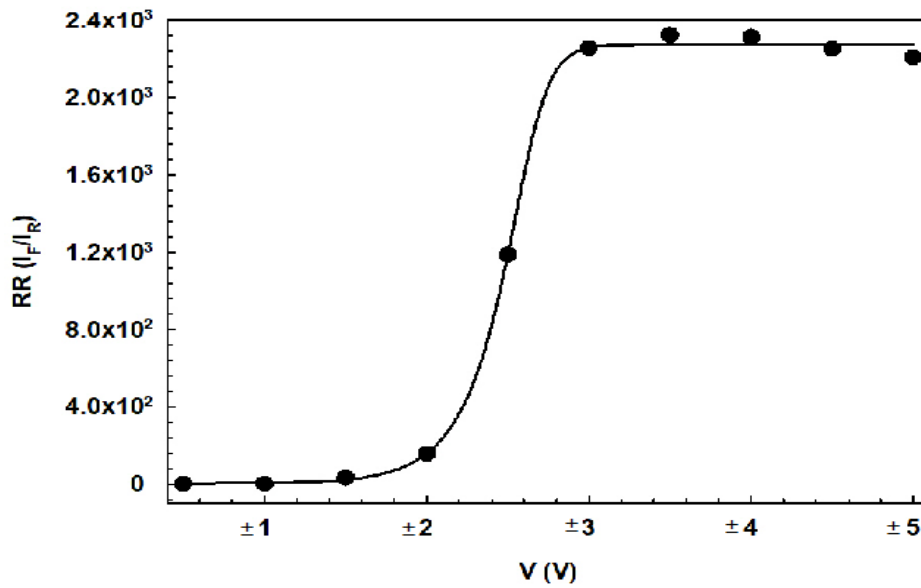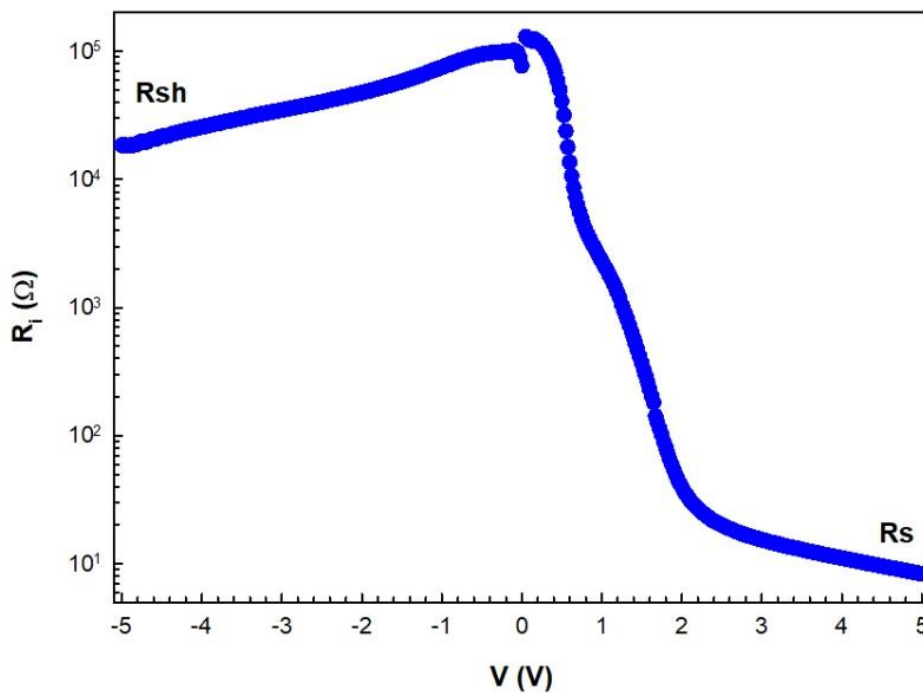
The R_S values are one of the major parameters influencing the electrical characteristics of *Ag/Perylene/n-Si* SBD. R_S is the significant source of minor signal loss in semiconductor devices. R_{sh} has a high value, making it ideal for an electronic device. R_{sh} could be caused by leak currents across the insulator among the front and rear contacts. Furthermore, R_{sh} might be caused by the shunt routes from the prob cable to the grounding, as well as the shunt resistance in the measurement device. The R_S is more influential in regions with sufficient forward voltage, whereas the R_{sh} is more potent in regions with reverse bias.

n and Φ_B values be determined only from the rectilinear section of the forward voltage region with TE theory. It is necessary to determine these parameters for the other bias region as well. The Cheungs' and modified Norde's functions can be used to do these computations in other regions (Norde, 1979; Bohlin, 1986; Cheung & Cheung, 1986).

Cheung's methods allow us to calculate the parameters n, Φ_B, and R_S in the region of descending curve of the I_F-V_F graphs. The n, Φ_{B0}, and R_s values are computed utilizing the given equations and presented in Table 1.

$$\frac{dV}{dln(I)} = \frac{nkT}{q} + R_S I \tag{4a}$$

$$H(I) = V - \frac{nkT}{q}\ln\left[\frac{I}{T^2 A^* A}\right] = R_S I + \Phi_{B0} n \tag{4b}$$

Table 1. *Various electronic parameters computed with diverce approaches from the I-V plot at RT*

TE Theory (For Region-III)				Ohm's-Law		Norde's-Function		Cheungs'-Methods			
								dV/dln (I)		H(I)	
n	I_0 (A)	Φ_{B0} (eV)	RR at ± 5 V	R_s at +5V (Ω)	R_{sh} at -5V (kΩ)	Φ_{B0} (eV)	R_s (Ω)	n	R_s (Ω)	Φ_{B0} (eV)	R_s (Ω)
7.59	2.00×10^{-6}	0.621	2.21×10^3	8.34	18.45	0.739	0.541	24.17	4.094	0.415	3.814

The Cheung functions determined as dV/dLn(I) which is known Cheung's 1st function and H(I) which is known as Cheung's 2nd function were plotted versus current. From Cheung's 1st functions. slope and intercept, it is possible to determine the n and R_s of a diode. Figure 5 and Eq. 4a are refered for this. Similarly, the slope and intercept of Cheung's 2nd functions may be used to derive the Φ_{B0} and R_s of a diode using Figure 6 and Eq. 4b. According to Cheung's 1st and Cheung's 2nd functions, the values of n, Φ_{B0}, and R_s were worked out, Table 1 shows them.

The results in Table 1, Figures 5 and 6 indicate that the R_S values acquired Cheung's methods concur. The calculated R_s values using the H(I)- I and dV/d(ln I)- I graphs demonstrate the Cheung method's consistency.

The modified Norde Function is an alternate approach for computing values such as R_s and Φ_B. The modified Norde function considers all forward voltage region of the curve, in which the current changes exponentially. The conventional TE method was utilized to determine the ideality factor employed in the R_s value computation. The Φ_{B0} and R_s values may be computed using the below formulas according to this function.

$$F(V) = \frac{V}{\gamma} - \frac{kT}{q}\ln\left(\frac{I(V)}{AA^*T^2}\right) \tag{5a}$$

$$\Phi_{B0} = F(V_{min}) + \frac{V_{min}}{\gamma} - \frac{kT}{q} \tag{5b}$$

$$R_S = \frac{kT(\gamma - n)}{qI_{min}} \tag{5c}$$

In Eq. 5a, F(V) and γ is an arbitrary constant and must be greater than n, which is derived from Eq. 2, respectively. In Eq. 5b and 5c, I_{min} is the current value matching the F(V)'s minimum. Likewise, V_{min} is the voltage value matching the F(V)'s minimum. The values of R_S and Φ_B were figured out by substituting the values of F(V_{min}), V_{min}, and I_{min} corresponding to F (V), V, and I values of the determined minimum F (V)-V graph (Figure 7), in Eq. 5b and 5c, and recorded in Table 1. The values of F(V_{min}), V_{min}, I_{min} was found as 0.593 V, 1.97 V, and 0.0463 A. Thus, the values of and Φ_B and Rs were calculated from Eq. 5b and 5c as 0.740 eV and 0.541 Ω by using the value of γ (1.5*n=11.385).
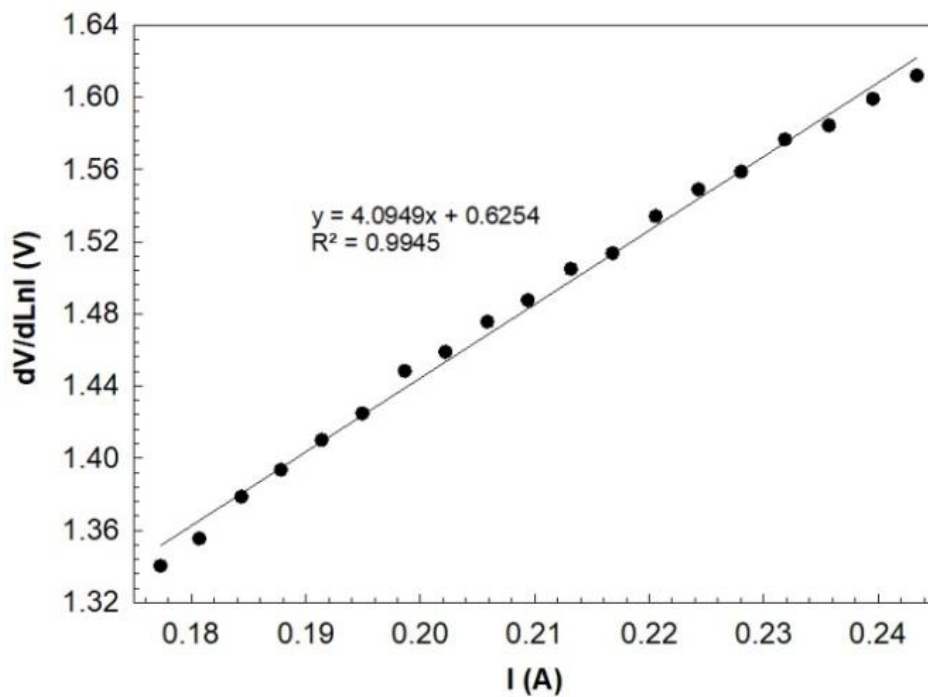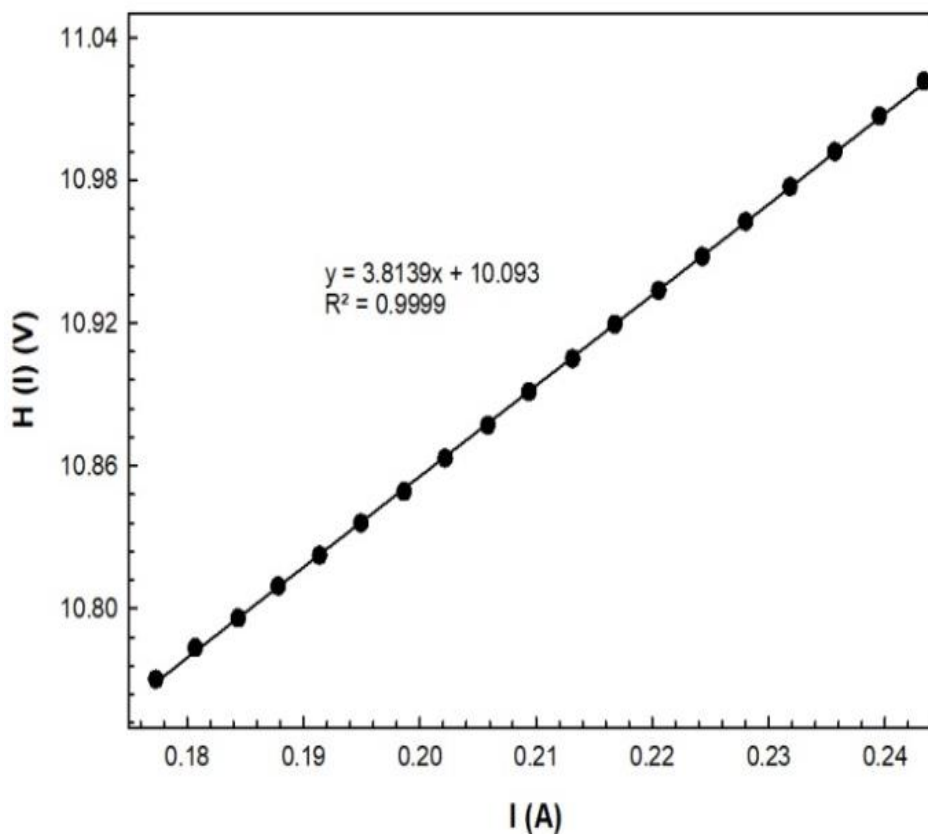
Figure 5. The dV/dln(I)-I plot of Ag/Perylene/n-Si SBD
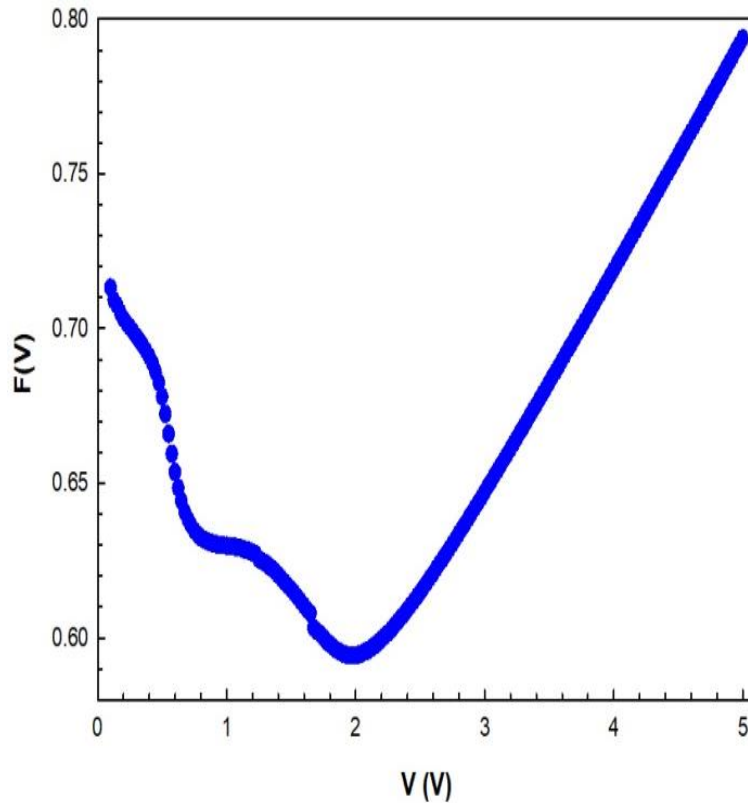

Figure 6. The H(I)-I plot of Ag/Perylene/n-Si SBD

Figure 7. F(V)-V plot for Ag/Perylene/n-Si SBD

It is seen that the R_S values in Table 1 determined using *Ohm law*, *Cheung's methods* and *modified Norde function* are distinct from each other (Turut et al., 2020). These approaches relate to various voltage region, which explains why the results obtained using these methods varies. The TE theory places emphasis on the linear portion, while Cheung's methods center on the downward curvature of the LnI-V graph. The Norde's function also emphasizes on the entire forward bias area. As a result, it describes how the value of R_s is impacted by changes in the applied voltage.

4. CONCLUSION

In this study, the influence of R_S on the I-V plot of the *Ag/Perylene/n-Si* SBD was investigated experimentally at RT. The values of R_S have been studied via various technics, including the theorem of TE and the functions of Cheung and Norde. The R_S values of *Ag/Perylene/n-Si* SBD were found as 8.34 Ω, 4.094 Ω and 3.814 Ω and 2.125 Ω using Ohm's-Law, Cheungs'-methods and Norde-function, respectively. It was noted that some inconsistencies were attributed to the limitations of the method, specifically due to the range of voltage used. The R_{sh} value was found from I-V data in the reverse voltage region using Ohm's law as 18.45 kΩ at -5 V. R_{sh} has a high value it appropriate for an electronic device. The RR was determined from I-V data as $\sim 10^3$ at V= ±5 V. This indicates that the *Ag/Perylene/n-Si* SBD has a very high RR, good ohmic behavior and is also as a good diode. As a result, the basic diode parameters such as I_o, n, Φ_{Bo} and Rs values were obtained by using TE, Norde and Cheungs methods. When these results were compared, it is clear that all these parameters are depended on bias voltage or the studied voltage range.

ACKNOWLEDGEMENT

CONFLICT OF INTEREST

The writer states that there is no competing interest or affiliation.

REFERENCES

Altındal, Ş., Özdemir, A. F., Aydoğan, Ş., & Türüt, A. (2022). Discrepancies in barrier heights obtained from current–voltage and capacitance–voltage of Au/PNoMPhPPy/n-GaAs structures in wide range of temperature. *Journal of Materials Science: Materials in Electronics*, *33*(15), 12210-12223. doi:10.1007/s10854-022-08181-1

Bohlin, K. E. (1986). Generalized Norde plot including determination of the ideality factor. *Journal of Applied Physics*, *60*(3), 1223-1224. doi:10.1063/1.337372

Cheung, S. K., & Cheung, N. W. (1986). Extraction of Schottky diode parameters from forward current-voltage characteristics. *Applied Physics Letters*, *49*(2), 85-87. doi:10.1063/1.97359

Gencer Imer, A., Korkut, A, Farooq, W A, Dere, A, Atif, M, Hanif, A., & Karabulut, A. (2019). Interface controlling study of silicon based Schottky diode by organic layer. *Journal of Materials Science: Materials in Electronic*s, *30*, 19239-19246. doi:10.1007/s10854-019-02282-0

Greene, M. (2009). Perylene Pigments. In: E. B. Faulkner & R. J. Schwartz (Eds.), *High Performance Pigments* (2nd ed.) (pp. 261-274). Wiley. doi:10.1002/9783527626915.ch16

Güçlü, Ç. Ş., Özdemir, A. F., & Altindal, Ş. (2016). Double exponential I–V characteristics and double Gaussian distribution of barrier heights in (Au/Ti)/Al$_2$O$_3$/n-GaAs (MIS)-type Schottky barrier diodes in wide temperature range. *Applied Physics A*, *122*(12), 1032. doi:10.1007/s00339-016-0558-x

Jaffery, S. H. A., Kim, J., Dastgeer, G., Hussain, M., Ali, A., Hussain, S., Eom, J., Hong, S., & Jung, J. (2020). Thickness-Dependent, Gate-Tunable Rectification and Highly Sensitive Photovoltaic Behavior of Heterostructured GeSe/WS$_2$ p–n Diode. *Advanced Materials Interfaces*, *7*(23), 2000893. doi:10.1002/admi.202000893

Norde, H. (1979). A modified forward I-V plot for Schottky diodes with high series resistance. *Journal of Applied Physics 50*(7), 5052-5053. doi:10.1063/1.325607

Okur, S., Yakuphanoglu, F., Ozsoz, M., & Kadayifcilar, P. K. (2009). Electrical and interface properties of Au/DNA/n-Si organic-on-inorganic structures. *Microelectronic Engineering*, *86*(11), 2305-2311. doi:10.1016/j.mee.2009.04.017

Özden, Ş., Avcı, N., Pakma, O., & Kariper İ. A. (2022). Influence of illumination intensity on the electrical properties of Al/NOA65/p-Si/Al heterojunction MPS device. *Journal of Materials Science: Materials in Electronics*, *33*(16), 12796-12807. doi:10.1007/s10854-022-08225-6

Rajagopal Reddy, V., Manjunath, V., Janardhanam, V., Kil, Y.-H., & Choi, C.-J. (2014). Electrical properties and current transport mechanisms of the Au/n-GaN Schottky structure with solution-processed high-k BaTiO3 interlayer. *Journal of Electronic Materials*, *43*(9), 3499-3507. doi:10.1007/s11664-014-3177-3

Sze, S. M., & Ng, K. K. (2007). *Physics of Semiconductor Devices* (3rd ed.). John Wiley & Sons, Inc. doi:10.1002/0470068329

Turut, A., Yıldız, D. E., Karabulut, A., & Orak, İ. (2020). Electrical characteristics of atomic layer deposited Au/Ti/HfO2/n-GaAs MIS-diodes in the wide temperature range. *Journal of Materials Science: Materials in Electronics*, *31*, 7839-7849. doi:10.1007/s10854-020-03322-w

Yakuphanoglu, F. (2007). The current-voltage characteristics of FSS/n-Si heterojunction diode under dark and illumination. *Physica B: Condensed Matter*, *388*(1-2), 226-229. doi:10.1016/j.physb.2006.05.430

Zeyrek, S., Acaroğlu, E., Altindal, Ş., Birdoğan, S., & Bülbül, M. M. (2013). The effect of series resistance and interface states on the frequency dependent C–V and G/w–V characteristics of Al/perylene/p-Si MPS type Schottky barrier diodes. *Current Applied Physics*, *13*(7), 1225-1230. doi:10.1016/J.CAP.2013.03.014

Adsorption Kinetics of Cu(II) and Ni(II) Ions Using Clay in Kulp District of Diyarbakır Province

Emine BULDAG[1]* 🆔 Ömer YAVUZ[2] 🆔

[1]Department of Chemistry, Institute of Science and Technology, Dicle University, Diyarbakır, Türkiye
[2]Department of Chemistry, Faculty of Science, Dicle University, Diyarbakır, Türkiye

Keywords	Abstract
Adsorption Copper Nickel Temparature	In this study, the adsorption kinetics of Cu(II) and Ni(II) ions in the aqueous medium of the natural clay sample found in Kulp district of Diyarbakır province were investigated. For this purpose, the characterization of the natural clay mineral found in Kulp district of Diyarbakır province was carried out using X-Ray (XRD and XRF) and BET methods. The copper and nickel from the aqueous medium was measurmented at 25, 35 and 45 degrees. When the obtained data were applied to other models, it was found that it followed the Ho McKay equation for both ions. The q_{max} values here were measured as 1.51, 2.05, 2.30 for Cu(II) and 1.044, 1.086 and 1.741 for Ni(II) at the working temperatures, respectively. The increase in q_{max} values shows the accuracy of our study.

1. INTRODUCTION

The development of the industry, increasing the number of heavy metals in the waters, created an important threat to environmental problems (Borst et al., 2020). It is necessary to remove heavy metals in polluted waters before giving them to the ecosystem. For this, many physical and chemical methods have become more popular recently.

The basis of the adsorption process is based on the equilibrium of unbalanced forces as a result of the interaction of molecules or ions in the aqueous medium with the groups on solid surface (Sarı & Tüzen, 2009). Natural adsorbents; clays, natural zeolites, bio sorbents can be given as examples. As an example of artificial adsorbents, activated charcoal and nanomaterials can be modified.

In order to remove cadmium and lead from the aqueous medium, calcalite was used as an absorbent. The measured values were found to be compatible with the Langmuir model. The percentages of removal at room temperature for natural calcite were determined to be approximately 20 mg/g for both metals (Yavuz et al., 2007).

Using palygorskite clay as a natural absorbent, lead, nickel, chrome and copper in river waters in South Africa were removed from the aqueous medium (Potgieter et al., 2006). Kaolinite and montmorillonite were used as adsorbent for iron, cobalt and nickel. Many parameters on metal removal were investigated (Bhattacharyya & Gupta, 2008). Modified Ünye clay was used for copper ions. Absorption capacity was found to be large (Eren, 2008).

*Corresponding Author, e-mail: ebuldag@hotmail.com

In other studies, natural kaolinite (Jiang et al., 2010), chitosan-clay composite (Tirtom et al., 2012), Nigerian kaolinite clay (Dawodu & Akpomie, 2014), modified Cucurbita moschata (a new adsorbent) (Khan & Rao, 2017), natural Arabian clay (Mu'azu et al., 2020) were used as absorbents and the removal of metal ions was achieved at a high rate.

In this study, natural clay found in Kulp district of Diyarbakır was used as absorbent. The effects of various temperatures and times were investigated to increase the adsorption of Cu(II) and Ni(II) ions to a high level. The analytical parameters of the method were measured. Its performance in removing ions was compared with other natural and modified absorbents in the literature.

2. MATERIAL AND METHOD

Materials

In the experiments, analytical purity $Cu(NO_3)_2$ and $Ni(NO_3)_2$ salts were used. The required amounts were weighed and 1000 mg/L stock solutions were prepared for each. Sortarious brand deionized water was used in the preparation of the solutions.

Clay sample

In this study, clay containing natural talc from Kulp district of Diyarbakir was used as adsorbent. The chemical content of the clay used as an adsorbent in the study; 63.4 % SiO_2, 0.2 % Al_2O_3, 0.2 % CaO, 3.3 Fe_2O_3, 26.4 %MgO, $\leq$ 1.0 % K_2O, $\leq$ 0.1 % Na_2O, $\leq$ 0.8 % TiO_2, $\leq$ 0.1 P_2O_5, $\leq$ 0.1 MnO and 5.30 % A.Za determined as a result of XRF analysis methods.

Characterization of clay

Clay sample containing natural talc brought from Kulp district of Diyarbakır was dried at approximately 100 °C. It was broken and ground and passed 150 mm electrified. Then it was dried again at 105 °C and stored in a desiccator to be used in experiments. The structure of the clay samples was determined by taking the XRD spectrum and is shown in Figure 1.
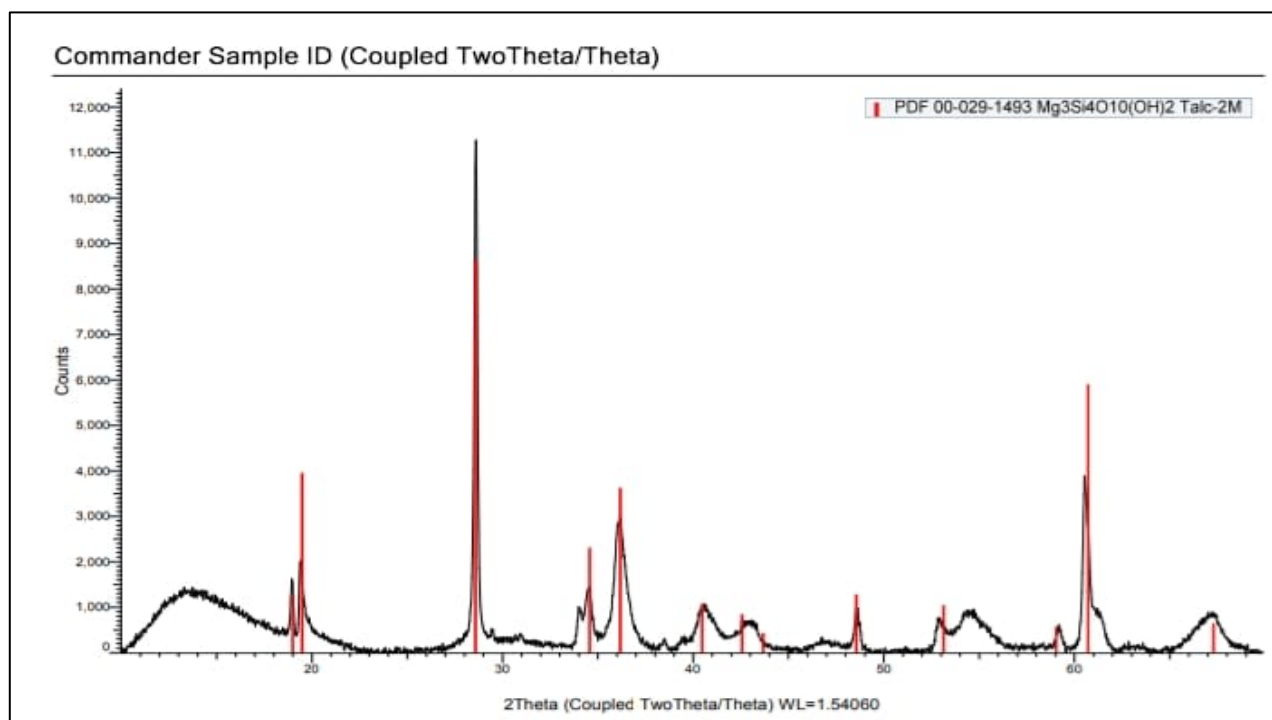

Figure 1. XRD spectrum of clay

Analyses of Cu(II) and Ni(II)

Analyses of Cu(II) and Ni(II) in aqueous media were investigated depending on temperature and time. Stock solutions of these two ions were prepared 10 ml each of the solutions containing both ions to be examined were transferred to 100 ml reagent bottles and a certain amount of clay sample was placed. It was shaken for a certain time and at certain temperatures. The clay was then separated using a centrifugation step for 15 minutes. Metal concentrations in solution were measured by atomic absorption spectrometry. Hollow cathode lamps of ions were used in the analysis. Lights with wavelengths of 327.39 and 231.60 nm were selected for the analysis of Cu(II) and Ni(II) ions.

Theory of adsorption

The measured data were applied to other models and the results were compared. The parameter that is effective in the compatibility of the measured values with the models is the correlation coefficient. During operation, the effect of contact time and temperature was examined. Measurements were made when Cu and Ni concentrations were 100 mg l^{-1} and adsorbent amount was 1 g. The adsorption of metal ions depends on the pH of the absorbent medium. The silicon value in the absorbent content determines the working pH value of the environment. Since the clay contains 57% silicon dioxide, the appropriate pH range 6 was used.

Since adsorption is time dependent, it is important to measure the equilibrium contact time in adsorption kinetics. The following models are used to determine the equilibrium contact times.

Lagergren Model: It was the first of the kinetic model. It is done by the Equation (1) given below (Yavuz et al., 2002). An increase in the q value indicates an increase in adsorption.

$$\ln(qm - qt) = \ln qm - k_1 t \tag{1}$$

Ho McKay Model: This model is the kinetic model developed (Ho & Mckay, 1998). The expression showing how the adsorption capacity changes with time is given in Equation (2).

$$\frac{t}{qt} = \frac{1}{K2\, qe^2} + \frac{t}{qe} \tag{2}$$

Elovich Kinetic Model: This model gives information about the adsorption process on the solid surface. This model also took place in the literature as the model developed by Roginsky and Zeldovich and was formulated as Equation (3) (Baytar et al., 2018).

$$qt = \frac{1}{\beta}(\ln \alpha\beta) + \frac{1}{\beta}\ln t \tag{3}$$

Weber-Morris Kinetic Model: This model was preferred to examine the internal particulate diffusion phenomenon. In this model, using the formula in Equation (4), the effect of boundary layer resistance, balance, velocity and contact time from the parameters of solution adsorption is measured (Onursal et al., 2020).

$$qt = k_i\sqrt{t} + C \tag{4}$$

3. RESULTS AND DISCUSSION

Kinetic studies of Cu(II)

In kinetic studies, the contact time and the amount of adsorbed substance are examined. For this purpose, the amount of adsorbed material was measured between 0-140 minutes and at 25, 35 and 45 degress. The data were given in the figures (Dal et al., 2021). When Figure 2 is examined, as the time increases, the amount of adsorbed material decreases and at the same time the temperature decreases. With the increase in the amount

of adsorbed substance observed to increase (Fu et al., 2021). Adsorption graphs of Cu(II) according to kinetic models are given as Figures 3, 4, 5 and 6.
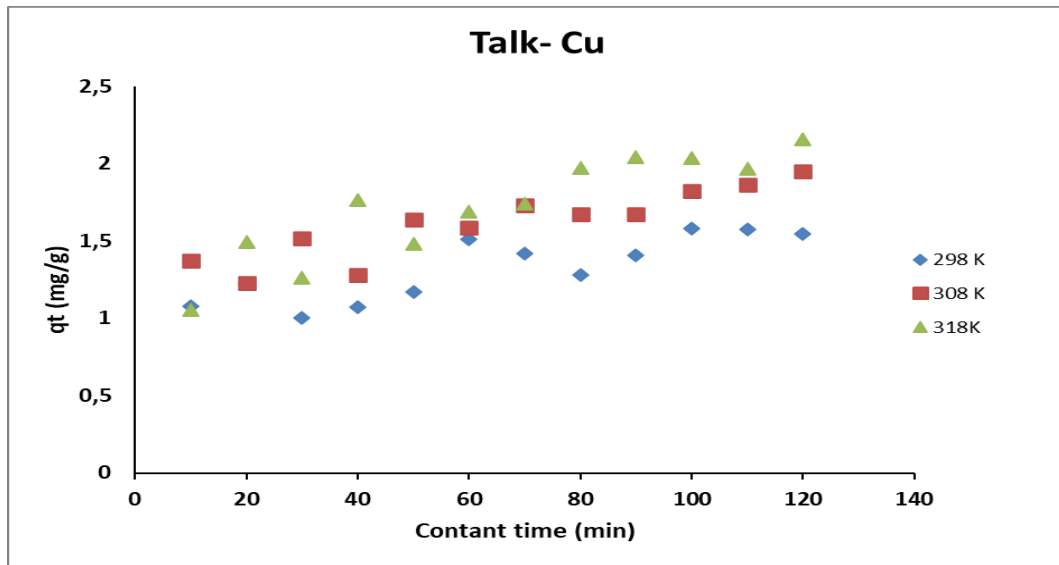

Figure 2. *The contact time on Cu(II) concentration*
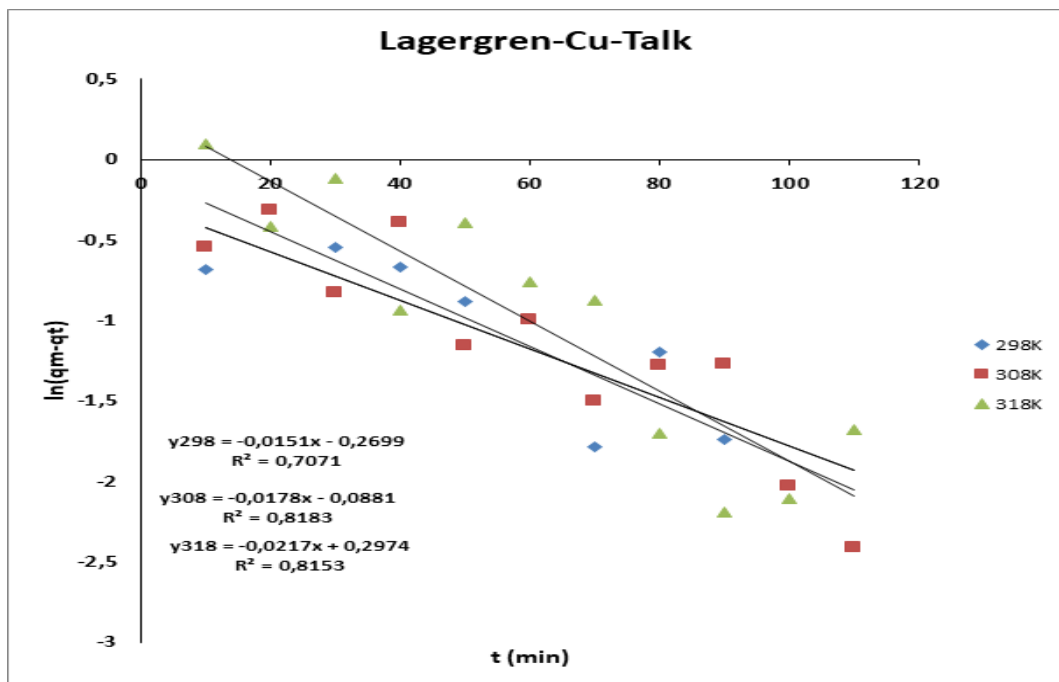
Figure 3. *Lagergren plot of Cu(II) adsorption*
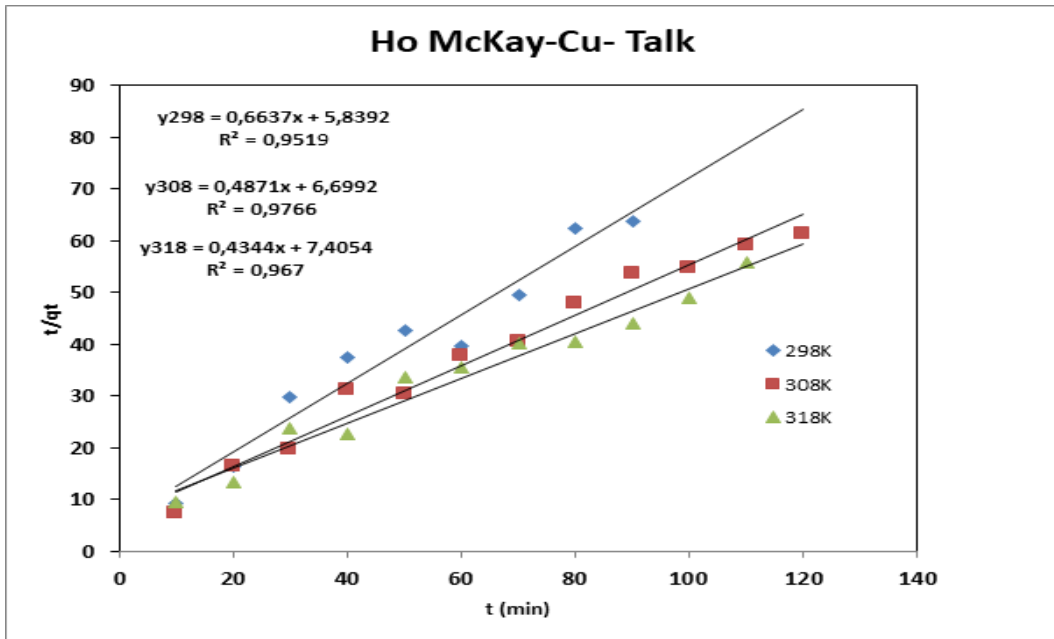
Figure 4. *Ho-Mac Kay plot of Cu(II) adsorption*
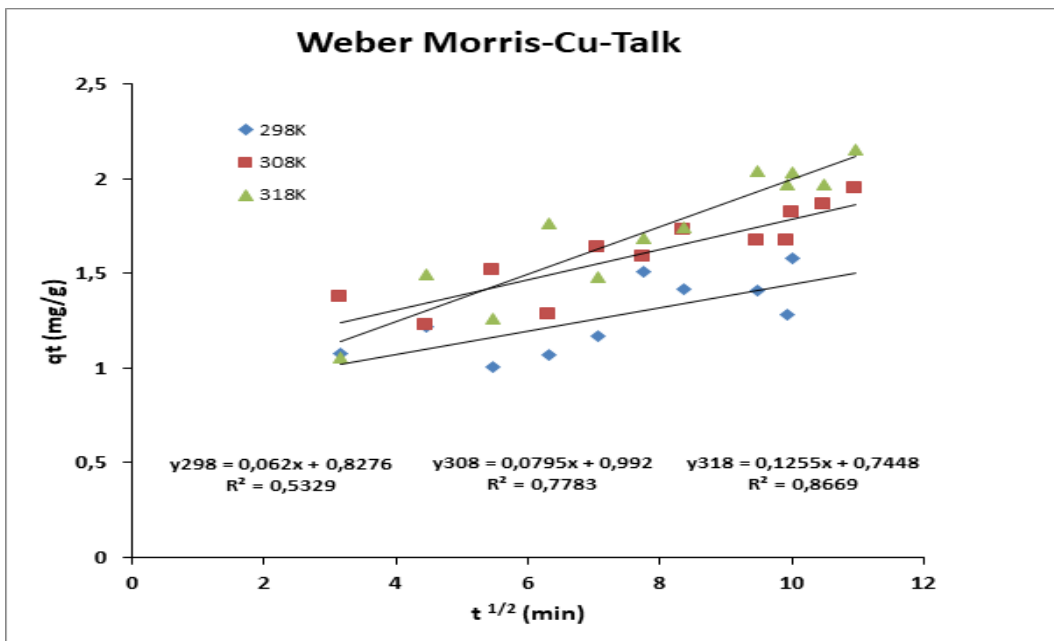
Figure 5. *Weber-Morris plot of Cu(II) adsorption*
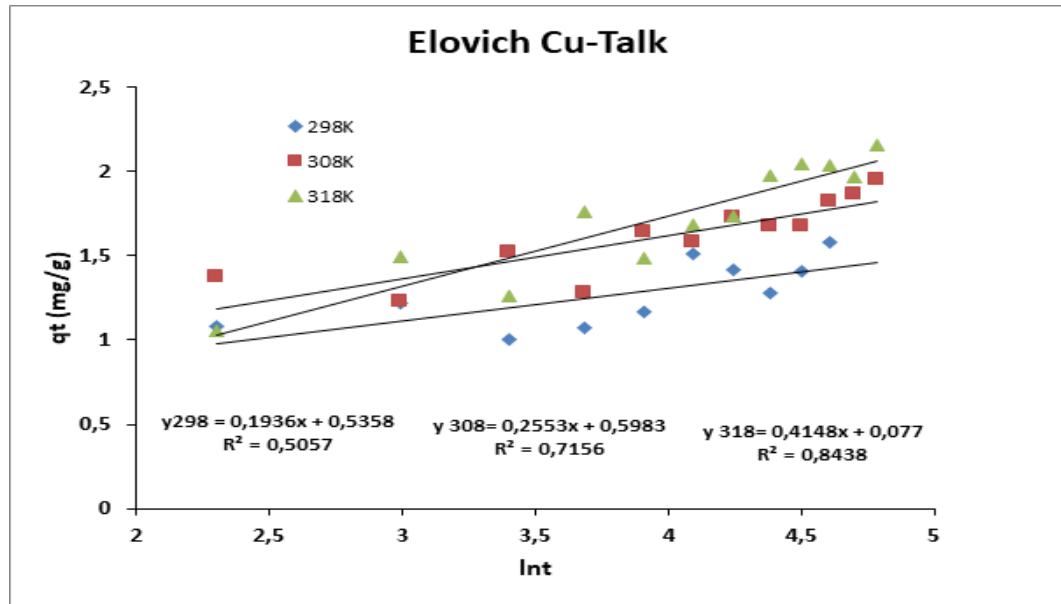
Figure 6. Elovich plot of Cu adsorption (II)

Data from models are shown in Table 1.

Table 1. Parameters according to kinetic velocity models

Lagergren's Equation	$ln(q_e - q_t) = lnq_e - k_1 t$			
(°K)	Line Equation	R^2	$k_1 = m$	$n = lnq_e$
298	y=-0,0154x-0,4696	0,37	0,0154	0,4696
308	y=-0,0178x-0,0881	0,82	0,0178	-0,0881
318	y=-0,0217x+0,2974	0,81	0,0217	0,2974

Ho McKay's Equation	$t/q_t = t/q_e + 1/k_2 q_e^2$			
(°K)	Line Equation	R^2	q_e (mg/g)	k_2
298	y=0,6637x+5,8392	0,95	1,51	0,0007
308	y=0,4871x+6,6992	0,98	2,05	0,0239
318	y=0,4344x+7,4054	0,97	2,30	0,0255

Weber-Morris's Equation	$q_t = C_b + K_{WM}\sqrt{t}$			
(°K)	Line Equation	R^2	K_{WM}	C_b
298	y=0,0662x+0,8276	0,53	0,0662	0,8276
308	y=0,0795x+ 0,9920	0,78	0,0795	0,9920
318	y=0,1255x+0,7448	0,87	0,1255	0,7448

Elovich's Equation	$q_t = (1/\beta) ln(\alpha\beta) + (1/\beta) ln\, t$			
(°K)	Line Equation	R^2	β	α
298	y=0,1936x+0,558	0,50	5,1652	3,455
308	y=0,2553x+0,5983	0,71	3,9170	2,659
318	y=0,4148x+0,077	0,84	2,4108	0,499

Kinetic studies of Ni(II)

Adsorption studies of Ni(II) were performed by applying the procedure in Cu(II) (Ewis et al., 2022). First of all, the contact time of Ni(II) at 298K, 308K and 318K was measured within 0-140 seconds and is show in Figure 7.
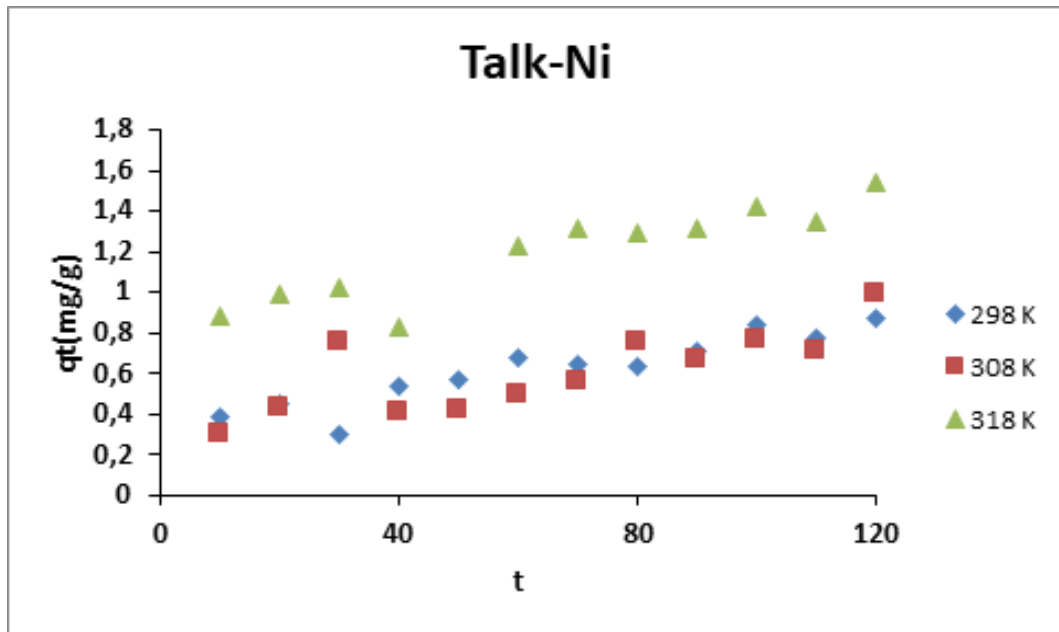
Figure 7. *The contact time on Ni(II) concentration*

Adsorption graphs of Ni(II) according to kinetic models are given as Figures 8, 9, 10 and 11.
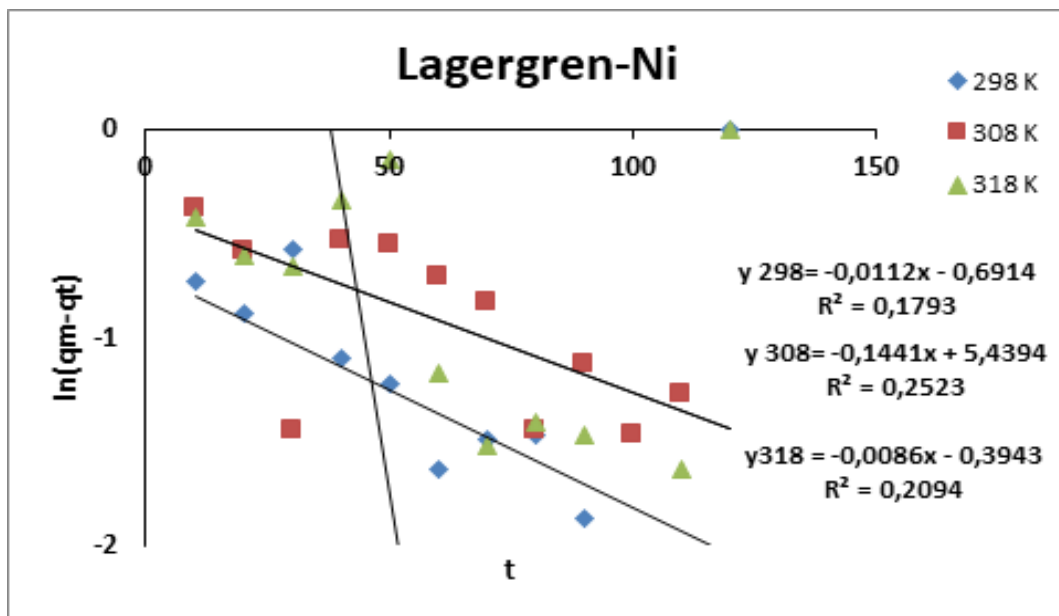
Figure 8. *Lagergren plot of Ni adsorption (II)*
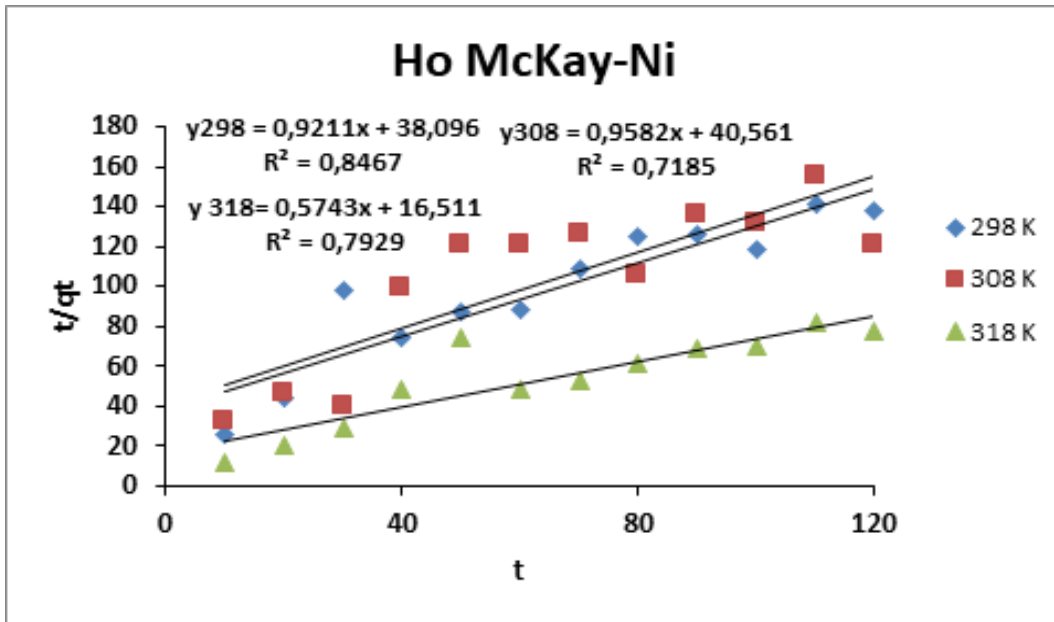
Figure 9. *Ho-Mac Kay plot of Ni(II) adsorption*
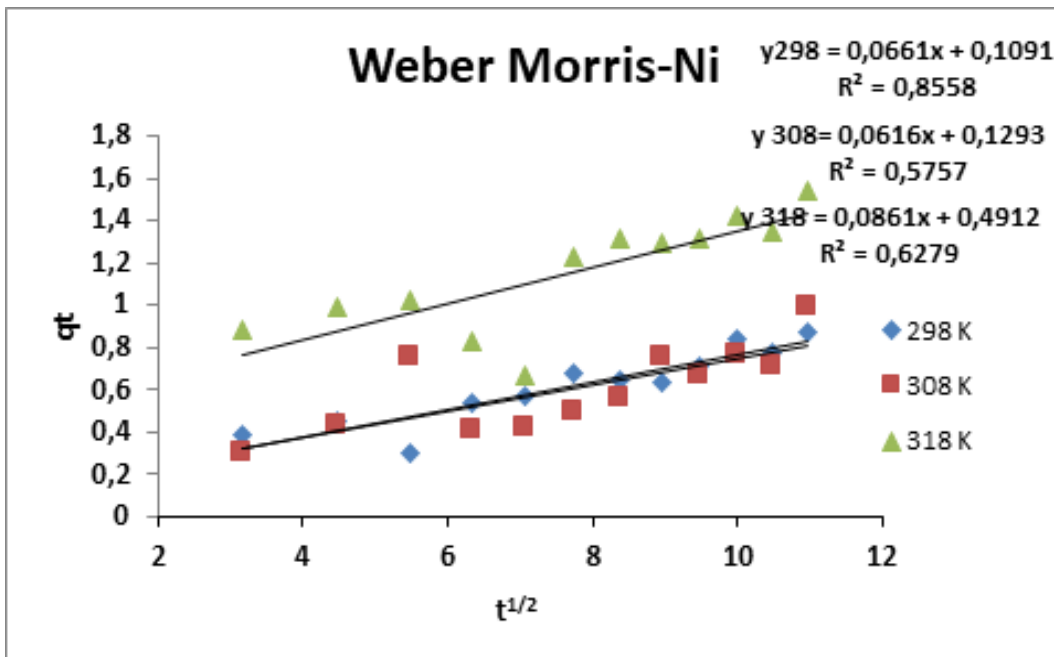
***Figure 10.*** *Weber-Morris plot of Ni(II) adsorption*
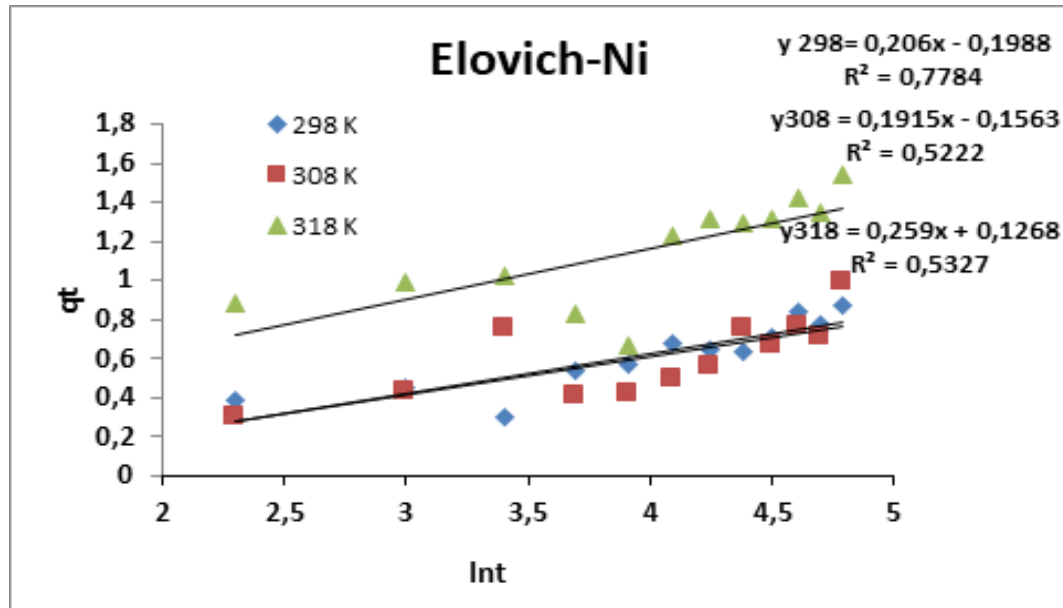
Figure 11. *Elovich plot of Ni(II) adsorption*

Data from models are shown in Table 2.

Table 2. *Parameters according to kinetic velocity models*

Lagergren's Equation		$ln(q_e - q_t) = lnq_e - k_1 t$		
(°K)	Line Equation	R^2	$k_1 = m$	$n = lnq_e$
298	y=-0,0112X-0,6914	0,18	-0,0112	-0,6914
308	y=-0,1441X+5,4394	0,25	-0,1441	5,4394
318	y=-0,0086X-0,3943	0,21	-0,0086	-0,3943

Ho McKay's Equation		$t/q_t = t/q_e + 1/k_2 q_e^2$		
(°K)	Line Equation	R^2	q_e (mg/g)	k_2
298	y=0,9211X+38,096	0,85	1,086	0,022
308	y=0,9582X+40,561	0,72	1,044	0,023
318	y=0,5743X+16,511	0,79	1,741	0,019

Weber-Morris's Equation		$q_t = C_b + K_{WM}\sqrt{t}$		
(°K)	Line Equation	R^2	K_{WM}	C_b
298	y=0,0661X+0,1091	0,85	0,0661	0,1091
308	y=0,0616X+0,1293	0,57	0,0616	0,1293
318	y=0,0861X+0,4912	0,63	0,0861	0,4912

Elovich's Equation		$q_t = (1/\beta) \ln(\alpha\beta) + (1/\beta) \ln t$		
(°K)	Line Equation	R^2	β	α
298	y=0,206X-0,1988	0,78	4,854	0,078
308	y=0,1915X-0,1563	0,52	5,222	0,084
318	y=0,259X+0,1268	0,53	3,861	0,422

4. CONCLUSION

In this study, the chemical structure of the clay sample brought from the Kulp district of Diyarbakır was examined using XRD. Using XRF, its chemical structure was determined as 63.4 % SiO_2, 0.2 % Al_2O_3, 0.2 % CaO, 3.3 Fe_2O_3, 26.4 %MgO, ≤ 1.0 % K_2O, ≤ 0.1 % Na_2O, ≤ 0.8 % TiO_2, ≤ 0.1 P_2O_5, ≤ 0.1 MnO and 5.30 % A.Za determined as a result of XRF analysis methods.

This clay sample was also used as an adsorbent in our studies. Both ion samples were shaken with this adsorbent at 298K, 308K and 318K for 0-140 minutes. The adsorption kinetics of the samples were investigated.

The adsorption kinetics of this sample were carried out separately for both Cu(II) ion and Ni(II) ion at different temperatures using Lagergren, Ho-Mac Kay, Weber-Morris and Elovich equations. The qmax values were calculated as 1.51, 2.05 and 2.30 for Cu(II) and 1.086, 1.044 and 1.741 for Ni(II) at the working temperatures, respectively. The increase in qmax values shows the accuracy of our study.

According to the measurements obtained, the adsorption kinetics of the adsorbent for both ion samples were found to be in accordance with the Ho-Mac Kay equation. The correlation coefficient of the results obtained for this equation was measured higher. This shows that the sensitivity is high for us.

ACKNOWLEDGEMENT

CONFLICT OF INTEREST

The authors declare no conflict of interest.

REFERENCES

Baytar, O., Ceyhan, A. A., & Şahin, O. (2018). İğde Çekirdeğinden Elde Edilen Aktif Karbon Kullanılarak Sulu Çözeltilerden Pb(II) Adsorpsiyonun İncelenmesi: İzoterm ve Kinetik. *Bitlis Eren Üniversitesi Fen Bilimleri Dergisi*, *7*(2), 256-267. doi:10.17798/bitlisfen.422446

Bhattacharyya, K. G., & Gupta, S. S. (2008). Kaolinite and montmorillonite as adsorbents for Fe(III), Co(II) and Ni(II) in aqueous medium. *Applied Clay Science*, *41*(1-2), 1-9. doi:10.1016/j.clay.2007.09.005

Borst, A. B., Smith, M. P., Finch, A. A., Estrade, G., Villanova-de-Benavent, C., Nason, P., Marquis, E., Horsburgh, N. J., Goodenough, K. M., Xu, C., Kynický, J., & Geraki, K. (2020). Adsorption of rare earth elements in regolith-hosted clay deposits. *Nature Communications*, *11*(1), 4386. doi:10.1038/s41467-020-17801-5

Dal, M. C., Onursal, N., Arıca, E., & Yavuz, Ö. (2021). Diyarbakır Karacadağ Kırmızı Tepe Skoryası ile Cu(II) Adsorpsiyon Kinetiğinin İncelenmesi. *Dicle Üniversitesi Mühendislik Fakültesi Mühendislik Dergisi*, *12*(2), 337-346. doi:10.24012/dumf.881650

Dawodu, F. A., & Akpomie, K. G. (2014). Simultaneous adsorption of Ni(II) and Mn(II) ions from aqueous solution unto a Nigerian kaolinite clay. *Journal of Materials Research and Technology*, *3*(2), 129-141. doi:10.1016/j.jmrt.2014.03.002

Eren, E. (2008). Removal of copper ions by modified Unye clay, Turkey. *Journal of Hazardous Materials*, *159*(2-3), 235-244. doi:10.1016/j.jhazmat.2008.02.035

Ewis, D., Ba-Abbad, M. M., Benamor, A., & El-Naas, M. H. (2022). Adsorption of organic water pollutants by clays and clay minerals composites: A comprehensive review. *Applied Clay Science*, *229*, 106686. doi:10.1016/j.clay.2022.106686

Fu, C., Zhu, X., Dong, X., Zhao, P., & Wang, Z. (2021). Study of adsorption property and mechanism of lead(II) and cadmium(II) onto sulfhydryl modified attapulgite. *Arabian Journal of Chemistry*, *14*(2), 102960. doi:10.1016/j.arabjc.2020.102960

Ho, Y. S., & Mckay, G. (1998). Kinetic Models for The Sorption of Dye from Aqueous Solution by Wood to Pollutant Removal on Various Sorbents. *Process Safety and Environmental Protection*, *76*(2), 183-191. doi:10.1205/095758298529326

Jiang, M., Jin, X., Lu, X.-Q., & Chen, Z. (2010). Adsorption of Pb(II), Cd(II), Ni(II) and Cu(II) onto natural kaolinite clay. *Desalination*, *252*(1-3), 33-39. doi:10.1016/j.desal.2009.11.005

Khan, U., & Rao, R. A. K. (2017). A high activity adsorbent of chemically modified *Cucurbita moschata* (a novel adsorbent) for the removal of Cu(II) and Ni(II) from aqueous solution: Synthesis, characterization and metal removal efficiency. *Process Safety and Environmental Protection*, *107*, 238-258. doi:10.1016/j.psep.2017.02.008

Mu'azu, N. D., Bukhari, A., & Munef, K. (2020). Effect of montmorillonite content in natural Saudi Arabian clay on its adsorptive performance for single aqueous uptake of Cu(II) and Ni(II). *Journal of King Saud University-Science*, *32*(1), 412-422. doi:10.1016/j.jksus.2018.06.003

Onursal, N., Dal, M. C., Kul, A. R., Yavuz, Ö. (2020). Cu(II) iyonlarının doğal karışık tipteki kil ile sulu ortamdan uzaklaştırılması, izoterm, kinetik ve termodinamik parametrelerin incelenmesi. *Eurasia Journal of Mathematics, Engineering, Natural & Medical Sciences*, *7(9)*, 85-103. doi:10.38065/euroasiaorg.84

Potgieter, J. H., Potgieter-Vermaak, S. S., & Kalibantonga, P. D. (2006). Heavy metals removal from solution by palygorskite clay. *Minerals Engineering*, *19*(5), 463-470. doi:10.1016/j.mineng.2005.07.004

Sarı, A., & Tüzen, M. (2009). Kinetic and equilibrium studies of biosorption of Pb(II) and Cd(II) from aqueous solution by macro fungus (Amanita rubescens) biomass. *Journal of Hazardous Materials*, *164*(2-3), 1004-1011. doi:10.1016/j.jhazmat.2008.09.002

Tirtom, V. N., Dincer, A., Becerik, S., Aydemir, T., & Celik, A. (2012). Comparative adsorption of Ni(II) and Cd(II) ions on epichlorohydrin crosslinked chitosan–clay composite beads in aqueous solution. *Chemical Engineering Journal*, *197*, 379-386. doi:10.1016/j.cej.2012.05.059

Yavuz, Ö., Altunkaynak, Y., & Güzel, F. (2002). Removal of copper, nickel, cobalt and manganese from aqueous solution by kaolinite. *Water Research*, *37*(4), 948-952. doi:10.1016/S0043-1354(02)00409-8

Yavuz, O., Guzel, R., Aydin, F., Tegin, I., & Ziyadanogullari, R. (2007). Removal of Cadmium and Lead from Aqueous Solution by Calcite. *Polish Journal of Environmental Studies*, *16*(3), 467-471.

Illumination Response of Impedance Properties of Al/Gr-PVA/p-Si (MPS) Device

Dilan ATA[1*] Muzaffer BALBAŞI[1] Adem TATAROĞLU[2]

¹Gazi University, Faculty of Engineering, 06570, Ankara, Türkiye
²Gazi University, Faculty of Science, 06560, Ankara, Türkiye

Keywords	Abstract
Gr Doped PVA Illumination Admittance Basic Electrical Parameters	Admittance measurements including capacitance (C) and conductance (G) of Al/Gr-PVA/p-Si (MPS) device were made at 500 kHz and under dark and 200 mW/cm2 conditions. The illumination response on the electric characteristics of the device was investigated using the C-2-V characteristics. It was observed that the electronic parameters of the device changed depending on the illumination conditions. The doping concentration, Fermi energy and barrier height were obtained using the C-2-V data. The surface state (Nss) was also obtained using capacitance data. The results show that the device can be used as a photocapacitor.

1. INTRODUCTION

Graphene (Gr) is one of the most promising materials due to its outstanding electric, optic, mechanic and thermal characteristics, such as strong electrical conductivity, high electron mobility, good flexibility and excellent chemical/thermal stability (Castro Neto et al., 2009; Sadasivuni et al., 2015; Wang et al., 2019). Graphene is extensively used in many electronic and optoelectronic device applications, which include field-effect transistors, energy storage devices like supercapacitors, flexible displays, sensors, photodetectors, and solar cells (Castro Neto et al., 2009; Bin Mohd Yusoff, 2015; Sadasivuni et al., 2015; Sang et al., 2019; Wang et al., 2019). Graphene is also an important material for transparent conductive electrodes. Graphene films can be grown by various methods including the chemical vapor deposition, pulsed laser deposition and electrochemical exfoliation of graphite.

Polymeric material has various characteristics such as easy processing, high-dielectric strength, light-weight, fracture tolerance, good chemical resistance and low manufacturing cost. PVA (Polyvinyl alcohol) is an easily produced polymer. PVA may be prepared by electro-spinning and sol-gel spin coating techniques. PVA has physicochemical properties, including good thermal stability, good flexibility, and good film forming (Finch, 1973; Ben Halima, 2016; Jafar Mazumder et al., 2019).

PVA has low electrical conductivity and becomes conductive with the addition of suitable dopant material (Bulinski, 2021). In addition, polymer-based dielectrics is often used to insulate electrical devices. Especially, dielectric polymers are preferred for charge-storage applications (Hashim, 2010). Pure polymers have generally a low dielectric constant. Polymer-based capacitors have important advantages like low dielectric loss, high breakdown strength, and easy production.

If a device is illuminated by light, the electron/hole pairs occur in depletion region (Wood, 1994). As light intensity increases, more carriers are formed in the depletion region. In other words, the number

*Corresponding Author, e-mail: dilan.savasturk@gazi.edu.tr

of these pairs is related to the photon energy. Also, the light-induced current is a result of the electron-hole pairs.

In this paper, we investigated illumination effect on electrical properties of the metal/polymer/semiconductor (MPS) device. The device was characterized under dark and 200 mW/cm^2 conditions. Admittance measurements (C and G) were also made at a constant frequency of 500 kHz. The device parameters were calculated for dark and illumination intensity.

2. MATERIAL AND METHOD

Boron-doped p-Si semiconductor wafer with 2-inch diameter, (100) orientation and 300 μm thickness was used as substrate. Before the Al/Gr-PVA/p-Si device were fabricated, Si was cleaned in an ultrasonic cleaner using chemical solvents. Detailed information about the formation of the Gr-PVP interlayer was given in the previous study (Ata et al., 2022).

The device was illuminated by a solar simulator (Newport/Oriel) with an AM 1.5G filter, which was only suitable for wavelengths between 400 and 700 nm. Admittance measurements of the device were made using HP 4192A at 500 kHz and under the dark and constant illumination conditions of 200 mW/cm^2. Both capacitance and conductance were also measured using an alternating signal with a voltage amplitude of 100 mV.

3. RESULTS AND DISCUSSION

The complex admittance, Y, of parallel circuit (parallel connected C and G) is defined as,

$$Y(\omega) = G_p(\omega) + i\omega C_p \tag{1}$$

here G_p and C_p are the parallel conductance and capacitance, respectively. Both depend on frequency. At the same time, the complex impedance Z is equal to $1/Y(\omega)$. Admittance spectroscopy is a powerful technique used to investigate electrical and dielectric characteristics and ac behavior of electronic devices. Capacitance-voltage (C-V) measurements are one of the most basic electrical measurements for electronic devices. A varying dc voltage and ac small signal voltage with $V(t)=V_0 \sin(\omega t)$ are applied across the device. The capacitance changes with frequency of the ac signal. At higher frequencies, the interface traps do not respond to ac signal and contribute to capacitance.

Figure 1 demonstrate the C-V plots. The measurements performed at a fixed frequency of 500 kHz showed that the capacitance value against the potential changes with increasing illumination intensity. When the illumination intensity per unit area is increased, capacitance values 'C' increases distinguishable. (Singh, 2003; Hashim, 2010; Tan et al., 2017; Tataroğlu et al., 2020; Buyukbas Ulusan et al., 2021; Al-Sehemi et al., 2022; Karataş & Yumuk, 2022).

These results confirm that the device exhibits photo-capacitive behavior, which is related to the photo-generated charges. The charge carriers are generated under illumination and accumulated at the interface. In addition, experimental measurements show that certain peaks for capacitance occur in the depletion region. These peaks are due to the distribution of deep traps in the band gap and interface states. As illumination intensity increases, the peak positions shift towards the lower voltages.

Figure 2 shows conductance-voltage (G/ω-V) plots as a function of applied voltage. Similarly, experimental results adapted to a fixed frequency value at 500 kHz show that the conductivity value measured against the potential also changes with increasing illumination intensity. In other words, The G/ω-V curve shows the conductance value rises with an increase in light intensity. The change in photo-conductance can be attributed to an increase in the number of photo-generated electrons with illumination intensity.
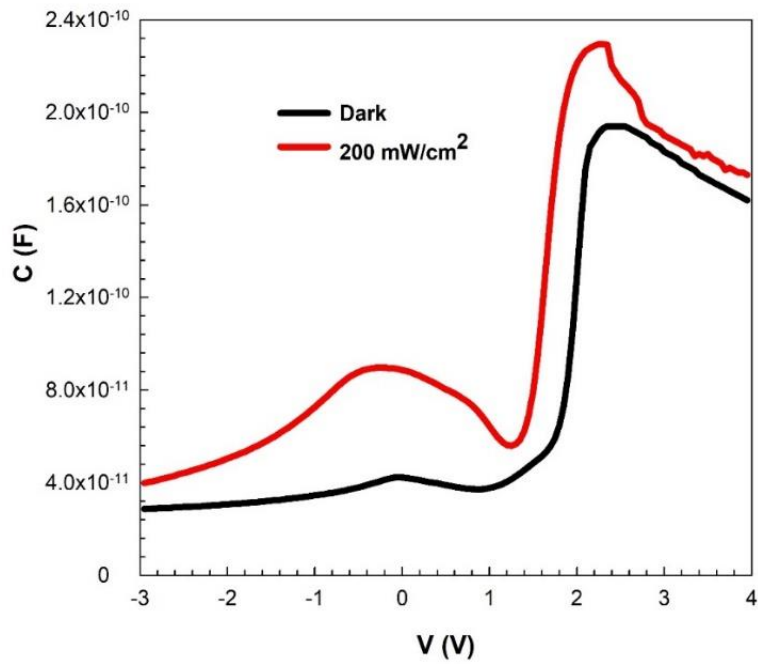
Figure 1. *C-V plots at 500 kHz*
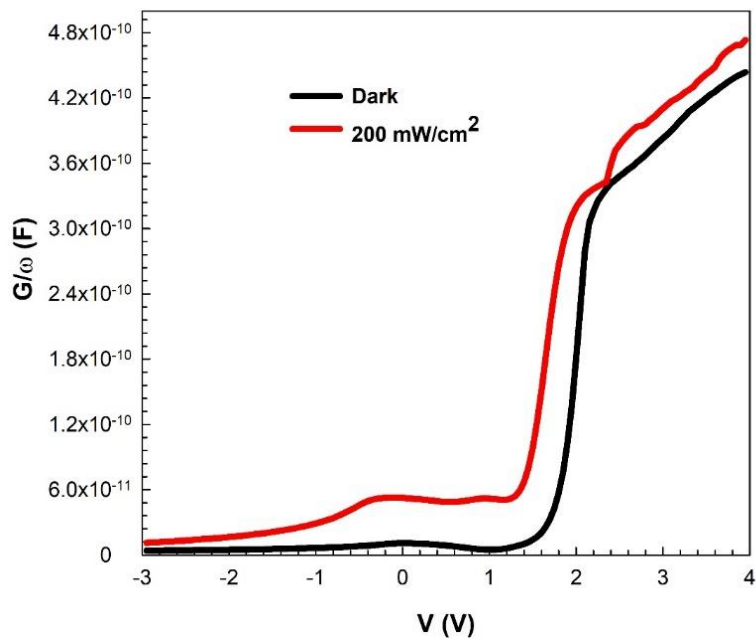
Figure 2. *G/ω-V plots at 500 kHz*

In practice, the admittance measurement is typically performed using an impedance analyzer, which is a specialized piece of test equipment that can measure the impedance of a circuit over a specific range of frequencies. The impedance measurement can then be converted to admittance, and the resistance can be calculated using the appropriate equations. Admittance measurements are used to calculate the resistance of a circuit in series. In a circuit with only resistive elements, the admittance is directly proportional to the conductance, which is the reciprocal of resistance. Hence, the resistance of a circuit can be calculated as the reciprocal of the conductance, which can be obtained from the admittance measurement.

All semiconductor devices contain series resistance parameter that affects their current-voltage (I-V) capacitance/conductance-voltage (C/G-V) characteristics and performance. Series resistance is mainly equal to the sum of the rectifier/ohmic contact resistances and the of the bulk resistance of semiconductor. The conductance method was used to extract series resistance (R_s) of the prepared device (Nicollian & Goetzberger, 1967). The R_s value was calculated using the following expression,

$$R_s = \frac{G_m}{G_m^2 + (\omega C_m)^2} \tag{2}$$

Series resistance was calculated from admittance measurements. Figure 3 demonstrates R_s-V plots. It is seen that the increase in illumination intensity causes an increase in the series resistance in depletion region. Besides, the R_s-V plots indicate a peak along depletion region. This peak comes from interface traps. This peak position shifts towards the lower positive voltage with illumination.
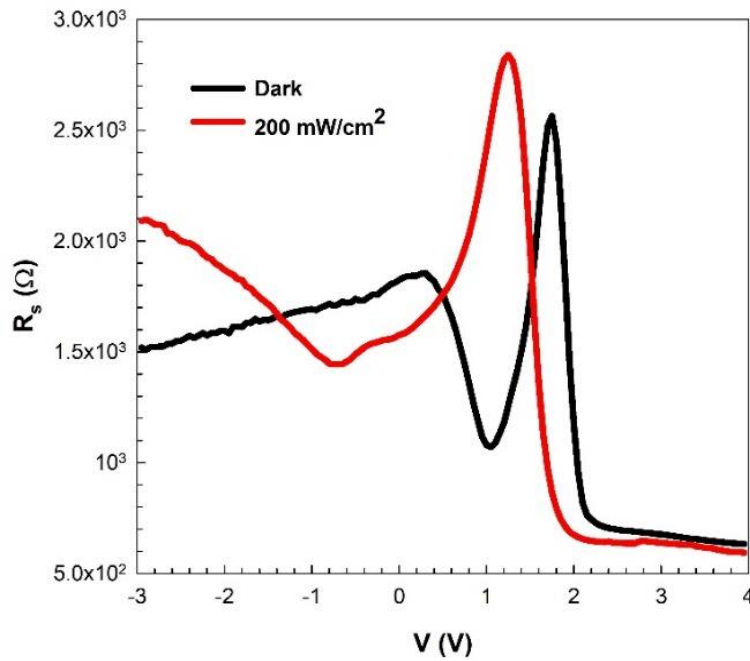
Figure 3. *R_s-V plots at 500 kHz*

The capacitance of depletion region of semiconductor devices is defined as: (Nicollian & Goetzberger, 1967; Sze, 1981; Nicollian & Brews, 1982; Tataroğlu & Altındal, 2006; Kim, 2016; Lambada et al., 2020),

$$C^{-2} = 2\,(V_0 + V)/(q\varepsilon_s\varepsilon_0 A^2 N_A) \tag{3}$$

The plot of C^{-2} versus V should yield a straight line. The diffusion potential ($V_D = V_0 + kT/q$) and acceptor concentration (N_A) can be derived from the intercept-slope of the straight line of C^{-2}-V plot. Here, E_F, E_m, $\Delta\Phi_B$ and W_D represent the Fermi energy level, the maximum electric field, the image force barrier lowering and the depletion-layer width, respectively. Their values were commonly calculated using the following equations,

$$E_F = \frac{kT}{q} ln\left(\frac{N_V}{N_A}\right) \tag{4}$$

$$E_m = \left[\frac{2qN_AV_0}{\varepsilon_s\varepsilon_0}\right]^{0.5} \tag{5}$$

$$\Delta\Phi_B = \left[\frac{qE_m}{4\pi\varepsilon_s\varepsilon_0}\right]^{0.5} \quad R_s = \frac{G_m}{G_m^2 + (\omega C_m)^2} \tag{6}$$

$$W_D = \sqrt{\frac{2\varepsilon_s\varepsilon_0 V_D}{qN_A}} \tag{7}$$

In addition, the barrier height Φ_B is given by,

$$\Phi_B = V_D + E_F - \Delta\Phi_B \tag{8}$$

Figure 4 shows C^{-2}-V plots of the device as a function of the reverse bias for dark and 200 mW/cm^2 conditions. The relationship between C^{-2} and V should be linear. It is clear that these plots indicate a straight line at a large reverse voltage. Also, it is observed that C^{-2} increases linearly with increase in the reverse applied voltage. The linearity of C^{-2}-V plots indicates that the interface states cannot follow the ac signal at 500 kHz.

The electrical parameters of the device extracted from Equations (4-8) have been given in Table 1. The Φ_B and W_D values under light are smaller than values in dark. The barrier height is affected by the distribution of charge at the depletion region. The device exhibits a photovoltaic behavior since the main electrical parameters are affected by illumination. The reason was attributed to the fact that the applied illumination generates more free carriers in the valance band, which absorb energy and easily jump to the conduction band under illumination conditions.
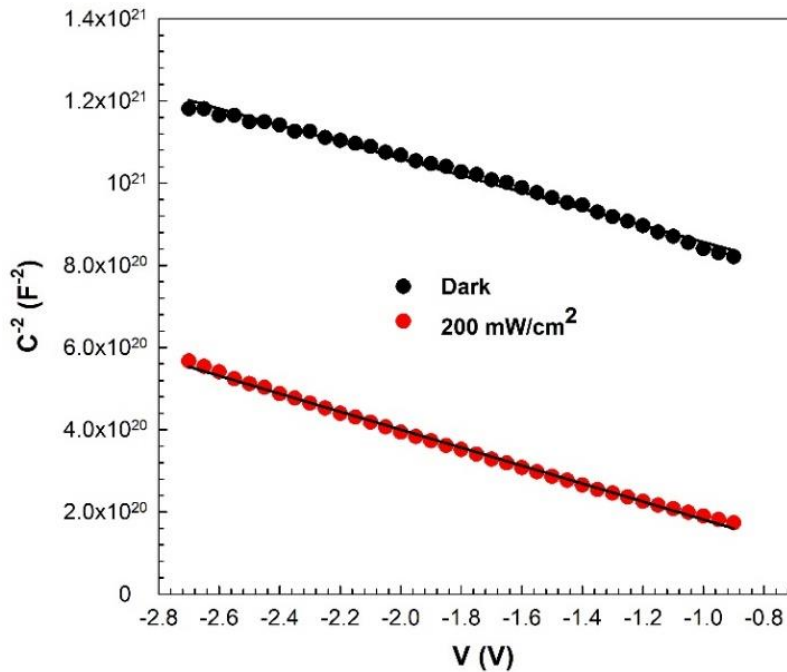
Figure 4. *C^{-2}-V plots at 500 kHz*

Table 1. *Some* electrical parameters *of the MPS structure*

P (mW/cm²)	V_D (eV)	N_A (cm⁻³)	E_F (eV)	E_m (V/cm)	$\Delta\Phi_B$ (eV)	Φ_B (eV)	W_D (cm)
0 (Dark)	0.644	9.35×10^{14}	0.274	1.33×10^4	$12.7.\times10^{-3}$	0.905	9.48×10^{-5}
200	0.356	8.88×10^{14}	0.275	0.95×10^4	10.8×10^{-3}	0.621	7.23×10^{-5}

The C-V measurements play an important role in the calculation of the interface state density (N_{ss}). The voltage dependence profile of illumination-induced surface states between organic interlayer and semiconductor was extracted based on high-low C-V method (Sze, 1981; Brews & Nicollian, 1984; Pandey & Kal, 1998). At high frequencies (f ≥ 500 kHz), charges at interface traps are unable to react to the exterior ac signal, and therefore they cannot supply an excess capacitance to the real value of it. At low frequencies, the interface traps can follow the ac signal, thus, they may contribute the measured capacitance value.

The interface state density across the band gap was calculated from the formula below using dark instead of low and illumination instead of high defined in the capacitance method.

$$N_{ss} = \frac{1}{qA}\left\{\left[\frac{1}{C_{dark}} - \frac{1}{C_i}\right]^{-1} - \left[\frac{1}{C_{ill}} - \frac{1}{C_i}\right]^{-1}\right\} \qquad (9)$$

In Equation 9, C_i and A are the interlayer capacitance and rectifier contact area, respectively. The N_{ss}-V plot is given in Figure 5. This plot shows two peaks. The first peak is related to the density distribution of the surface state and the second peak is the result of series resistance.
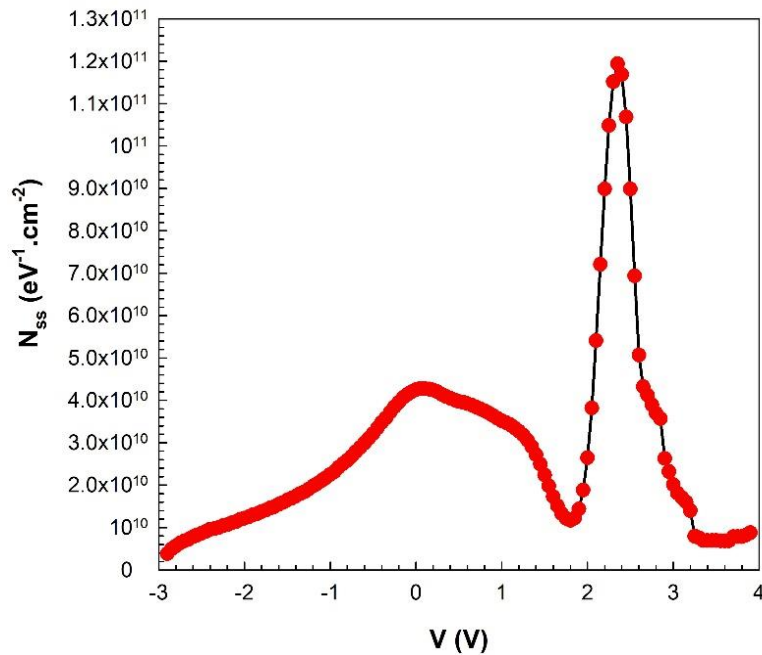
Figure 5. *Nss-V plot at 500 kHz*

4. CONCLUSION

This paper is concerned with the admittance measurements of the MPS structure under light illumination. These measurements were carried out at the constant frequency of 500 kHz under the dark and maximum constant illumination condition of 200 mW/cm^2.

The results showed that the MPS structure exhibited photo capacitive behavior. Some parameters, including N_A, E_F, Φ_B and W_D of the structure, were derived from the C^{-2}-V data. It was seen that these parameters were affected by the illumination. Besides, the N_{ss} versus V plot shows two distinctive peaks. These peaks indicate a special distribution of interface traps. In conclusion, the fabricated structure can serve as a photo capacitor in some specific optoelectronic applications.

CONFLICT OF INTEREST

The authors declare no conflict of interest.

REFERENCES

Ata, D., Altindal Yeriskin, S., Tataroglu, A., & Balbasi, M. (2022). Analysis of admittance measurements of Al/Gr-PVA/p-Si (MPS) structure. *Journal of Physics and Chemistry of Solids*, *169*, 110861. doi:10.1016/j.jpcs.2022.110861

Ben Halima, N. (2016). Poly(vinyl alcohol): review of its promising applications and insights into biodegradation. *RSC Advances*, *6*(46), 39823-39832. doi:10.1039/C6RA05742J

Bin Mohd Yusoff, A. R. (2015). *Graphene-based energy devices*. Wiley-VCH Verlag.

Brews, J. R., & Nicollian, E. H. (1984). Improved MOS capacitor measurements using the Q-C method, *Solid-State Electronics*, *27*(11), 963-975. doi:10.1016/0038-1101(84)90070-4

Bulinski, M. (2021). Metal doped PVA films for opto-electronics-optical and electronic properties, an overview. *Molecules*, *26*(10), 2886. doi:10.3390/molecules26102886

Buyukbas Ulusan, A., Tataroglu, A., Altindal, S., & Azizian-Kalandaragh, Y. (2021). Photoresponse characteristics of Au/(CoFe2O4-PVP)/n-Si/Au (MPS) diode. *Journal of Materials Science: Materials in Electronics*, *32*(12), 15732-15739. doi:10.1007/s10854-021-06124-w

Castro Neto, A. H., Guinea, F., Peres, N. M. R., Novoselov, K. S., & Geim, A. K. (2009). The electronic properties of graphene. *Reviews of Modern Physics*, *81*(1), 109-162. doi:10.1103/RevModPhys.81.109

Finch, C. A. (1973). *Polyvinyl alcohol: Properties and applications*. Wiley.

Hashim, A. A. (2010). *Polymer thin films*. InTech.

Jafar Mazumder, M. A., Sheardown, H., & Al-Ahmed, A. (Eds.). (2019). *Functional polymers*. Springer International Publishing.

Karataş, Ş., & Yumuk, M. (2022). Electrical characteristics of Al/(GO:PTCDA)/p-type Si structure under dark and light illumination: photovoltaic properties at 40 mW cm−2. *Journal of Materials Science: Materials in Electronics*, *33*(14), 10800-10813. doi:10.1007/s10854-022-08061-8

Kim, H. (2016). Capacitance-voltage (C-V) characteristics of Cu/n-type InP Schottky diodes. *Transactions on Electrical and Electronic Materials*, *17*(5), 293-296. doi:10.4313/TEEM.2016.17.5.293

Lambada, D. R., Yang, S., Wang, Y., Ji, P., Shafique, S., & Wang, F. (2020). Investigation of Illumination Effects on the Electrical Properties of Au/GO/p-InP Heterojunction with a Graphene Oxide Interlayer. *Nanomanufacturing and Metrology*, *3*(4), 269-281. doi:10.1007/s41871-020-00078-z

Nicollian, E. H., & Brews, J. R. (1982). *MOS physics and technology*. Wiley.

Nicollian, E. H., & Goetzberger, A. (1967). The Si-SiO2 Interface — Electrical Properties as Determined by the Metal-Insulator-Silicon Conductance Technique. *Bell System Technical Journal*, *46*(6), 1055-1133. doi:10.1002/j.1538-7305.1967.tb01727.x

Pandey, S., & Kal, S. (1998). A simple approach to the capacitance technique for determination of interface state density of a metal-semiconductor contact. *Solid-State Electronics*, *42*(6), 943-949. doi:10.1016/S0038-1101(97)00267-0

Sadasivuni, K. K., Ponnamma, D., Kim, J., & Thomas, S. (2015). *Graphene-based polymer nanocomposites in electronics.* Springer International Publishing.

Sang, M., Shin, J., Kim, K., & Yu, K. J. (2019). Electronic and thermal properties of graphene and recent advances in graphene based electronics applications. *Nanomaterials*, *9*(3), 374. doi:10.3390/nano9030374

Singh, J. (2003). *Electronic and optoelectronic properties of semiconductor structures.* Cambridge University Press.

Sze, S. M. (1981). *Physics of semiconductor devices.* Wiley.

Tan, S. O., Uslu Tecimer, H., Çiçek, O., Tecimer, H., & Altındal, Ş. (2017). Frequency dependent C–V and G/ω–V characteristics on the illumination-induced Au/ZnO/n-GaAs Schottky barrier diodes. *Journal of Materials Science: Materials in Electronics*, *28*(6), 4951-4957. doi:10.1007/s10854-016-6147-0

Tataroğlu, A., & Altındal, Ş. (2006). Characterization of current-voltage (I-V) and capacitance-voltage-frequency (C-V-f) features of Al/SiO2/p-Si (MIS) Schottky diodes. *Microelectronic Engineering*, *83*(3), 582–588. doi:10.1016/j.mee.2005.12.014

Tataroğlu, A., Altındal, Ş., & Azizian-Kalandaragh, Y. (2020). Electrical and photoresponse properties of CoSO4-PVP interlayer based MPS diodes. *Journal of Materials Science: Materials in Electronics*, *31*(14), 11665-11672. doi:10.1007/s10854-020-03718-8

Wang, J., Mu, X., & Sun, M. (2019). The thermal, electrical and thermoelectric properties of graphene nanomaterials. *Nanomaterials*, *9*(2), 218. doi:10.3390/nano9020218

Wood, D. (1994). *Optoelectronic semiconductor devices.* Prentice Hall.

Accuracy of In-Field and Out-Field Doses Calculated by Analytical Anisotropic and Pencil Beam Convolution Algorithms: A Dosimetric Study

Osman Vefa GÜL[1*] (iD)

[1]Selçuk Üniversitesi Tıp Fakültesi Radyasyon Onkolojisi A.D. Selçuklu/Konya Türkiye

Keywords	Abstract
In-Field Dose Out-of-Field Dose TLD	Out-of-field doses may affect the formation of secondary cancers, especially in radiosensitive organs, in patients treated with radiotherapy. The aim of this study is to investigate the in-field dose and out-of-field dose accuracy of Eclipse's analytic anisotropic algorithm (AAA) and pencil beam convolution (PBC) algorithms using TLDs. A tissue equivalent phantom containing a total of 21 measurement points at a depth of 5 cm from the anterior and posterior was created. Using Eclipse AAA and PBC algorithms in TPS, 100 MU for AP/PA fields and 95 cm source-skin distance (SSD) were planned. In-field measurement points including isocenter were 3, 5, 7 and 11 points for 3x3, 5x5, 7x7 and 10x10 cm2, respectively. Measuring points outside the field edge were 38, 36, 34 and 30 points for 3x3, 5x5, 7x7 and 10x10 cm2, respectively. In-field point dose values calculated by TPS for different fields were compared with TLD doses measured at the same location. The difference between in-field dose estimation and TLD measurements of both algorithms was generally below 1%. The difference between TPS and TLD was found to be 4.41% for the 10x10 cm2 irradiation field, due to the field edge at a distance of 5 cm from the isocenter. As the field size decreased, the out-of-field dose calculation performance of the AAA and PBC algorithms was adversely affected. For the 10x10 cm2 irradiation field, the TLD measurements and the out-of-field point dose difference of the PBC algorithm were found to be 39.40%. This difference was at most 12.06% for the AAA algorithm. The Eclipse TPS is good at calculating the in-field dose but underestimates the off-field dose. In out-of-field dose calculation, the AAA algorithm gives more accurate results than the PBC algorithm. Additionally, the smaller the field size, the worse the outfield dose accuracy. The use of in vivo dosimeters is recommended in order to estimate the out-of-field dose with great accuracy in radiotherapy.

1. INTRODUCTION

Cancer is one of the most serious health problems today. Many patients with cancer receive radiotherapy alone or simultaneously. The most important rule in radiotherapy is to ensure that the surrounding healthy tissue and risky organs receive the minimum dose while the tumor receives the maximum dose. In radiotherapy, patient treatment doses are calculated with treatment planning systems (TPS) that have the dosimetric information of the treatment devices loaded. As treatment techniques improve, the importance of computational algorithms increases. Treatment Planning Systems make dose calculations using different algorithms. These Algorithms are measurement-based, model-based or Monte Carlo based (Bosse et al., 2020). In measurement-based algorithms, using water phantom in treatment fields determined for reference conditions; percent deep dose, dose profile, and dose efficiency measurements are used (Abazarfard et al., 2021). In order to calculate the dose of TPS in radiotherapy, some measurements must be taken in the water phantom first. Percent deep dose and dose profile measurements need to be made for different fields and depths. Thanks to these measured data, TPS tries to accurately estimate the dose distribution in different depths and heterogeneous fields (DePew et al., 2018). Pencil Beam Convolution (PBC) creates the dose matrix by convolving the dose kernel with the

functions of the irregular areas. In the PBC algorithm, the pen beam kernel defines the dose distribution of the very fine beam entering the water equivalent medium. Pencil beam kernels are obtained by measuring central axis deep dose and beam off-axis ratio data. Anisotropic Analytical Algorithm (AAA) algorithm, a new photon dose calculation in Eclipse TPS started to be used. The AAA model provides fast and accurate dose calculation for photon beams, even in regions with complex tissue heterogeneities. Dose calculation algorithms include separate convolution patterns for primary photons, out-of-focus photons, contaminated electrons, and photons scattered from beam-limiting devices. Primary photons are photons emitted from a primary source, expressed as a point source located on the target surface. Out-of-focus photons are the photons scattered from the flattening filter and primary collimators. AAA also takes into account tissue heterogeneities and anisotropic 3D neighborhood of a radiation-matter interaction. Accurate modeling of out-of-field doses in radiotherapy is of great importance for clinical evaluation (Wang & Ding, 2014). During radiotherapy, areas outside the target volume are exposed to radiation due to scattered photons. Out-of-field doses may affect the formation of secondary cancers, especially in radiosensitive organs, in patients treated with radiotherapy (Bahreyni Toossi et al., 2018). Thyroid, breast, ovaries and lenses are among these radiosensitive organs. Although the level of radiation these organs are exposed to is low, it increases the risk of secondary cancer. It is important to determine the accuracy of the doses calculated by TPS algorithms in order to minimize the risk of secondary cancer. Doses taken out of the field by patients who are pregnant or with pacemakers are very important in clinical decisions. In-field dose success of radiotherapy TPS is high, but it cannot show this success in out-field dose calculation. Among the factors that negatively affect the failure of TPS in calculating the out-field dose are the sharp dose drop at the edge of the field and the formation of secondary radiation. Radiation therapy requires quality control at every stage. Some measurements need to be taken for the quality control of the plans prepared for the patients, the treatment planning system, and the treatment device. For this purpose, dosimetric equipment such as ion chambers of various volumes, thermoluminescent dosimeters (TLD), and film dosimeters are used. TLDs are used in clinics for purposes such as determining critical organ doses, investigating dose distribution in complex geometries, validating treatment planning, and controlling new treatment techniques in radiation therapy applications. Although the failure of TPS to calculate out-of-field dose is known, there are not enough studies in the literature (Shine et al., 2019). Howell et al. (2010) evaluated the out-of-field dose performance of the AAA algorithm with TLD in Eclipse TPS and found that the AAA algorithm underestimated over 40% of the out-of-field dose depending on the distance (Howell et al., 2010). Alghamdi and Tajaldeen (2019) evaluated the in-field and out-field dose calculation accuracy of five different algorithms for media with different densities. As a result of the measurements, they found that the AAA and PBC algorithms underestimated the out-of-field dose by 40% (Alghamdi & Tajaldeen, 2019).

This dosimetric study, it is aimed to compare the in-field and out-field dose calculation accuracy of AAA and PBC algorithms used by Eclipse TPS with TLD measurements.

2. MATERIAL AND METHOD

Phantom Irradiation

For the irradiated phantom setup, 9 pieces of 1cm thick and 1 piece 0.5cm thick RW3 (PTW, Freiburg, Germany) phantom of 40cm x 40cm dimensions were used. In addition, a 0.5 cm thick tissue equivalent bolus with adhesive properties was used. In our study, TLD-100 chips were used, and the effective atomic number is 8.14. TLD-100 chips do not produce artifacts as they are close to the human tissue effective atomic number of 7.42. TLD-100 chips were placed at the measurement points determined before Computed tomography (CT). Because TLDs are tissue equivalent, they became the reference for measurement points in the phantom. TLDs were placed 1 cm apart in the bolus to determine measurement points. The preliminary steps for preparing the measurement phantom are shown in Figure 1. The anterior and posterior depth of TLDs was 5 cm. Computed tomography (CT) images of the created phantom were obtained on the Toshiba Aquilion CT device with a slice thickness of 1 mm, and then TPS was transferred. Necessary dosimetric measurements were made before the treatment. The difference between the measurements obtained and the acceptance tests of the linear accelerator was found to be within 1%.
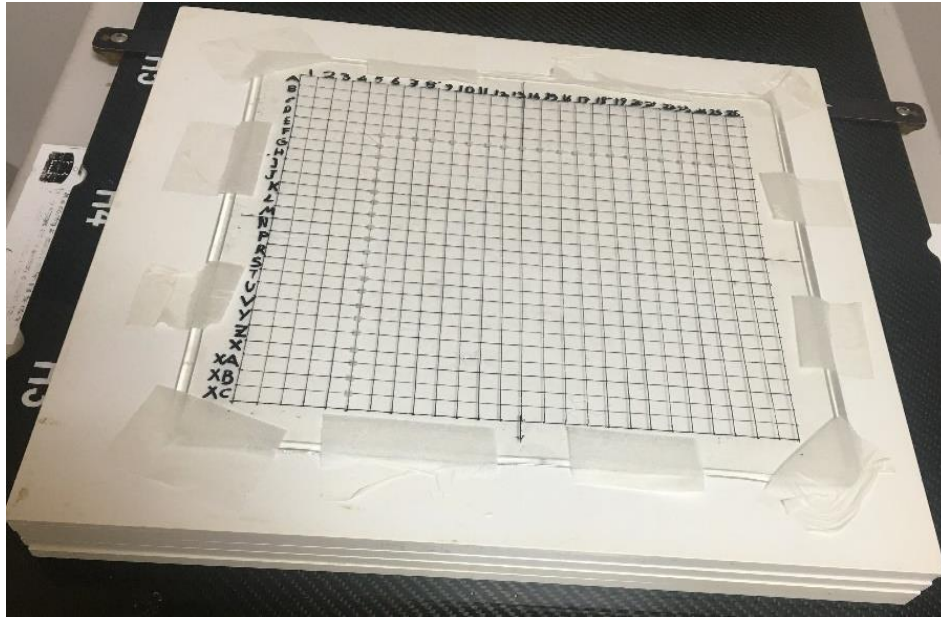
Figure 1. Preliminary steps to prepare the measurement phantom

Treatment Planning

For all irradiation fields, the isocenter point was set to 5 cm for anterior and posterior depths and the source-skin distance (SSD) was set to 95 cm. The irradiation setup is shown in Figure 2. The irradiation was carried out in the Varian DHX linear accelerator device with 80 multileaf collimators (MLC) at 6 MV photon energy. X-ray was applied at 300 MU/min. In the AAA and PBC algorithms, dose calculations were made with a 2 mm grid size. In TPS, plans were made to irradiate 100 MU from AP and PA to different open fields using Eclipse AAA and PBC algorithms. These open fields were 3x3, 5x5, 7x7 and 10x10 cm^2. In-field measurement points including isocenter were 3, 5, 7 and 11 points for 3x3, 5x5, 7x7 and 10x10 cm^2, respectively. Measuring points outside the field edge were 38, 36, 34 and 30 points for 3x3, 5x5, 7x7 and 10x10 cm^2, respectively. In-field and out-of-field doses calculated in both algorithms were measured on the x and y axes, then averaged for each axis.
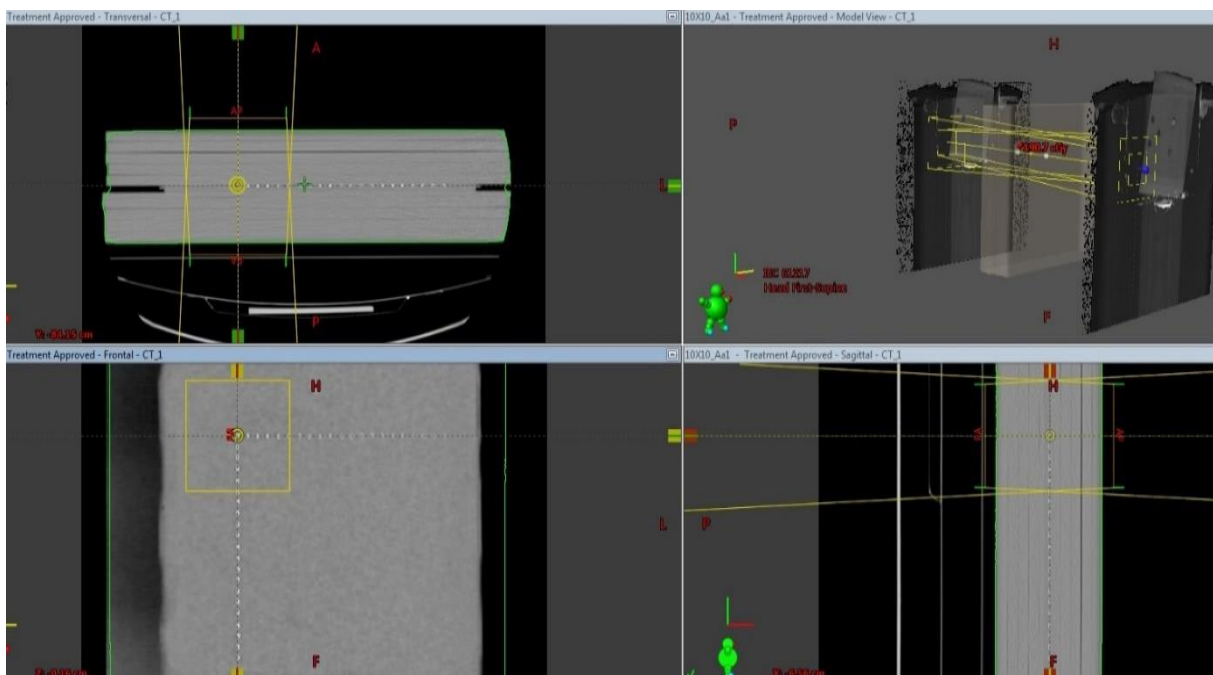
Figure 2. Measuring points and irradiation set-up in the phantom

Calibration of TLDs

TLD, which can measure independently of many factors, is accepted as the most suitable in-vivo dosimetry system. In this study, 3.2 mm x 3.2 mm x 0.9 mm chip-shaped TLD-100 dosimeters obtained by doping natural lithium fluoride (LiF) with Mg and Ti were used. 150 TLD-100 chips were used for TLD calibration. TLD-100 chips were baked in TLD oven for 1 hour at 400°C and 2 hours at 100°C. All TLDs were exposed to a dose of 1 Gy in a Varian DHX linear accelerator device at a depth of 1.5 cm with 6 MV photon energy in a $10x10$ cm^2 field. 96 TLDs with irradiation reproducibility within 1% were selected for the study. The reader calibration factor (RCF), which is the conversion coefficient to be used to convert the phototube current in microcoulomb (µC) taken from the reader to the absorbed radiation dose, was determined. In order to ensure that the reading values of the selected TLD chips have similar sensitivity, a weighting factor called the element correction factor (ECC) specific to each chip was determined. Since the determined ECC factors are specific to each chip, the chips are named to avoid confusion.

In-Field Dose Measurement with TLDs

Point doses calculated in TPS and measured by TLDs were compared for each field. After each TLD was individually packaged, it was placed at the measuring points. Measurements were repeated 3 times for each point determined before CT. 2 TLDs were placed at each measurement point to minimize the error. In-field dose measurement was performed at 3, 5, 7 and 11 measurement points for 3x3, 5x5, 7x7 and 10x10 cm2, respectively. A preliminary read annealing for irradiated TLD chips was performed at 100ºC for 10 minutes. Doses were measured with TLDs for each area and point. The mean and standard deviation of the measured doses were calculated.

Out-of-Field Dose Measurement with TLDs

Dose measurement points were determined starting at a distance of 1 cm from the field edge. The number of these measurement points was 38, 36, 34 and 30 for 3x3, 5x5, 7x7 and $10x10$ cm^2 irradiation fields, respectively. Dose measurement with TLDs was repeated 3 times for each field. Pre-reading annealing process was applied to read TLDs exposed to radiation. The point doses measured by TLDs and calculated by TPS were compared for different irradiation fields.

Statistical Analysis

In the current study, percentage differences between TPS and TLD doses were evaluated. Analysis of AAA, PBC and TLD doses was performed using Paired Sample t-test.

3. RESULTS AND DISCUSSION

The mean dose differences (%) between in-field doses measured by TLD and calculated by AAA and PBC algorithms are shown in Table 1. For the $3x3cm^2$ irradiation field, TLD measurements at the isocenter point and the in-field dose difference calculated by TPS were -0.24% and -0.34% for the AAA and PBC algorithms, respectively. For the $3x3cm^2$ irradiation field, no significant difference was found between AAA and PBC algorithms for isocenter point doses (p=0.072). For the 5x5 cm^2 irradiation field, point dose measurements on the x and y axes at 1 and 2 cm distance from the isocenter were taken separately and then the average was calculated. Accordingly, the difference between in-field point doses calculated by the AAA and PBC algorithms and measured by TLD was less than 0.75%. For the $7x7cm^2$ irradiation field, the difference between TLD measurement and point doses calculated by AAA and PBC algorithms was less than 0.7%. For a 10x10 cm^2 irradiation field, the point dose difference between TLD and TPS up to 4 cm distance is approximately 1%. However, due to the edge of the field at a distance of 5 cm, in-field dose measurement by TLD and calculated by TPS increased to 4.41%. For the 10x10 cm^2 irradiation field, a significant difference was found between the point doses calculated by the AAA and PBC algorithms at a distance of 5 cm (p=0.00). The in-field dose distribution measured by TLD and calculated by TPSs is shown in Figure 3. The mean dose differences (%) between out-field doses measured by TLD and calculated by AAA and PBC algorithms are given in Table 2. For the $3x3cm^2$ irradiation field, TLDs could measure the dose up to 19 cm outside the field, while the TPS was able to calculate up to 8 cm. As the field size decreased, the out-of-field dose calculation performance of the AAA and PBC algorithms was adversely affected. For the 10x10 cm2 irradiation field, the
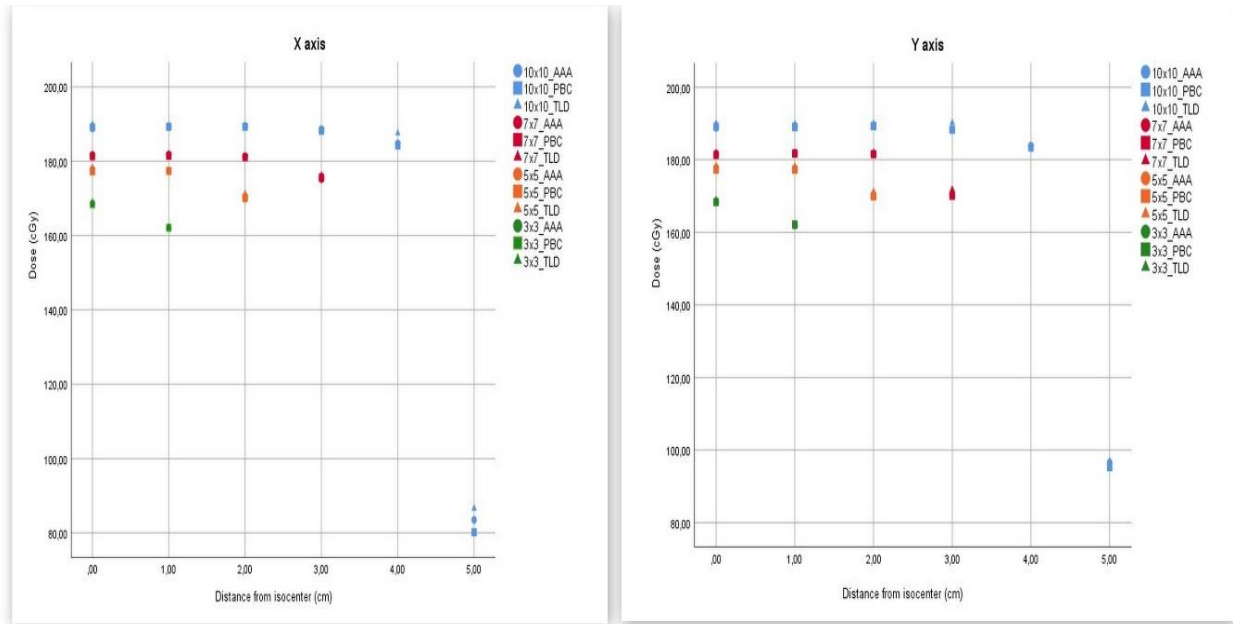
TLD measurements and the out-of-field point dose difference of the PBC algorithm were found to be 39.40%. This difference was at most 12.06% for the AAA algorithm. For all irradiation fields, the AAA algorithm was able to measure the dose at a distance of 12 cm from the edge of the field. The farthest distance that the PBC algorithm could measure was 15 cm. The out-of-field dose distribution measured by TLD and calculated by TPSs is shown in Figure 4. Although radiation was measured with TLD at different distances from the edge of the field, it was observed that the out-of-field dose calculation capability of both algorithms was limited.

Table 1. *Mean dose differences (%) between in-field doses measured by TLD and calculated by AAA and PBC algorithms*

	Field Size (cm²)											
	3 X 3			5 X 5			7 X 7			10 X 10		
Meas. points	AAA (%)	PBC (%)	TLD Mean ± SD (cGy)	AAA (%)	PBC (%)	TLD Mean ± SD (cGy)	AAA (%)	PBC (%)	TLD Mean ± SD (cGy)	AAA (%)	PBC (%)	TLD Mean ± SD (cGy)
Iso.	-0.25	-0.34	168.92±0.26	-0.28	-0.56	178.25±0.39	-0.09	-0.29	181.82±0.10	-0.54	-0.38	189.88±0.57
1	-0.17	-0.06	162.22±0.24	-0.23	-0.27	177.80±0.55	-0.05	-0.18	181.90±0.48	-0.26	-0.32	189.74±0.60
2	-	-	-	-0.73	-0.67	171.18±0.41	+0.03	-0.06	181.41±0.65	-0.19	-0.24	189.73±0.52
3	-	-	-	-	-	-	-0.68	-0.65	173.98±2.33	-0.44	-0.59	189.33±0.93
4	-	-	-	-	-	-	-	-	-	-0.72	-1.02	185.66±1.99
5	-	-	-	-	-	-	-	-	-	-1.90	-4.41	91.76±5.37

Table 2. *Mean dose differences (%) between out-field doses measured by TLD and calculated by AAA and PBC algorithms*

	Field Size (cm²)											
	3 X 3			5 X 5			7 X 7			10 X 10		
Meas. points	AAA (%)	PBC (%)	TLD Mean ± SD (cGy)	AAA (%)	PBC (%)	TLD Mean ± SD (cGy)	AAA (%)	PBC (%)	TLD Mean ± SD (cGy)	AAA (%)	PBC (%)	TLD Mean ± SD (cGy)
1	-4.12	-3.49	5.53±0.85	-7.37	-6.18	7.63±0.41	-11.67	-15.19	10.78±0.56	-4.51	-8.76	11.75±0.86
2	-35.09	-34.57	4.02±0.07	-14.81	-13.85	5.18±0.20	+2.13	-5.79	6.47±0.43	-2.15	-31.68	7.89±0.19
3	-63.47	-62.62	3.31±0.08	-25.72	-25.13	3.58±0.15	-4.62	-5.04	4.76±0.16	+6.07	-34.90	5.10±0.70
4	-67.00	-67.29	2.46±0.04	-39.08	-38.56	3.06±0.10	-11.07	-14.50	3.44±0.30	-4.98	-39.40	4.01±0.46
5	-57.09	-58.29	1.41±0.07	-39.43	-41.13	2.12±0.14	-1.34	-6.63	2.23±0.17	+1.10	-30.99	2.71±0.56
6	-62.64	-62.60	1.08±0.07	-40.26	-45.14	1.50±0.18	-9.13	-10.68	1.74±0.17	-1.93	-23.86	2.02±0.33
7	-61.92	-62.48	0.67±0.13	-21.11	-30.83	0.90±0.05	-17.47	-28.88	1.34±0.41	-1.32	-30.56	1.59±0.16
8	-82.12	-81.76	0.56±0.02	-34.23	-42.20	0.78±0.02	-10.02	-14.04	0.89±0.02	+9.36	-17.38	1.11±0.24
9	-	-	0.49±0.01	-31.06	-32.06	0.59±0.01	-10.19	-4.32	0.67±0.04	+8.09	-2.38	0.84±0.05
10	-	-	0.37±0.03	-33.68	-35.87	0.47±0.01	-13.65	-13.27	0.58±0.03	-3.92	-16.45	0.79±0.03
11	-	-	0.30±0.01	-49.25	-48.88	0.40±0.01	-9.09	-7.49	0.44±0.02	-4.03	-3.22	0.62±0.02
12	-	-	0.26±0.02	-49.05	-48.87	0.39±0.01	-28.48	-3.78	0.42±0.02	-12.06	-12.24	0.58±0.02
13	-	-	0.24±0.01	-	-	0.31±0.01	-	-38.05	0.34±0.03	-	-11.59	0.44±0.03
14	-	-	0.21±0.01	-	-	0.26±0.02	-	-38.81	0.32±0.03	-	-6.90	0.42±0.02
15	-	-	0.18±0.01	-	-	0.21±0.01	-	-32.48	0.29±0.02	-	-4.87	0.41±0.02
16	-	-	0.16±0.01	-	-	0.20±0.01	-	-	0.22±0.02	-	-	-
17	-	-	0.14±0.01	-	-	0.18±0.01	-	-	0.19±0.01	-	-	-
18	-	-	0.12±0.01	-	-	0.16±0.01	-	-	-	-	-	-
19	-	-	0.12±0.02	-	-	-	-	-	-	-	-	-

Figure 3. *In-field point dose distribution measured by TLD
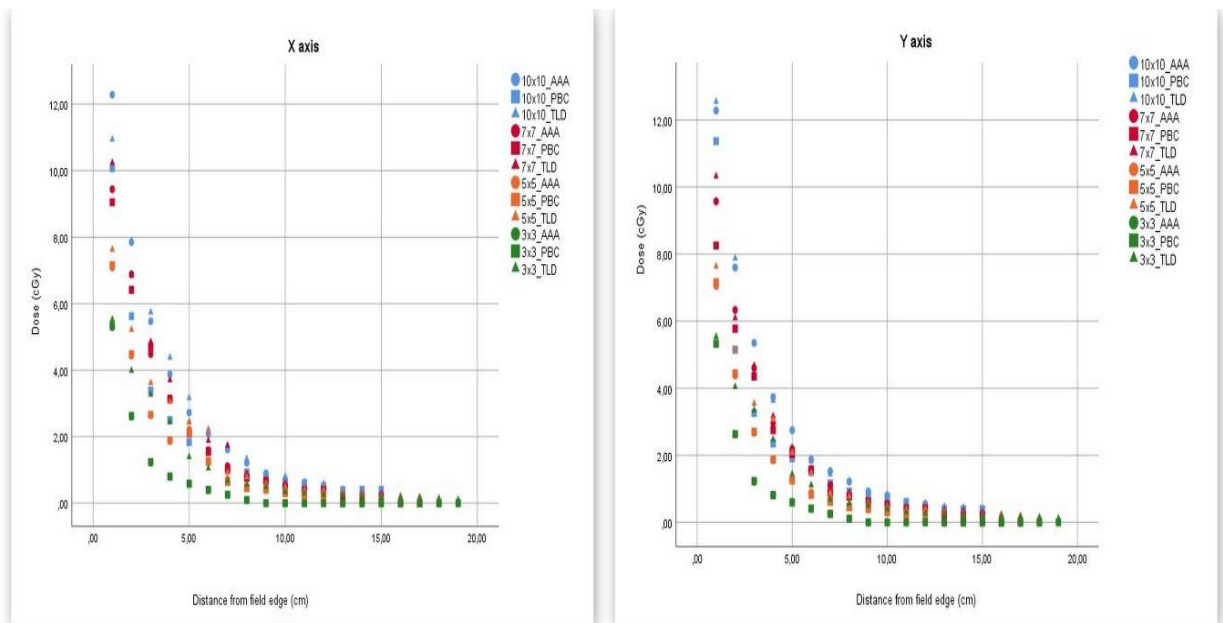and calculated by AAA and PBC algorithms*

Figure 4. *Out-of-field point dose distribution measured by TLD
and calculated with AAA and PBC algorithms*

In this dosimetric study, we examined the accuracy of in-field and out-field doses calculated by Eclipse AAA and PBC algorithms for different fields. Two different algorithms gave similar results with TLD measurements for in-field dose calculation. Out-of-field doses may affect the formation of secondary cancers, especially in radiosensitive organs, in patients treated with radiotherapy. Accurate estimation of out-of-field doses in radiotherapy is important to minimize the risk of secondary cancer. The results show that the AAA and PBC algorithms underestimate out-of-field doses when compared with TLD measurements. The AAA algorithm calculates the out-of-field dose calculation with less error than the PBC algorithm, but it is not sufficient. For the $10 \times 10 cm^2$ irradiation area, the PBC algorithm and the AAA algorithm underestimate 40% and 12.06%, respectively. These underestimation rates increase as the irradiation field size decreases.

Howell et al. (2010) aimed to measure the accuracy of the out-field dose estimated by the AAA algorithm for a given clinical treatment in the Varian Clinac 2100. They compared doses calculated in TPS and measured by TLD for 238 points. They emphasized that the AAA algorithm could underestimate out-of-field doses by 40% (Howell et al., 2010). In our current study, we found that the AAA algorithm erroneously predicted the dose for 10x10, 7x7, 5x5 and 3x3 cm^2, approximately 12%, 28%, 48%, and 82%, respectively.

Huang et al. (2013) evaluated the accuracy of Pinnacle3 TPS out-field dose calculations for IMRT treatment plans with Anthropomorphic phantom and TLDs. They stated that accurate dose estimation of TPS is inversely proportional to distance. They emphasized that for the three IMRT treatment plans studied, TPS underestimated the dose by an average of 50% (Huang et al., 2013). In the IMRT treatment technique, each field is divided into small sub-fields. The out-of-field dose estimation results of TPS in our study were similar to those of Huang et al. (2013). In our study, it was found that for the 5x5cm^2 irradiation field, TPS underestimated approximately 49% at a distance of 12 cm from the edge of the field. For the 3x3 irradiation field, the TPS at 8 cm distance underestimates approximately 80%.

Bahreyni Toossi et al. (2018) examined the extra-field dose at different distances in breast irradiation. They found that TPS underestimated the dose by 39%, especially at the edge of the field and at long distances (Bahreyni Toossi et al., 2018). Our research was conducted by Bahreyni Toossi et al. (2018), gave parallel results. It has been observed that TPS underestimates dose for different fields. For the 10x10 irradiation field, the dose underestimated by TPS was approximately 12% and 39% for the AAA and PBC algorithms, respectively.

Sánchez-Nieto et al. (2020) investigated the accuracy of doses estimated by TPS for 10x10 cm^2 field with 6 MV photon energy in Elekta Axesse linear accelerator using dosimetric methods. They stated that TPS was successful in the field, but underestimated by about 13% outside the field edge (Sánchez-Nieto et al., 2020). In our study, both algorithms were found to be successful in calculating in-field dose, but it was seen that they greatly underestimated the out-of-field dose depending on the field size.

Acun-Bucht et al. (2018) aimed to examine the validation of doses calculated by TPS using ion chambers and TLDs. They measured doses of off-axis points 2 cm and 4 cm from the isocenter with TLDs. Acun-Bucht et al. (2018) found the difference between TPS and TLD doses at 2cm and 4cm distance from the isocenter of approximately 3% and 4%, respectively (Acun-Bucht et al., 2018). In our current study, the difference between TLD and TPS doses for 2 cm and 4 cm distances from the isocenter is less than 1%.

Alghamdi and Tajaldeen (2019) evaluated the in-field and out-field dose calculation accuracy of five different algorithms for media with different densities. According to the results of measurements made in water density, the in-field dose difference was 0.39% and 0.43% for the AAA and PBC algorithms, respectively. In addition, as a result of the measurements, they found that the AAA and PBC algorithms underestimated the out-of-field dose by 40% (Alghamdi & Tajaldeen, 2019). In our study, the intra-field dose difference calculated by TLD measurements and TPS was less than 1%. For 10x10 cm2, it was seen that the PBC algorithm underestimated the out-of-field dose by approximately 39%. This rate was approximately 12% for the AAA algorithm.

Gul et al. (2021) investigated the out-of-field fetal dose of a patient who received breast radiotherapy in the first 3 months of pregnancy using a human equivalent phantom. The fetal dose at a distance of 25.84 cm from the lower limit of the target volume was calculated as 0 cGy in the AAA algorithm. TLD measurements ranged between 3-16 cGy. In our current study, in parallel with Gul et al. (2021), AAA and PBC algorithms were found to be insufficient in calculating out-of-field dose at a distance of 19 cm from the edge of the field.

4. CONCLUSION

In this study, we investigated the in-field dose and out-of-field dose accuracy of Eclipse TPS using TLDs. The Eclipse TPS is good at calculating the in-field dose, but underestimates the off-field dose. In out-of-field dose calculation, the AAA algorithm gives more accurate results than the PBC algorithm. Additionally, the smaller the field size, the worse the outfield dose accuracy. Out-of-field doses may affect the occurrence of secondary cancer, especially in radiosensitive organs, in patients receiving radiotherapy. In order to minimize the risk of secondary cancer, it is important to determine the accuracy of the in-field and out-field doses calculated with

TPS algorithms. Out-field doses taken by pregnant patients or patients with pacemakers are crucial in clinical decisions. The use of in vivo dosimetry is recommended for accurate determination of out-of-field dose in radiotherapy of patients who are pregnant or have pacemakers.

CONFLICT OF INTEREST

There is no conflict of interest.

REFERENCES

Abazarfard, M., Azadeh, P., & Mostaar, A. (2021). Dose calculation accuracy for photon small fields in treatment planning systems with comparison by Monte Carlo simulations. *Polish Journal of Medical Physics and Engineering*, *27*(3), 181-190. doi:10.2478/pjmpe-2021-0022

Acun-Bucht, H., Tuncay, E., Darendeliler, E., & Kemikler, G. (2018) Absolute dose verification of static intensity modulated radiation therapy (IMRT) with ion chambers of various volumes and TLD detectors. *Reports of Practical Oncology & Radiotherapy*, *23*(4), 242-250. doi:10.1016/j.rpor.2018.04.001

Alghamdi, S., & Tajaldeen, A. (2019). Evaluation of dose calculation algorithms using different density materials for in-field and out-of-field conditions. *Experimental Oncology*, *41*(1), 46-52. doi:10.32471/exp-oncology.2312-8852.vol-41-no-1.12529

Bahreyni Toossi, M. T., Soleymanifard, S., Farhood, B., Mohebbi, S., & Davenport, D. (2018). Assessment of accuracy of out-of-field dose calculations by TiGRT treatment planning system in radiotherapy. *Journal of Cancer Research and Therapeutics*, *14*(3), 634-639. doi:10.4103/0973-1482.176423

Bosse, C., Narayanasamy, G., Saenz, D., Myers, P., Kirby, N., Rasmussen, K., Mavroidis, P., Papanikolaou, N., & Stathakis, S. (2020). Dose Calculation Comparisons between Three Modern Treatment Planning Systems. *Journal of Medical Physics*, *45*(3), 143-147. doi:10.4103/jmp.jmp_111_19

DePew, K. D., Ahmad, S., & Jin, H. (2018). Experimental Assessment of Proton Dose Calculation Accuracy in Small-Field Delivery Using a Mevion S250 Proton Therapy System. *Journal of Medical Physics*, *43*(4), 221-229. doi:10.4103/jmp.jmp_33_18

Gul, O. V., Inan, G., & Basaran, H. (2021). Dosimetric comparison of different radiotherapy techniques to determine the absorbed fetal dose in pregnant patients with left-sided breast cancer. *Arab Journal of Nuclear Sciences and Applications*, *54*(4), 94-101. doi:10.21608/ajnsa.2021.69536.1456

Howell, R. M., Scarboro, S. B., Kry, S. F., & Yaldo, D. Z. (2010). Accuracy of out-of-field dose calculations by a commercial treatment planning system. *Physics in Medicine & Biology*, *55*(23), 6999-7008. doi:10.1088/0031-9155/55/23/S03

Huang, J. Y., Followill, D. S., Wang, X. A., & Kry, S. F. (2013). Accuracy and sources of error of out-of field dose calculations by a commercial treatment planning system for intensity-modulated radiation therapy treatments. *Journal of Applied Clinical Medical Physics*, *14*(2), 186-197. doi:10.1120/jacmp.v14i2.4139

Sánchez-Nieto, B., Medina-Ascanio, K. N., Rodríguez-Mongua, J. L., Doerner, E., & Espinoza, I. (2020). Study of out-of-field dose in photon radiotherapy: A commercial treatment planning system versus measurements and Monte Carlo simulations. *Medical Physics*, *47*(9), 4616-4625. doi:10.1002/mp.14356

Shine, N. S., Paramu, R., Gopinath, M., Jaon Bos, R. C., & Jayadevan, P. M. (2019). Out-of-Field Dose Calculation by a Commercial Treatment Planning System and Comparison by Monte Carlo Simulation for Varian TrueBeam®. *Journal of Medical Physics*, *44*(3),156-175. doi:10.4103/jmp.jmp_82_18

Wang, L., & Ding G. X. (2014). The accuracy of the out-of-field dose calculations using a model-based algorithm in a commercial treatment planning system. *Physics in Medicine & Biology*, *59*(13), N113-28. doi:10.1088/0031-9155/59/13/n113

A study of Proton Radiation Effects on a Silicon Based Solar Cell

Damla Gül KELEŞ[1] (iD) Hande KARADENİZ[1*] (iD) Serdar KARADENİZ[1] (iD)

[1]*Giresun University, Faculty of Engineering, Department of Energy Systems Engineering, Giresun, Türkiye*

Keywords	Abstract
Photovoltaic Cell Electrical Parameters Proton Irradiation SRIM	In this study, the changes in the performance parameters of silicon photovoltaic cells were investigated before and after irradiation. For this aim, the current-voltage and power-voltage characteristics of structures were obtained before and after irradiation. The electrical parameters were determined using obtained characteristics. High energetic (24.5 MeV) proton beam was used as the radiation source. In addition, radiation-induced displacement damages were determined using SRIM/TRIM simulations, and the effect of these damages on the photovoltaic cell was investigated. This study, which depends on the radiation hardness as a result of irradiation with protons, was important. Because the displacement damage caused changes on the electrical properties of device. This behavior was attributed to the defects generated by proton irradiation. On the other hand, it was seen that proton irradiation can be a tool for controlling the material and cell properties.

1. INTRODUCTION

Photovoltaic power systems have been known for many years as a source that produces the electricity with solar effect. Photovoltaic cells are widely used in energy systems due to reasons such as efficiency. It is important to examine the conditions that can affect the performance of photovoltaic devices under different conditions in converting light energy to electrical energy. Especially, the performance of a photovoltaic cell plays an important role in space applications such as satellite technology (Tada et al., 1982; Alurralde et al., 2004; Miyazawa et al., 2018). Monocrystalline silicon solar cells are not only the most complex, but they are generally used in near-earth satellites because of their low expense and lightweight material. However, as a continuous power supply, solar cells and other optoelectronic components of satellites are irradiated by charged particles such as protons and electrons within Earth's radiation belts. Defective fields are formed due to displacement damage caused by space particles penetrating solar cells. They cause some changes in the performance of the devices due to the damage caused (Song et al., 2022). These variations are seen in some common performance parameters such as fill factor, open circuit voltage and short circuit current. The change in the parameters of photovoltaic cells affects the efficiency, optimum current and voltage parameters. A brief inspection of radiation-induced damage of photovoltaic cells has been studied for space applications (Raya-Armenta et al., 2021). In addition, different studies have been carried out for photovoltaic devices (Wang et al., 2017; Hadjdida et al., 2018; Yu et al., 2021; Liu et al., 2022).

The problem of radiation damage arises with the introduction of solar cell power systems into satellites. A solar cell on a satellite is bombarded by these particles due to the high-energy activity of an electron and proton trapped in the earth's electromagnetic field. The reason of the distorting effect of radiation on materials and devices are the particles such as electrons, neutrons, protons and ions. The source of these particles can be particle accelerators, natural space radiation, nuclear reactions, radioactive sources or

electrons that produced by gamma rays. These particles can interact with materials in a variety of ways because of their mass, energy and charge. When the application areas of particle accelerators are examined, especially discovery of the atomic nucleus, its importance is understood with the continuation of its development in the fields of science and technology. In our country, many activities have been carried out within the scope of accelerator technology, and studies that contribute to its development are still continuing (Sultansoy, 1993; Adıgüzel et al., 2023). Researches have also been conducted to test various radiation applications such as materials, detectors and other electronic devices interacting with protons (Bilge Demirkoz et al., 2020).

In this study, the characteristics of performance parameters of photovoltaic devices have been investigated before and after proton irradiation. The variation in the electrical properties of silicon cells irradiated with protons has been investigated, and information about their performances has been provided. Moreover, the effects of radiation-induced degradation on cell performance have been analyzed using the SRIM/TRIM simulation program.

2. MATERIAL AND METHOD

The Si based polycrystalline solar cells with effective area of 12.5 cm x 12.5 cm used in this study were purchased from Shenzhen Topsky Energy Co., Ltd. A polycrystalline p-type silicon was used in the solar cell. The back and front contacts are made of aluminum (Al) and silver (Ag), respectively. The detailed characteristics of the solar cell are listed in Table 1. The electrical properties of polycrystalline silicon cell have investigated before being exposed to radiation. First, current, voltage and power parameters of the polycrystalline silicon cell have measured under AM0 (136,6 mW/cm^2 at 25°C) solar spectrum condition using Sciencetech Solar Simulator and computer controlled Keithley 2400 SourceMeter device. The schematic illustration of measurement setup is displayed in Figure 1. Current-voltage (I-V) and power-voltage (P-V) curves have drawn with the data obtained as a result of these measurements. Then, the same polycrystalline silicon cell has exposed to proton irradiation at the Proton Accelerator Facility, and the electrical properties have examined again. During the irradiation, the used proton energy and total number of ions are 24.5 MeV and 1x10^6 cm^{-2}, respectively. The angle of the proton beam on the cell is 90 degrees, and the total irradiation time is 12 seconds. The irradiation process was performed at room temperature and in an atmospheric environment. As a result of these processes, the changes before and after radiation of the polycrystalline silicon cell have compared. SRIM/TRIM simulation has performed to investigate of proton-induced displacement damage on device performance.
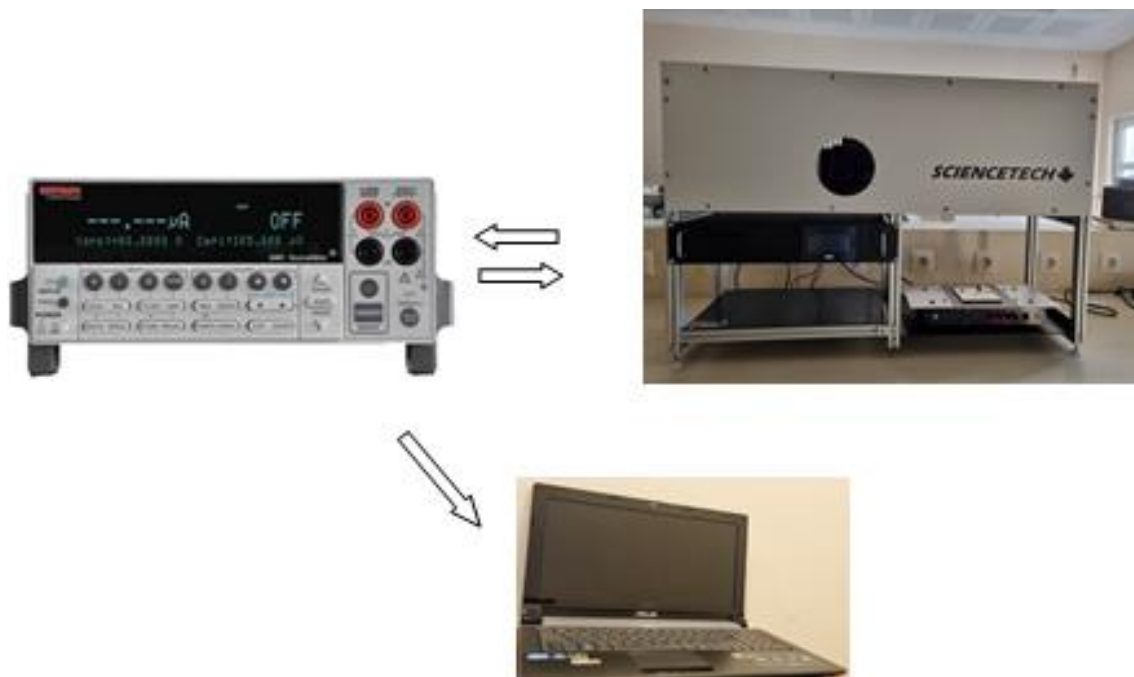

Figure 1. Schematic illustration of measurement setup

Table 1. *Characteristics of silicon photovoltaic cell*

Dopant element	Boron
Process of surface pyramid	Texture
Anti-reflection coating material	Hydrogenated silicon nitride (SiN$_x$:H)
Production process of anti-reflection coating	Plasma Enhanced Chemical Vapor Deposition (PECVD)

3. RESULTS AND DISCUSSION

Figures 2a and 3a depict the I-V and P-V plots before irradiation of the silicon cell. The short-circuit current (I_{sc}) of a solar cell is measured when the output is zero or short-circuited. At a given light intensity, the value of the output current (I) is given as follows, and it represents the distribution capacity of a solar cell.

$$I = I_{sc} = I_{photon} \tag{1}$$

Where I_{photon} is the current that produced by the photons. When the current-voltage graph is examined, it is seen that I_{sc} of the silicon cell is 615.96 mA. The open circuit voltage (V_{oc}) of a solar cell is measured when the output terminals of the device are open or I is zero. At a given light intensity, V_{oc} represents the maximum output voltage of the solar cell and given as follows.

$$V_{oc} = \frac{kT}{q} \ln\left(\frac{I_{photon}}{I_o} + 1\right) \tag{2}$$

Where k is the Boltzmann constant, T is absolute temperature, I_o is the saturation current and q is the electronic charge. While I_o depends on device design and material selection, I_{photon} depends on device design and material selection as well as lighting intensity. The value of V_{oc} is determined as 613.03 mV from current-voltage graph.

The maximum output power (P_m) of a solar cell has calculated using the following expression.

$$P_m = V_m I_m \tag{3}$$

Where V_m and I_m are the maximum voltage and current, respectively at a maximum power point (P_m). The I_m and V_m values from the power-voltage graph have found as 534.10 mA and 371.85 mV, respectively. The P_m is calculated as 198.61 mW using the Equation (3).

The efficiency (η) of a solar cell is given as follows.

$$\eta = \frac{V_m I_m}{P_{in} A} \tag{4}$$

Where P_{in} is the total power of the light intensity on the cell and A is the effective area. The η value of the non-irradiated silicon cell has calculated as 15.59%. The performance parameters of the solar cell are given in Table 2.

Figures 2b and 3b represent the I-V and P-V plots after irradiation of the silicon cell. After proton irradiation, the I_{sc} and V_{oc} of the silicon cell have found to be 522.33 mA and 572.94 mV, respectively. It is seen that the maximum current, maximum voltage and maximum power values are 475.62 mA, 412.06 mV and 195.98 mW, respectively. The efficiency of the irradiated silicon cell has calculated as 15.08%. When the graphs are examined, it is seen that there is a decrease of 93.626 mA in I_{sc} of the irradiated silicon cell. The reduction is due to the fact that new energy levels emerging in the proton radiation band gap reduced the number of minority carriers. It is seen that there is a decrease of 40.08 mV in V_{oc}. By proton irradiation applied to the silicon cell, the radiation has increased the number of recombination centers and caused a decrease in V_{oc}. The maximum power has decreased by 2.62 mW. Since minority carriers at deep levels are short-lived, they are trapped by the reunification centers before they can reach the exit terminals of the structure. Thus, it also reduced other performance parameters such as the power parameter of solar cell (Srivastava et al., 2006).
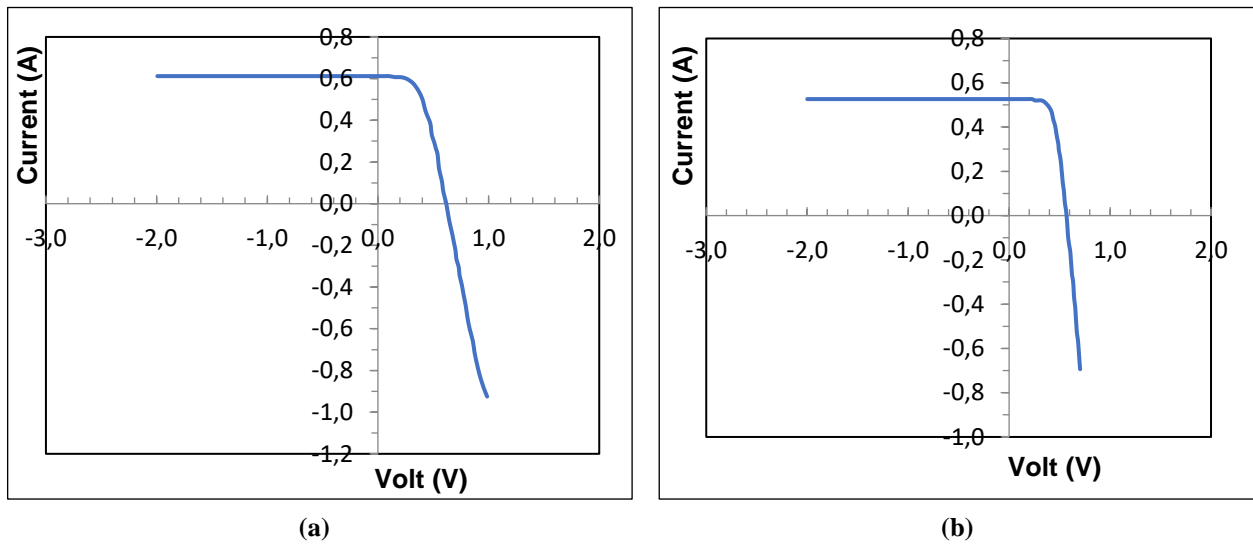

(a)   **(b)**

*Figure 2. I-V plot of silicon cell, **a**) before proton irradiation and **b**) after proton irradiation*
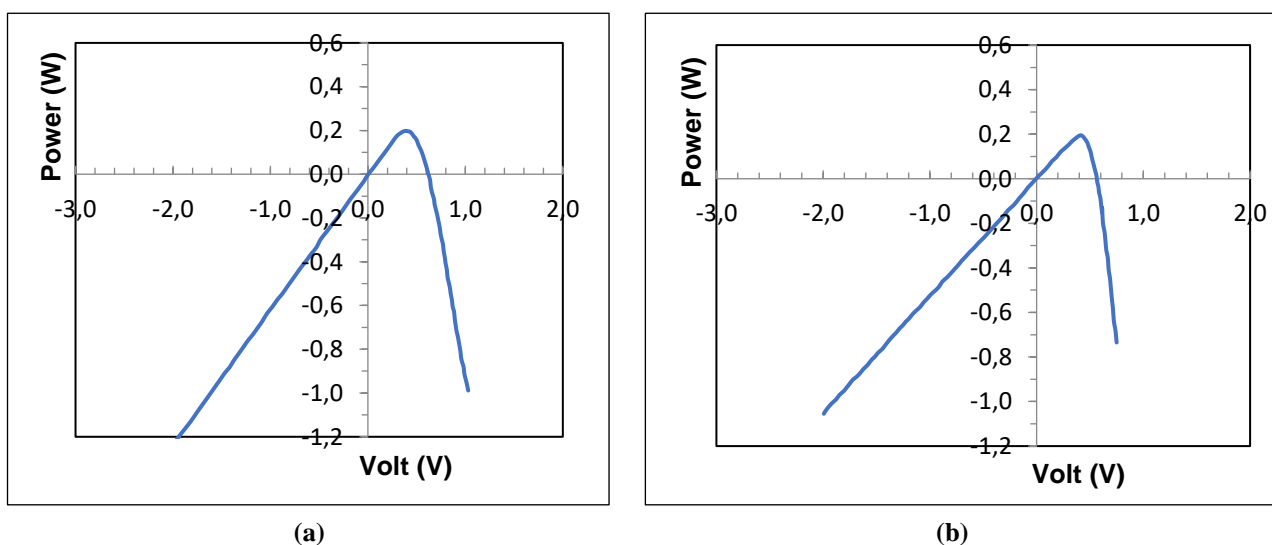

(a)   **(b)**

*Figure 3. P-V plot of silicon cell, **a**) before proton irradiation and **b**) after proton irradiation*

***Table 2** The performans parameters of the solar cell before and after proton irradiation*

	I_{sc} (mA)	V_{oc} (mV)	P_m (mW)	η(%)
Before irradiation	615.96	613.03	198.61	15.59
After irradiation	522.33	572.94	195.98	15.08

The SRIM simulation results of particle trajectories are shown in Figure 4. The purpose of the SRIM simulation program is to examine the interactions of matter and ions with each other (Ziegler, 2004). The results of the interactions are expressed with graphical and numerical data that take place during the transition of ions in the target substance. SRIM/TRIM can be studied not only the spacing of ions in matter, but also many other aspects of damage to the target during the deceleration process. The used cell thickness has 250 μm. Thus, particle trajectories and displacement damage distribution have determined more clearly.
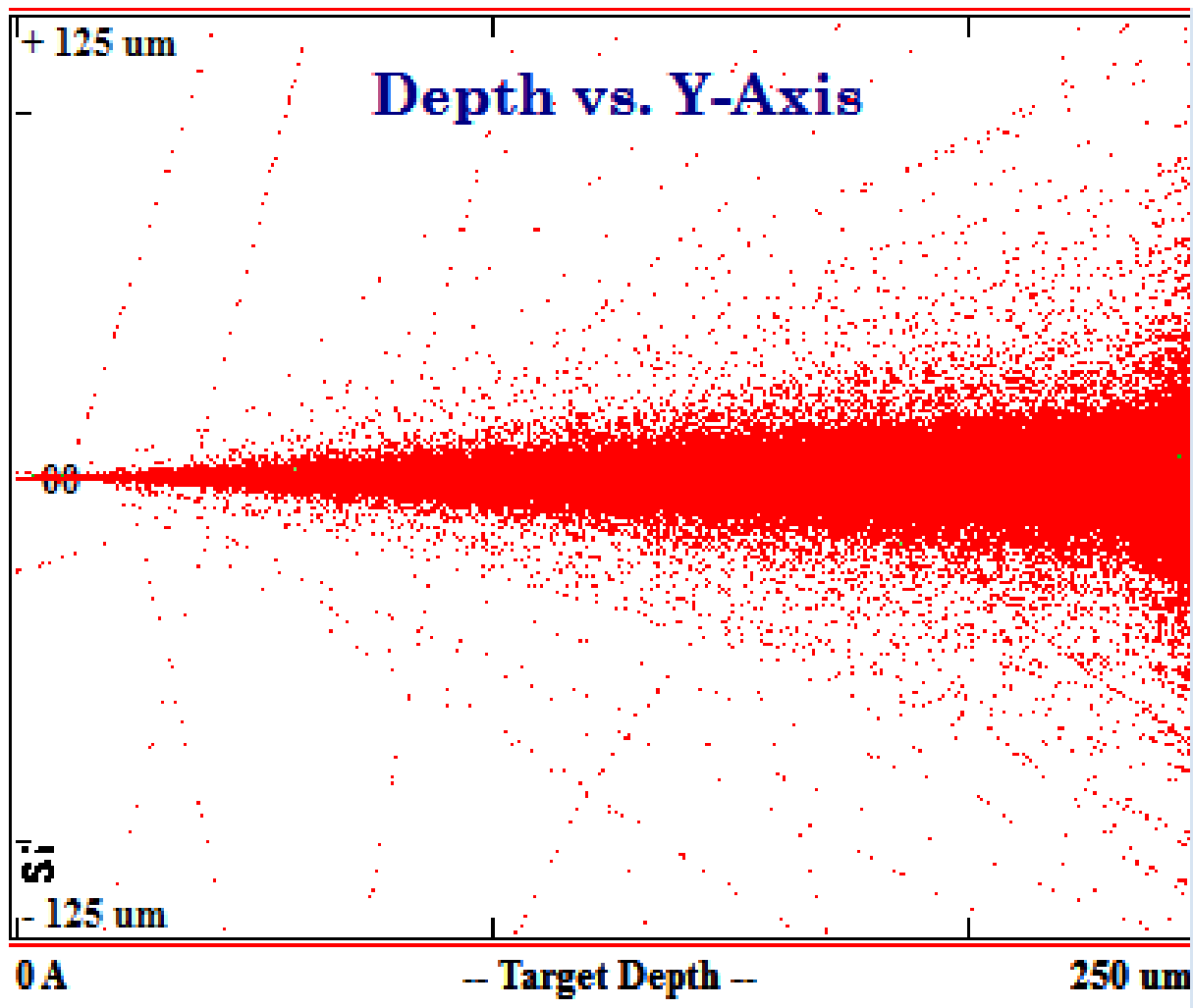

Figure 4. *Particle trajectories in SRIM/TRIM*

The final distribution of the ion has been determined by directing into the complex target in the SRIM/TRIM, and the change in the structure of the silicon cell interacting with the proton beam has examined. The energy and dose of the ions required by implanting atoms have calculated at a given depth and concentration into a target. Thus, the displacement damage is modeled using SRIM (Messenger et al., 2003). Figure 5 has shown the number of displaced target atoms created by the colliding ions. As seen in Figure 5, the ions have released 99.96% of their energy directly to the target and 0.04% to the recoil stages.
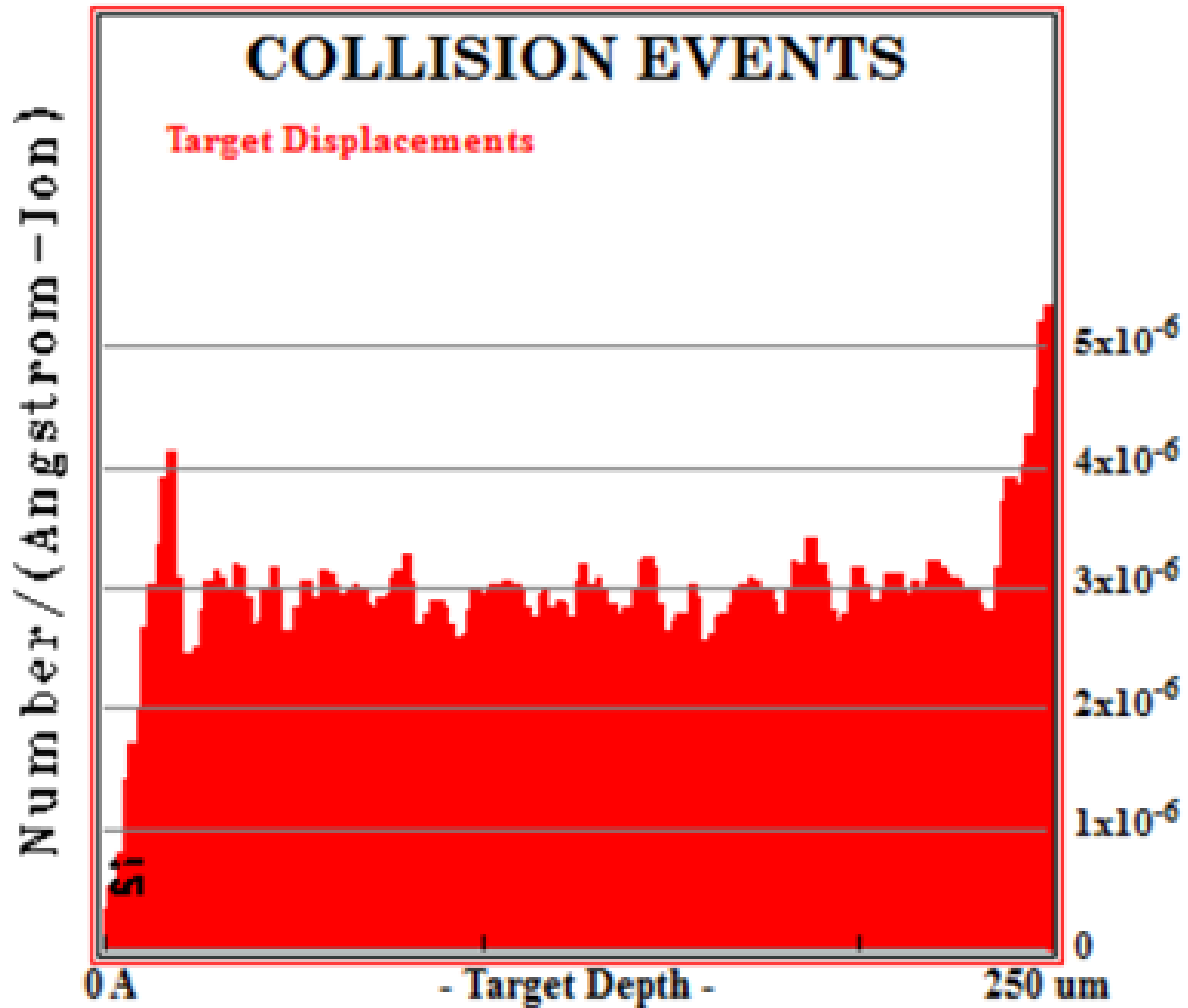
Figure 5. Total target displacement

4. CONCLUSION

In this study, the electrical characterizations of silicon cell have realized before and after proton irradiation. The changes in the electrical parameters of photovoltaic cell after irradiation have investigated with the help of obtained data. In addition, calculations have made about the damage by the proton on the silicon cell with the SRIM/TRIM program, and graphics have created.

When the parameters of silicon cells have compared before and after irradiation, a decrease in open circuit voltage has observed. Radiation has created new energy levels and reduced the number of minority carriers. Therefore, the short circuit current has also reduced. Moreover, radiation has increased the number of reunification centers. Therefore, a decrease in open circuit voltage value has occurred. On the other hand, it has been observed that the proton beam affects the maximum power value of the silicon cell. As a result, the efficiency of the cell decreased 0.51%.

The average displacement value of the proton per target atom has calculated as 0.5×10^{3}. The number of displaced target atoms formed by the colliding ions have appears to be constant for a silicon cell. As a result of the interaction between the proton and the solar cell, energy loss occurs due to displacement. It is seen that the penetration depth of the protons is higher than mentioned energy. Hence it has been observed that the proton has damaged the silicon cell and caused a decrease in device performance. On the other hand, it was seen that proton irradiation can be a tool for controlling the material and cell properties.

ACKNOWLEDGEMENT

CONFLICT OF INTEREST

The author declares no conflict of interest.

REFERENCES

Adıgüzel, A., Açıksöz, S., Çağlar, A., Çetinkaya, H., Esen, Ş., Halis, D., Hamparsunoğlu, A., İlhan, T. B., Kılıçgedik, A., Koçer, O., Oğur, S., Öz, S., Özbey, A., Özcan, V. E., & Ünel, N. G. (2023). Ion Source and LEBT of KAHVELab Proton Beamline. *Journal of Instrumentation*, *18*, T01002. doi:10.1088/1748-0221/18/01/T01002

Alurralde, M., Tamasi, M. J. L., Bruno, C. J., Martínez Bogado, M. G., Plá, J., Fernández Vázquez, J., Durán, J., Schuff, J., Burlon, A. A., Stoliar, P., & Kreiner, A. J. (2004). Experimental and theoretical radiation damage studies on crystalline silicon solar cells. *Solar Energy Materials & Solar Cells*, *82*(4), 531-542. doi:10.1016/j.solmat.2003.11.029

Bilge Demirkoz, M., Seckin, C., Avaroglu, A., Bulbul, B., Uslu, P., Kılıç, E., Orhan, Y., Akcelik, S., Yigitoglu, M., Saral, C., Uzun Duran, S., Kılıç, U., Efthymiopoulos, I., Berkay Poyrazoglu, A., Albarodi, A., & Celik, N. (2020). Metu-Defocusing Beamline : A 15-30 Mev Proton Irradiation Facility and Beam Measurement System. *EPJ Web of Conferences*, *225*, 01008. doi:10.1051/epjconf/202022501008

Hadjdida, A., Bourahla, M., Ertan, H. B., & Bekhti, M. (2018). Analytical modelling, simulation and comparative study of multi-junction solar cells efficiency. *Int. J. Renew. Energy Res.*, *8*(4) 1824-1832. doi:10.20508/ijrer.v8i4.8135.g7488

Liu, X., Liu, N., Zhang, G., Zhang, L., & Wang, T. (2022). Structural and Optical Changes in GaAs Irradiated with 100 keV and 2 MeV Protons. *J. Phys. D: Appl. Phys.*, *55*, 295105. doi:10.1088/1361-6463/ac6bcd

Messenger, S. R., Burke, E. A., Morton, T. L., Summers, G. P., Walters, R. J., & Warner, J. H. (2003, May 11-18). Modelling low energy proton radiation effects on solar cells. In: K. Kurokawa, L. L. Kazmerski, B. McNelis, M. Yamaguchi, C. Wronski, W. C. Sinke (Eds.), Proceedings of the 3rd World Conference on Photovoltaic Energy Conversion, Vol. C, (pp. 716-719), Osaka, Japan.

Miyazawa, Y., Ikegami, M., Chen, H-S., Ohshima, T., Imaizumi, M., Hirose, K., & Miyasaka, T. (2018). Tolerance of perovskite solar cell to high-energy particle irradiations in space environment. *iScience*, *2*, 148-155. doi:10.1016/j.isci.2018.03.020

Raya-Armenta, J. M., Bazmohammadi, N., Vasquez, J. C., & Guerrero, J. M. (2021). A Short Review of Radiation-Induced Degradation of III-V Photovoltaic Cells for Space Applications. *Solar Energy Materials & Solar Cells*, *233*, 111379. doi:10.1016/j.solmat.2021.111379

Song, P., Zhao, J., Liu, J., Yue, H., Pawlak, M., & Sun, X. (2022). Evaluation of the performance degradation of silicon solar cell irradiated by low-level (<1 MeV) energetic particles using photocarrier radiometry. *Infrared Physics & Technology*, *123*, 104177. doi:10.1016/j.infrared.2022.104177

Srivastava, P. C., Pandey, S. P., & Asokan, K. (2006). A study on swift (~100 MeV) heavy (Si8+) ion irradiated crystalline Si-solar cell. *Nuclear Instruments and Methods in Physics Research Section B: Beam Interactions with Materials and Atoms*, *244*(1), 166-170. doi:10.1016/j.nimb.2005.11.029

Sultansoy, S. (1993). Regional Project for Elementary Particle Physics: Linac-Ring Type c- τ Factor. *Tr. J. Phys.*, *17*, 591-597.

Tada, H. Y., Carter, J. R. Jr., Anspaugh, B. E, & Downing, R. G. (1982). *Solar cell radiation handbook* (3rd Ed.). JPL Publication.

Wang, Y., Ren, Z., Thway, M., Lee, K., Yoon, S. F., Peters, I. M., Buonassisi, T., Fizgerald, E. A., Tan, C. S., & Lee, K. H. (2017). Fabrication and characterization of single junction GaAs solar cells on Si with As-doped Ge buffer. *Solar Energy Materials and Solar Cells*, *172*, 140-144. doi:10.1016/j.solmat.2017.07.028

Yu, Z., Sun, Y., Zhang, G., Lu, W., & Zuo, D. (2021). Experimental study on machining germanium wafer with ice particle, fixed abrasive tools. *The International Journal of Advanced Manufacturing Technology*, *115*, 3225-3232. doi:10.1007/s00170-021-07352-4

Ziegler, J. F. (2004). SRIM-2003. *Nuclear Instruments and Methods in Physics Research Section B: Beam Interactions with Materials and Atoms*, *219-220*, 1027-1036. doi:10.1016/j.nimb.2004.01.208

JOURNAL OF SCIENCE

PART A: ENGINEERING AND INNOVATION